Domain Engineering in KTiOPO$_4$

Carlota Canalias

Doctoral Thesis

Laser Physics and Quantum Optics

Royal Institute of Technology

Stockholm 2005

Cover picture: AFM image of the surface relief resulting from a domain-selective etch on former c⁻ face of a KTP crystal.

Domain engineering in KTiOPO$_4$

Abstract

Ferroelectric crystals are commonly used in nonlinear optics for frequency conversion of laser radiation. The quasi-phase matching (QPM) approach uses a periodically modulated nonlinearity that can be achieved by periodically inverting domains in ferroelectric crystals and allows versatile and efficient frequency conversion in the whole transparency region of the material.

KTiOPO$_4$ (KTP) is one of the most attractive ferroelectric non-linear optical material for periodic domain-inversion engineering due to its excellent non-linearity, high resistance for photorefractive damage, and its relatively low coercive field. A periodic structure of reversed domains can be created in the crystal by lithographic patterning with subsequent electric field poling. The performance of the periodically poled KTP crystals (PPKTP) as frequency converters rely directly upon the poling quality. Therefore, characterization methods that lead to a deeper understanding of the polarization switching process are of utmost importance.

In this work, several techniques have been used and developed to study domain structure in KTP, both in-situ and ex-situ. The results obtained have been utilized to characterize different aspects of the polarization switching processes in KTP, both for patterned and unpatterned samples.

It has also been demonstrated that it is possible to fabricate sub-micrometer (sub-µm) PPKTP for novel optical devices. Lithographic processes based on e-beam lithography and deep UV-laser lithography have been developed and proven useful to pattern sub-µm pitches, where the later has been the most convenient method. A poling method based on a periodical modulation of the K-stoichiometry has been developed, and it has resulted in a sub-µm domain grating with a period of 720 nm for a 1 mm thick KTP crystal. To the best of our knowledge, this is the largest domain aspect-ratio achieved for a bulk ferroelectric crystal. The sub-micrometer PPKTP samples have been used for demonstration of 6:th and 7:th QPM order backward second-harmonic generation with continuous wave laser excitation, as well as a demonstration of narrow wavelength electrically-adjustable Bragg reflectivity.

Keywords: quasi-phase matching, KTiOPO$_4$, ferroelectric domains, atomic force microscopy, periodic electric field poling, polarization switching, second harmonic generation.

To Marc.

I know nothing. I am from Barcelona.
Manuel, Fawlty Towers.

Preface

This thesis surveys the work performed in the Laser Physics and Quantum Optics group, Department of physics, at the Royal Institute of Technology since I started these doctoral studies, almost five years now.

This thesis consists of an introductory part giving a background to the work performed and the reprints of the publications.

List of publications

Publications included in the thesis

I. J. Wittborn, C. Canalias, K.V. Rao, R. Clemens, H. Karlsson and F. Laurell "Nanoscale characterisation of domains in periodically poled ferroelectrics," Appl. Phys. Lett. 80, 1622 (2002).

II. C. Canalias, V. Pasiskevicius, A. Fragemann, F. Laurell, "High resolution domain imaging on the non-polar y-face of periodically poled $KTiOPO_4$ by means of atomic force microscopy," Appl. Phys. Lett., 82, 734 (2003).

III. C. Canalias, J. Hirohashi, V. Pasiskevicius and F. Laurell "Polarization switching characteristics of flux grown $KTiOPO_4$ and $RbTiOPO_4$ at room temperature" J. Appl. Phys. 97, 124105 (2005).

IV. C. Canalias, V. Pasiskevicius, F.Laurell, S. Grilli, P. Ferraro, and P De Natale "In situ visualization of domain kinetics in flux grown $KTiOPO_4$ by digital holography. (Submitted to Appl. Phys. Lett.)

V. C. Canalias, S. Wang, V. Pasiskevicius, and F.Laurell "Domain nucleation and growth in flux-grown $KTiOPO_4$ formed by periodic poling at room temperature" (submitted to Appl. Phys. Lett.)

VI. C. Canalias, V. Pasiskevicius, R. Clemens, F. Laurell, "Sub-micron periodically poled flux grown $KTiOPO_4$", Appl. Phys. Lett. 82, 4233 (2003).

VII. C. Canalias, V. Pasiskevicius, M. Fokine and F. Laurell "Backward quasi-phase matched second harmonic generation in sub-micrometer periodically poled flux-grown $KTiOPO_4$" Appl. Phys. Lett. 86, 181105 (2005)

Publications not included in the thesis

A. V. Pasiskevicius, C. Canalias, and F. Laurell "Highly efficient stimulated Raman scattering of picosecond pulses in $KTiOPO_4$" (submitted to Appl. Phys. Lett.)

B. M. Pelton, P. Marsden, D. Ljunggren, M. Tengner, A. Karlsson, A. Fragemann, C. Canalias, F. Laurell, "Bright, single-spatial-mode source of frequency non-degenerate, polarization-entangled photon pairs using periodically poled KTP" *Optics Express*, 12, 3573 (2004).

C. C. Canalias, R. Clemens, J. Hellström, F. Laurell, J. Wittborn, H. Karlsson, "High resolution Non-invasive techniques for Imaging Domains and Domain Walls in Ferroelectric Crystals", p. 207 in the book "State of the art: Periodically microstructured nonlinear optical materials" Eds. E. Diéguez, V. Bermúdez. World Scientific (in press), 2005.

D. C. Canalias, R. Clemens, J. Hellström, F. Laurell, J. Wittborn, H. Karlsson "Scanning probe microscopy characterization of ferroelectric domains and domain walls in KTiOPO$_4$" pp363 in the book "Scanning probe microscopy: characterization, nanofabrication and device application of functional materials. Ed. P. M. Vilarinho, Y. Rosenwaks, and A. Kingon, Nato Science series II. Mathematics, physics and chemistry. Vol.186. Kluwer Academic Publishers, The Netherlands, 2005.

These papers will be referred to in the text by the notation used above.

Contents

Chapter 1

Introduction

The introduction of periodically poled ferroelectrics by bulk electric field poling in 1993[1] had a great influence on the development of new laser sources. The use of these crystals in quasi-phase matched (QPM) nonlinear frequency conversion offers new discrete wavelength lines and wavelength tunability over a much broader spectral range than is possible with conventional lasers, and hence it can lead to new applications. Examples of areas where QPM-based lasers have been tested are: medical diagnosis and treatment, materials processing, scientific instruments, optical communications, low-light imaging, atmospheric aberration compensation for astronomy and satellite tracking, scene projectors for testing and entertainment, optical signal processing, data storage, underwater communications and imaging, and remote identification of biological species.

Nonlinear frequency conversion imposes specific demands on the nonlinear optical materials. Besides presenting sufficiently large second-order susceptibility, the material must be optically transparent both to the incident and generated wavelengths, permit phase matching of the interaction, and have low susceptibility to optical damage.[2] In order to maintain an efficient energy transfer in nonlinear frequency conversion, the relative phase of the interacting waves in the nonlinear material must be kept constant. This happens, for example, if the refractive indexes are equal at all interacting wavelengths. In quasi phase matching, rather than relaying on the material's natural properties of dispersion and birefringence, the sign of the nonlinear susceptibility is reversed every coherence length in order to reset the accumulated phase error between the interacting waves. In ferroelectric crystals, such nonlinear modulation can be obtained by periodically reversing the sign of the spontaneous polarization, so-called periodic poling.

The most popular material to implement QPM in is periodically poled congruent $LiNbO_3$. Domain inversion in $LiNbO_3$ has been extensively studied by many researchers worldwide. [3-6] The popularity of $LiNbO_3$ is directly related to its significant homogeneity and wide commercial availability at moderate prices, the relatively standardized poling technique, and its large effective nonlinear optical coefficients. However, it suffers from

photorefractive damage which limits their practical use, particularly in applications in the visible range and at high optical power. Secondly, its trigonal anisotropy of the surface energy, which favors formation of domains of hexagonal shape, difficulties poling of dense domain gratings for first order blue or UV generation. Furthermore, since its coercive field is high (~21 kV/mm), the aperture of the QPM devices have mostly been restricted to ~0.5 mm, which is a practical limitation in many optical experiments. More or less the same can be said about $LiTaO_3$. In the recent years, growth and periodic poling of stoichiometric $LiNbO_3$ and $LiTaO_3$ crystals have been developed. However, their price is much higher than for the congruent ones, and, although the resistance to optical damage is considerably increased, material growth technology has to be improved especially in terms of homogeneity and consistency in crystal quality. Moreover, optimization of the poling process in these materials is still under development as their composition is varying.

On the other hand, periodically poled $KTiOPO_4$ (KTP) and its isomorphs present excellent nonlinearities, are well functioning both for UV, IR and visible generation and in high power application[7-10] since the photorefractive damage is not an issue in these materials.[11] At room temperature the coercive field of KTP is one-order of magnitude lower than that of $LiNbO_3$ and $LiTaO_3$, thicker periodically poled structures can be easily fabricated giving access to higher optical powers. Moreover, its chiral crystal structure along the polar axis limits the domain broadening, which makes it easier to fabricate dense domain gratings.

Thus, why has KTP not become as popular as $LiNbO_3$?

To start with, KTP cannot be Czochralski grown so it does not come in large wafer size as $LiNbO_3$ (typical wafer size for $LiNbO_3$ is 5 inches, whereas for KTP is 1 inch), and it is at least ten times more expensive than $LiNbO_3$. Secondly, material variations from wafer to wafer or within the same wafer, manifesting itself an ionic conductivity that can vary as much as by an order of magnitude[7], has led to a reduced yield of periodically poled structures. Moreover, the ionic conductivity makes it difficult to control the poling by switching-current measurement, and alternative monitoring techniques had to be developed.[8,12] On top of that, the mechanisms governing the polarization switching process in KTP have not been studied in much detail. Thus, it seemed of utmost importance to better understand the poling process and its correlation to the material properties.

The aim of this thesis has been to try to gain deeper understanding of the mechanisms governing the polarization reversal in KTP at room temperature so that the potential of this material could be better utilized. Also, we wanted to develop techniques to visualize the domain structure in-situ and ex-situ. In parallel to that, the other goal of the project has been to explore the possibility of fabricating sub-micrometer periodic domain gratings for new optical devices, such as electrically addressable Bragg reflectors. Therefore, processes to pattern and pole ferroelectric domains narrower than 1 μm had to be developed.

This thesis is organized as follows. Chapter 2 provides an introduction to nonlinear optics and quasi-phase matching to motivate the need of periodically poled

structures. Chapter 3 gives an overview of the physical concepts related to ferroelectricity and domain switching. Chapter 4 describes KTP and its most relevant properties, and chapter 5 describes the ex-situ and in-situ methods used to study domain structures during these work. Chapter 6 surveys the study of polarization switching properties in unpatterned KTP. Investigations of periodic poling of KTP can be found in chapter 7. Chapter 8 presents the fabrication and evaluation of sub-micrometer PPKTP. Finally, chapter 9 concludes the results obtained during this work.

References Chapter 1

[1] M. Yamada, N. Nada, M. Saitoh, and K. Watanabe, Appl. Phys. Lett., 62, 435 (1993).

[2] P. F. Bordui and M.M. Fejer, Annu. Rev. Mater. Sci., 23, 321 (1993)

[3] V. Gopalan, T.E. Mitchell, K. Kitamura, and Y. Furukawa Appl. Phys. Lett. 72, 1981 (1998).

[4] S. Kim, V. Gopalan, and A. Gruverman, Appl. Phys. Lett. 80, 2740 (2002).

[5] J-H Ro and M. Cha, Appl. Phys. Lett. 77, 2391 (2000).

[6] L. -H. Peng, Y.-C. Fang, and Y. -C. Lin, Appl. Phys. Lett. 74, 2070 (1999).

[7] H. Karlsson and F. Laurell, Appl. Phys. Lett. 71, 3474 (1997).

[8] H. Karlsson, F. Laurell, and L. K. Chen, Appl. Phys. Lett. 74, 1519 (1999).

[9] H. Karlsson, M. Olson, G. Arvidsson, F Laurell, U. Bäder, A. Borsutzky, R. Wallenstein, S. Wickström and M. Gustafsson, Opt. Lett. 24, 330 (1999).

[10] J. –P. Fève, O. Pacaud, B. Boulanger, B. Ménaert, J. Hellström, V. Pasiskevicius, and F. Laurell, Opt. Lett. 26, 1882 (2001)

[11] J. Hellström, V. Pasiskevicius, H. Karlsson and F. Laurell, Opt. Lett. 25, 174 (2000).

[12] J. Hellström, R. Clemens, V. Pasiskevicius, H. Karlsson, and F. Laurell, J.Appl. Phys. 90, 1489 (2001).

Chapter 2

Nonlinear optics and Quasi-phase matching

2.1. The nonlinear polarization

When an electromagnetic wave passes through a dielectric material it induces a polarization in the material, i.e., a displacement of the valence electrons from their stationary orbits. This induced polarization can be express as a function of the applied electric field:

$$\mathbf{P} = \varepsilon_0 \chi^{(1)} \mathbf{E} + \varepsilon_0 (\chi^{(2)} \mathbf{E}^2 + \chi^{(3)} \mathbf{E}^3 + ...) = \mathbf{P}^{L} + \mathbf{P}^{NL} \tag{2.1}$$

Where ε_0 is the permittivity of the vacuum, $\mathbf{E}$ is the electric filed component of the electromagnetic wave, and $\chi^{(m)}$ is the susceptibility tensor of m:th order with the rank (m+1). $\mathbf{P}^{L} = \varepsilon_0 \chi^{(1)} \mathbf{E}$ corresponds to the linear part of the polarization and $\mathbf{P}^{NL} = \varepsilon_0 (\chi^{(2)} \mathbf{E}^2 + \chi^{(3)} \mathbf{E}^3 + ...)$ to the nonlinear part.

In every day life, the strength of the electric field is relatively small, and the induced polarization is proportional to the electric field, and the material response can be solely described by $\mathbf{P}^{L}$. However, if the light is intense enough, the relative displacement of the electron cloud from its nucleus is nonlinear with the electric field, and $\mathbf{P}^{NL}$ has to be taken into account.[1]

2.2. Second order nonlinear interactions

The second order nonlinear effects, described by $\mathbf{P}^2(\omega_3) = \varepsilon_0 \chi^{(2)} \mathbf{E}_{\omega 1} \mathbf{E}_{\omega 2}$, are usually relatively weak, yet it is possible to use them to generate frequency conversion processes at power levels suitable for practical applications. For all the processes the energy of the

photons that take part in the frequency mixing has to be conserved. Fig 2.1 illustrates the different types of frequency conversion processes. In sum and difference frequency mixing, two input photons, that travel through the nonlinear media, are added or subtracted into one photon of higher or lower energy: $\omega_3 = \omega_1 \pm \omega_2$. When $\omega_1 = \omega_2 = \omega$ and $\omega_3 = 2\omega$, the nonlinear susceptibility gives rise to second harmonic generation (SHG). In the case of $\omega_1 = \omega_2 = \omega$, and $\omega_3 = 0$, a constant electric polarization of the medium is produced and the effect is known as optical-rectification. Another special case that has found important applications is when $\omega_1 = 0$ and $\omega_3 = \omega_2 = \omega$. Then, one of the input fields is static, and the refractive index of the media is affected through the linear electro-optic effect. This is also known as the Pockel's effect.
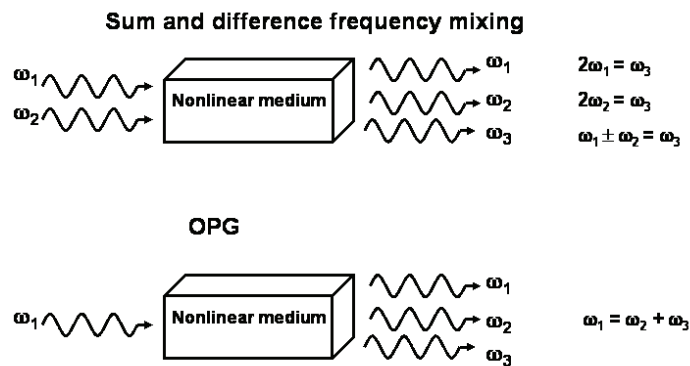
Fig 2.1. Frequency conversion processes in a second-order nonlinear medium.

The other type of processes, down-conversion or optical parametric generation (OPG), starts with one input photon and results in two photons of lower energies. The two generated wavelengths are referred to as signal and idler, of which the signal is the shortest one. When a cavity is used to enhance the efficiency by resonating one or both of the generated fields, the device is called an optical parametric oscillator (OPO).

2.2.1. The second-order nonlinearity and the d-tensor

Consider again second order nonlinear processes: $\mathbf{P}^2(\omega_3) = \varepsilon_0 \chi^{(2)} \mathbf{E}_{\omega1} \mathbf{E}_{\omega2}$. The second-order nonlinearity $\chi^{(2)}$ exists only in a medium without center of inversion in the point-symmetry group. In the literature, the d-tensor is frequently used instead of the second-order nonlinear susceptibility, and it is defined as[1]

$$d_{ijk} \equiv \frac{1}{2}\chi_{ijk} \tag{2.2}$$

If Kleinman symmetry applies[2], i.e. all interacting frequencies are far from resonances, the tensor can be contracted into a 3×6-element matrix, so that:

$$\begin{pmatrix} (P_{\omega_3}^{(2)})_x \\ (P_{\omega_3}^{(2)})_y \\ (P_{\omega_3}^{(2)})_z \end{pmatrix} = 2\varepsilon_0 K \begin{bmatrix} d_{11} & d_{12} & d_{13} & d_{14} & d_{15} & d_{16} \\ d_{21} & d_{22} & d_{23} & d_{24} & d_{25} & d_{26} \\ d_{31} & d_{32} & d_{33} & d_{34} & d_{35} & d_{36} \end{bmatrix} \begin{pmatrix} (E_{\omega_1})_x (E_{\omega_2})_x \\ (E_{\omega_1})_y (E_{\omega_2})_y \\ (E_{\omega_1})_z (E_{\omega_2})_z \\ (E_{\omega_1})_y (E_{\omega_2})_z + (E_{\omega_1})_z (E_{\omega_2})_y \\ (E_{\omega_1})_x (E_{\omega_2})_z + (E_{\omega_1})_z (E_{\omega_2})_x \\ (E_{\omega_1})_x (E_{\omega_2})_y + (E_{\omega_1})_y (E_{\omega_2})_x \end{pmatrix} \tag{2.3}$$

$K(-\omega_3;\omega_1, \omega_2)$ is the degeneracy factor, which takes the value ½ for SHG and optical rectification and 1 for the other conversion processes.

2.3. The coupled wave equations

The Maxwell's equations in a nonlinear, nonmagnetic medium with no currents and no free charges can be expressed in the following form:

$$\nabla^2 \mathbf{E} = \mu_0 \sigma \frac{\partial \mathbf{E}}{\partial \mathbf{t}} + \mu_0 \varepsilon_0 \frac{\partial^2 \mathbf{E}}{\partial \mathbf{t}^2} + \mu_0 \frac{\partial^2 \mathbf{P}}{\partial \mathbf{t}^2} \tag{2.4}$$

where μ_0 is the permeability of vacuum and σ the losses of the material.

If we assume that the medium is lossless and that $\mathbf{E}$ and $\mathbf{P}$ are quasi-plane and quasi-monochromatic waves propagating in the x-direction, $\mathbf{E}$ and $\mathbf{P}$ can be written as

$$\mathbf{E}(x,t) = \frac{1}{2}\left[\mathbf{E}(x,\omega)\exp i(kx - \omega t)\right] + c.c.$$

$$\mathbf{P}(x,t) = \frac{1}{2}\left[\mathbf{P}(x,\omega)\exp i(kx - \omega t)\right] + c.c. \tag{2.5}$$

where ω is the frequency of the waves, k is the wavenumber given by

$$k = \frac{n(\omega)\omega}{c}$$

$n = \sqrt{\dfrac{\varepsilon(\omega)}{\varepsilon_0}}$ is the refractive index at frequency ω, and c the speed of light in vacuum.

If we assume that the wave envelopes $\mathbf{E}(x, \omega)$ and $\mathbf{P}(x, \omega)$ are varying slowly both in amplitude and phase as a function of distance and time, it is possible to apply the "slowly varying envelope approximation", SVEA.[3]

$$\left|\frac{\partial^2 \mathbf{E}(\omega)}{\partial x^2}\right| << \left|k\frac{\partial \mathbf{E}(\omega)}{\partial x}\right|$$

$$\left|\frac{\partial \mathbf{E}(\omega)}{\partial t}\right| << \left|\omega \mathbf{E}(\omega)\right| \tag{2.6}$$

$$\left|\frac{\partial^2 \mathbf{P}(\omega)}{\partial t^2}\right| << \left|\omega\frac{\partial \mathbf{P}(\omega)}{\partial t}\right| << \left|\omega^2 \mathbf{P}(\omega)\right|$$

Using the SVEA approximation, the equation (2.4) gets reduced to

$$\frac{\partial \mathbf{E}(\omega)}{\partial x} = -\alpha\mathbf{E}(\omega) + \frac{i\mu_0 c\omega}{2n}\mathbf{P}^{\mathbf{NL}}(\omega) \tag{2.7}$$

where $\alpha = \dfrac{\mu_0 c\sigma}{2}$ is the loss coefficient of the electric field.

For second order nonlinear processes, all fields mix with all other and three waves couple to each other through three polarizations, yielding three coupled wave equations:

$$\frac{\partial E_1}{\partial x} = -\alpha_1 E_1 + \frac{i\omega_1^2}{k_1 c^2}Kd_{eff}E_3 E_2^* exp(i\Delta kx)$$

$$\frac{\partial E_2}{\partial x} = -\alpha_2 E_2 + \frac{i\omega_2^2}{k_2 c^2}Kd_{eff}E_3 E_1^* exp(i\Delta kx) \tag{2.8}$$

$$\frac{\partial E_3}{\partial x} = -\alpha_3 E_3 + \frac{i\omega_3^2}{k_3 c^2}Kd_{eff}E_1 E_2 exp(-i\Delta kx)$$

The frequency relation of the interacting waves obeys $\omega_3 = \omega_1 + \omega_2$, and the phase-mismatch between them is $\Delta k = k_3 - k_2 - k_1$. The effective nonlinear coefficient, d_{eff}, is obtained from the matrix in equation (2.3) modified with a factor for the relevant phase matching condition. The interaction is maximized when $\Delta k = 0$, which can be achieved by properly choosing the direction of propagation of the interacting waves.

2.4. Phase matching

In three-wave nonlinear processes, useful output power levels are obtained when the phase-mismatch between the interacting waves is equal to zero, i.e. $\Delta k = 0$.

Consider second harmonic generation, where the fundamental optical wave travels with a phase velocity $c/n(\omega)$. The generated wave, the second harmonic, propagates with a phase velocity of $c/n(2\omega)$. Fig. 2.2 illustrates the intensity of the second harmonic generation with different phase matching conditions. The driving polarization and the generated field will thus drift out of phase relative to each other. Thus, the efficiency of the interaction is reduced as energy is transferred from the fundamental wave to the generated wave, then back to the fundamental wave while they propagate through the nonlinear medium (Fig. 2.2, curve c). The distance over which maximum transfer of

energy occurs between the fundamental wave and the generated wave is called the coherence length of interaction:

$$L_c = \left| \frac{\pi}{\Delta k} \right|$$

However, if $\Delta k = 0$ can be achieved by some means, the interaction is phase matched and the contributions to the second harmonic wave generated at each point along the nonlinear material add up in phase with the contributions generated at every other point along the crystal, thus the second harmonic field grows linearly with distance in the crystal and its intensity grows quadratically (Fig. 2.2, curve a).

There are two important techniques to achieve phase matching: Birefringent phase matching (BPM) (Fig. 2.2, curve a) and quasi-phase matching (QPM) (Fig. 2.2, curve b).[4]
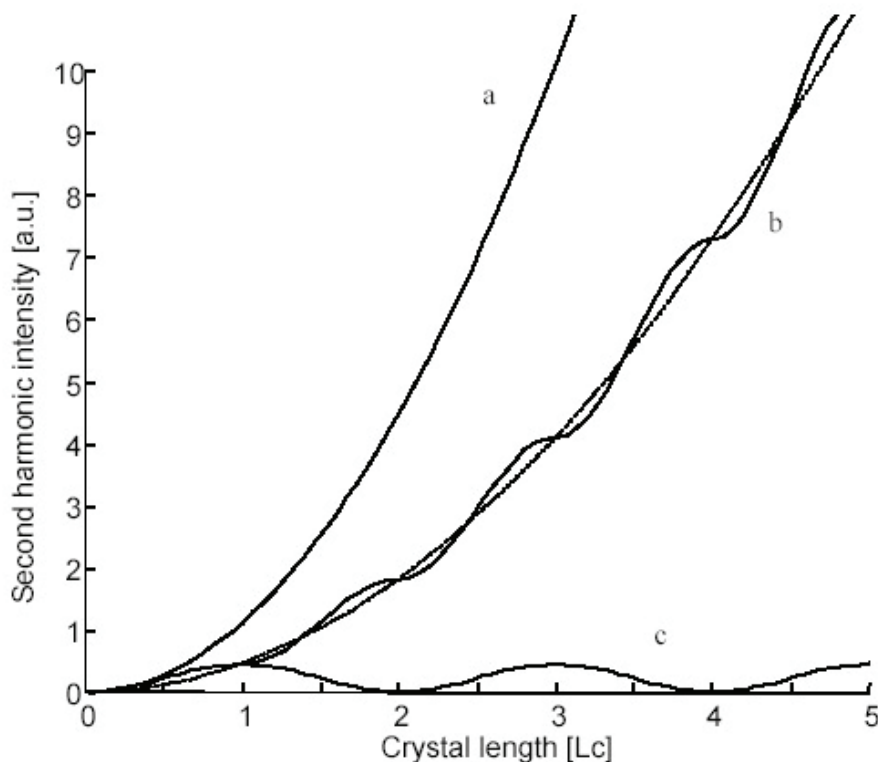
Fig. 2.2 Second harmonic generation in a material with different phase matching conditions. Line (a): perfect phase matching; line (c):non-phase matched interaction; line (b) first order QPM by flipping the sign of the nonlinearity every coherence length of the interaction of curve (c).[3,5]

2.4.1. Birefringent phase matching (BPM)

The basic idea of BPM is that the interacting waves of different frequencies are polarized differently, so that their corresponding phase velocities can be adjusted and their wave vectors can satisfy the phase matching conditions. Referring to a three-waves nonlinear

process, there is two main types of BPM. For type I the fields at frequencies ω_1 and ω_2 have the same polarization and the third field ω_3 is polarized orthogonal compared to the two first. For type II the fields at ω_1 and ω_2 are orthogonally polarized.

The situation where the angle of the beam propagation in relation to the axis of the dielectric tensor is $\theta=90°$ is referred to as noncritical phase matching, while the case of $\theta \neq 90°$ is called critical phase matching.

Noncritical phase matching is advantageous over critical phase matching since the Poyinting vector walk-off angle for this case is zero, which places less constraint on the beam size and the crystal length.

In birefringent phase matching, many desirable implementations are limited by problems occurring in this method, such as Poynting-vector walk-off, low effective nonlinear coefficient, and inconvenient phase-matching temperatures and angles[6]. In addition, in birefringent phase matching the range of the wavelengths over which a particular crystal can be used is determined by the dispersion of the indices of refraction for light polarized along the principal axes and by the second-order nonlinear susceptibility tensor. Efficient nonlinear conversion requires not only that the phase-matching conditions are satisfied for the wavelengths of interests, but also that the nonlinear optical coefficients corresponding to the chosen polarization directions are large.

2.4.2. Quasi-phase matching

Quasi-phase matching is an alternative technique to birefringent phase matching for compensating phase velocity dispersion in frequency-conversion applications, and thus achieving efficient energy transfer between the interacting waves.

Armstrong *et al.*[7] were the first to suggest ways to achieve QPM. For a frequency-conversion process, such as an OPG or a SHG process, the phase mismatch is accumulated with increasing interaction length. After a coherence length, the conversion efficiency decreases as energy flows back from the converted wave to the driving wave. If the nonlinear coefficient is modulated with a period twice the coherence length, in other words, the nonlinear coefficient changes its sign after each coherence length, the accumulated phase mismatch can be offset. QPM achieves phase matching through artificial structuring of the nonlinear material rather than through its inherent birefringent properties. The periodic phase correction inherent in QPM causes the SH power to build up in a stepwise fashion (see Fig 2.2, curve b). The build up is less rapid than what would occur with birefringent phase matching. Despite this reduced efficiency the great advantage of QPM is that it can be employed when BPM is impossible and can provide non-critical phase matching for any nonlinear interaction permitted by the transparency range of the material.

To achieve QPM, an artificially engineered sign modulation of the nonlinear tensor d_{ijk} can be used. Assume that the nonlinear modulation can be described by a function g(x),

which is a rectangular function with the period Λ and magnitude +/-1. Then, g(x) can be expressed by a Fourier expansion[4]:

$$g(x) = \sum_{m=-\infty}^{\infty} G_m \exp(iK_m x) \tag{2.9}$$

K_m is the magnitude of the m*th*-harmonic of grating vector, K_m.

$$K_m = \frac{2\pi m}{\Lambda} \tag{2.10}$$

The direction of the grating vector is along the propagation direction x of the electromagnetic waves. The effective nonlinear coefficient can be written as

$$d(x) = d_{ijk} g(x) \tag{2.11}$$

The conversion will be efficient if $\Delta k_{tot} = \Delta k + K_m \approx 0$, which is fulfilled for two conjugate terms in the series of g(x). Thus, the effective nonlinear coefficient for QPM is reduced to $d_{eff} = G_m d_{ijk}$. For a rectangular structure with a duty-cycle, $D = \frac{L_p}{\Lambda}$, where L_p is the length of the grating that have a positive sign of its d_{ijk}, the coefficient G_m takes the values:

$$G_m = \frac{2}{\pi m} \sin(\pi m D) \tag{2.12}$$

At the optimum D, i.e. 50% duty-cycle, the sine function becomes 1, and $d_{eff} = \frac{2}{\pi m} d_{ijk}$.

2.4.3. Fabrication of QPM structures

The most direct technique for QPM is that the nonlinear crystal is divided into segments each one a coherence length long with each segment then rotated relative to its neighbors by 180° about the axis of propagation. Because of the lack of inversion symmetry, this has the effect of changing the sign of the components of the nonlinear susceptibility tensor. Hence the nonlinear polarization wave is shifted by π radians after each coherence length. The coherence length for frequency conversion process is normally only a few micrometers. It is hence difficult to fabricate such thin segments of nonlinear crystals and to control the thickness of them precisely.[4] However, there is another approach: a technique based on periodic poling of single domain ferroelectric crystals which yields QPM devices suitable for applications in the UV, visible and IR regions. The process creates periodic reversals of the spontaneous polarization (P_S) of the crystal, where the width of each domain is the coherence length of the nonlinear process. Let us see the effect of the spontaneous polarization on SHG[8]. In Fig. 2.3(a) the applied electric field at the fundamental frequency ω_1 induces a separation of charge that adds to and subtracts from the charge separation associated with the spontaneous polarization. Note that in the figure, the nonlinear response of the induced polarization has been decomposed into components at ω_1 and $2\omega_1$. The same effect when the direction of the

spontaneous polarization is reversed is show in Fig. 2.3(a). The second-harmonic components are π out of phase with each other. Thus, periodic inversion of the P_s provides a means for producing the 180° phase shift required to satisfy the QPM condition.
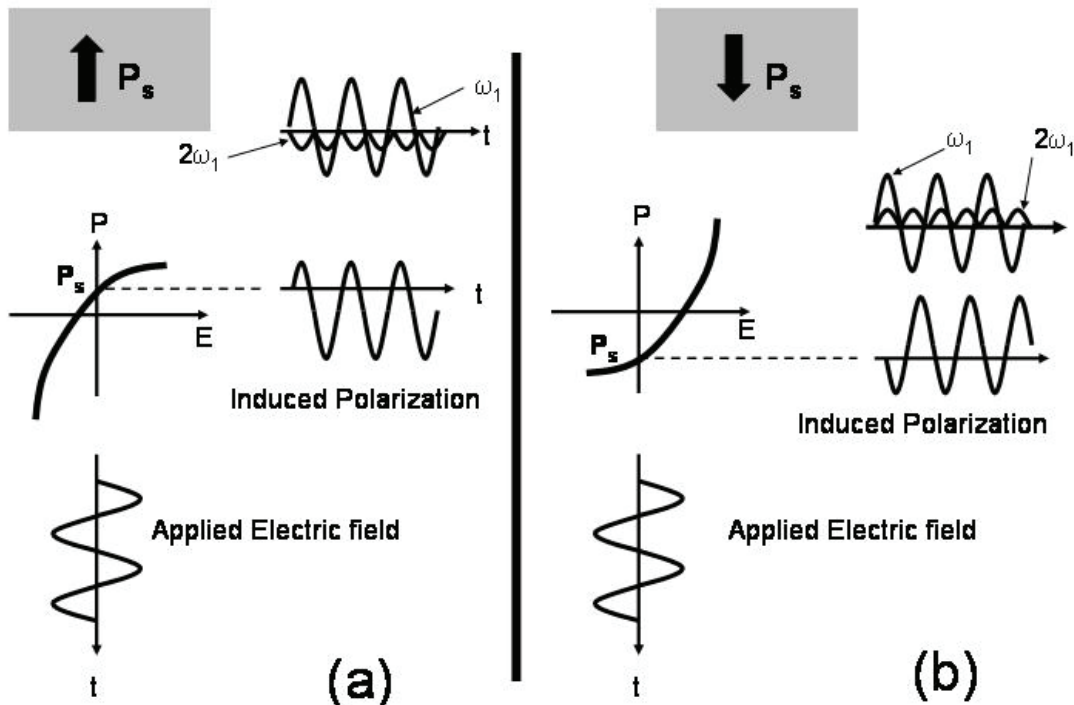
Fig. 2.3 Effect of the spontaneous polarization on SHG. Inversion of P_s from (a) to (b) leads to a 180° phase shift in the generated second harmonic.[8]

2.5. Quasi-phase matched second-harmonic generation

In second harmonic generation two identical photons from a single fundamental pump beam are added and result in a photon having twice the frequency, $\omega_{SH} = 2\omega_F$.
The starting point will be the three coupled wave equations (2.8). In the case of SHG, $\omega_1 = \omega_2 = \omega$ and $\omega_3 = 2\omega$.
The couple wave equations are reduced to two equations, and assuming the material is lossless

$$\frac{\partial E_{2\omega}}{\partial x} = \frac{i\omega}{n_{2\omega}c} d_{eff} E_\omega E_\omega \; exp(-i\Delta kx \;) \; where \; K_{degeneracy} = \frac{1}{2}$$

$$\frac{\partial E_\omega}{\partial x} = \frac{i\omega}{n_\omega c} d_{eff} E_{2\omega} E^*_\omega \; exp(i\Delta kx \;) \; where \; K_{degeneracy} = 1$$

(2.12)

where $\Delta k = k_{2\omega} - 2k_\omega$ and the degeneracy factors have been replaced by its proper value. If we assume that the pump beam can be approximated by a plane wave which is not depleted when it propagates through the material. The intensity of each wave is $I_j = \frac{1}{2}\varepsilon_0 cn_j \left|E_j\right|^2$. The first equation in (2.12) can be integrated over the material distance L giving

$$I_{2\omega} = \frac{2\omega^2 d_{eff}^2 L^2 I_\omega^2}{n_{2\omega} n_\omega^2 \varepsilon_0 c^3} sinc^2\left(\frac{\Delta kL}{2}\right)$$

(2.13)

If now we implement a modulation of the nonlinearity in the material and assume the QPM condition will be fulfilled

$$\Delta k - K_m \approx 0 \Leftrightarrow k_{2\omega} - 2k_\omega \approx K_m \Leftrightarrow \frac{2\omega(n_{2\omega} - n_\omega)}{c} = \frac{2\pi m}{\Lambda}$$

(2.14)

where the period Λ is twice the coherence length L_c for the wave interaction

$$\Lambda = 2L_c = \frac{2m\pi}{k_{2\omega} - k_\omega} = \frac{m\lambda_\omega}{2(n_{2\omega} - n_\omega)}$$

(2.15)

The g(x) function can be inserted into the first equation of (2.12) to see how the growth of the generated field is affected by the modulation of the nonlinearity.[3]

$$E_{2\omega} = \frac{i\omega}{n_{2\omega}c} d_{ijk} E_\omega^2 \int_o^L \sum_{m=-\infty}^\infty G_m \exp(i(K_m - \Delta k_{total})x)dx$$

(2.16)

Thus, the growth will be maximized if $\Delta k_{total} = \Delta k - \frac{2\pi m}{\Lambda} = 0$

2.6. Quasi-phase matched backward SHG

If sufficiently short periods can be created, it is possible to quasi-phase match interactions involving counter propagating beams. The forward QPM SHG configuration can be expressed as $K_m = k_{2\omega} - 2k_\omega$

When the period of a QPM grating goes into the sub-micrometer region, K_m becomes large and the QPM condition can be express as $K_m = k_{2\omega} + 2k_\omega$, thus the second-harmonic wave counter-propagates to the driving wave.

Implementation of QPM backward SHG is the first step towards other QPM interactions involving counter- and back- propagating beams, for example, a backward

wave OPO, with the pump wave counter-propagating the signal and the idler waves, or a backward wave OPG, with the signal counter-propagating the pump and the idler waves.
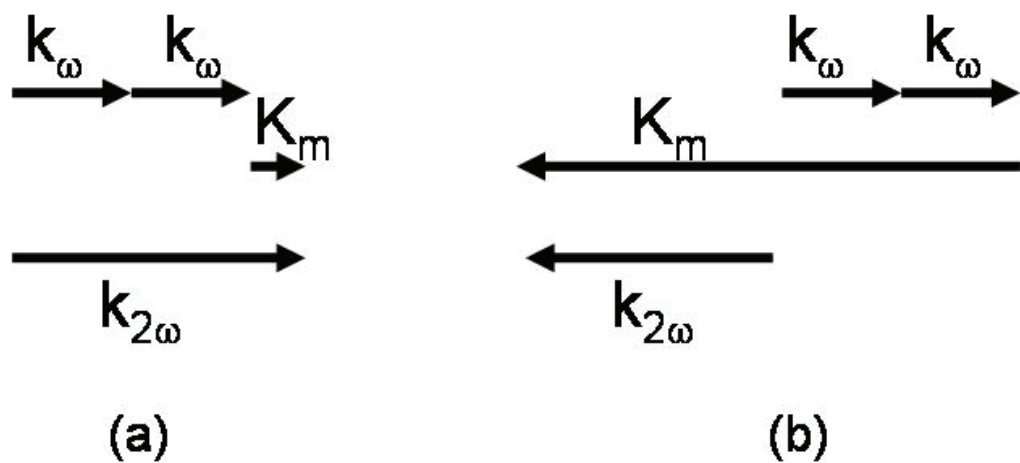
Fig. 2.4. Wave vector diagram for QPM in (a) forward SHG, and (b) backward SHG.

References Chapter 2

[1] P. N. Butcher and D. Cotter, *"The elements of nonlinear optics"*, Cambridge University Press, (1990).

[2] Y. R. Shen, *"The principles of nonlinear optics",* John Wiley & sons, USA (1984).

[3] M. M. Fejer, G. A. Magel, D. H. Jundt, and R. L. Byer, IEEE J. Quantum Electron. 28, 2631 (1992).

[4] L. E. Myers, R. C. Eckardt, M. M. Fejer, R. L. Byer, W. R. Bosenberg, J. W. Pierce, J. Opt. Soc. Am. B, 12, 2102 (1995).

[5] J. Hellström, *"Nanosecond optical parametric oscillators and amplifiers based on periodically poled KTiOPO₄",* ph. D. thesis. ISBN 91-7283-214-2, Royal Institute of Technology, (2001).

[6] L. E. Myers, R. C. Eckardt, M. M. Fejer, R. L. Byer, W. R. Bosenberg, J. W. Pierce, J. Opt. Soc. Am. B, 12, 2102 (1995).

[7] J. A. Armstrong, N. Bloembergen, J. Ducuing, P. S. Pershan, Phys. Rev. 127, 1918 (1962).

[8] W. P. Risk, T. R. Gosnell, A. V. Nurmikko *"Compact blue-green lasers"* Cambridge University Press, UK (2003).

Chapter 2

Chapter 3

Ferroelectricity

3.1. Introduction

In the 19th century several studies[1-3] were carried out to understand pyroelectricity, a phenomena known since ancient times[4]. Such investigations led eventually to the discovery of piezoelectricity by J. Curie and P. Curie[5]. However, the history of ferroelectricity started around 1665 when Elie Seignet of La Rochelle, France, created sodium potassium tartrate tetrahydrate, $NaKC_4H_4O_6.4H_2O$, later known as Rochelle salt. E. Schrodinger was the first to use the term "ferroelectricity" in 1912, although it was not until 1920 that J. Valsek[6] demonstrated that the direction of the spontaneous polarization of Rochelle salt could be reversed by application of an electric field. More than a decade was to pass before a whole series of new ferroelectrics, phosphates and arsenates of potassium were produced. The best known member of this family is KH_2PO_4 (KDP)[7]. It was not until the 40's that ferroelectricity stopped to be view as a rarity when $BaTiO_3$ was found to be ferroelectric.[8] During the same decade, several other members of this structural family as $KNbO_3$[9], $LiNbO_3$ and $LiTaO_3$[10], $PbTiO_3$[11] were shown to also be ferroelectric. From then on, the ferroelectric field has been greatly growing, specially for their interest as ferroelectric random access memories, and more inorganic as well as organic ferroelectric materials have been discovered and studied.

3.2. The structural symmetry

According to Neumann's principle[12], symmetry elements of all physical properties in a crystal should include all symmetry elements of the point group of this crystal. Thus if a physical parameter is subjected to a symmetry operation of the crystal, the value of this physical parameter should remain invariant. In the nature, there are 32 macroscopic symmetry types[13] (point groups or crystal classes) and 11 of them possess a center of symmetry, i.e. the center of positive charge coincides with the center of negative charge

per unit cell. Of the 21 non-centric crystal classes, all except one produce an electric field when subjected to stress. The effect is linear, and it is called the piezoelectric effect. The reverse effect is always present: the crystal contracts or expands when subjected to an external field. Piezoelectric materials can be polarized by applying a mechanical stress or an electric field. Of the 20 piezoelectric crystal classes 10 are characterized by the fact that they have a unique polar axis. Crystals belonging to these classes are called polar because they possess spontaneous polarization or electric moment per unit volume. The spontaneous polarization is in general temperature dependent and it can be detected by observing the flow of charge to and from the surfaces on change of temperature. This is the pyroelectric effect and the 10 polar classes are often referred to as the pyroelectric classes. All ferroelectric materials are a subset of pyroelectric materials in which the direction of the spontaneous polarization can be changed between two or more orientational states by an applied electric field. The orientational states have the same crystal structure, but differ in the direction of the spontaneous polarization at zero applied electric field.

3.3. Basic concepts of ferroelectricity

3.3.1. The polarization and spontaneous polarization

The polarization is the electric dipole moment per unit volume. If the material is represented by a system of bound electric charges of charge density $\rho(\mathbf{r})$, then $\boldsymbol{P}$ is given by

$$\boldsymbol{P} = \int_V \boldsymbol{r}\rho(\boldsymbol{r})dV \tag{3.1}$$

where V is a representative volume containing all the species of interest, and $\boldsymbol{r}$ is the position. A crystal exhibiting spontaneous polarization can be pictured as to be composed of negative and positive ions. In a certain temperature range, these ions are at their equilibrium positions, at which the free energy of the crystal is a minimum, and the center of positive charge does not coincide with the negative one. Thus, each pair of positive and negative ions can be seen as an electric dipole, and the spontaneous polarization (dipole moment per unit volume) as due to an assembly of these dipoles, which point in the same direction. The spontaneous polarization is defined as the magnitude of the polarization within a single ferroelectric domain in the absence of an external electric field and can be written as[14]

$$\mathbf{P_s} = \frac{\iiint \mu dv}{\text{volume}} \tag{3.2}$$

where μ is the dipole moment per unit volume.

The magnitude of P_s in a single crystal is directly related to the atomic displacements that occur in ferroelectric reversal and can be calculated from the atomic positions within the unit cell. Designating Δ_i as the component of the atomic displacement vectors joining

the ith atom positions in the original and reversed orientations along the direction of P_s, Z_i as the effective charge on the ith ion, and V as the unit cell volume, then

$$P_S = \frac{1}{V} Z_i \Delta_i \tag{3.3}$$

Using the definition above, Bierlein et al[15] deduced the P_S value for KTP to be 0.24 C/m^2.

3.3.2. The Pyroelectric effect

The spontaneous polarization varies naturally with temperature giving rise to the pyroelectric effect:

$$\Delta P_{Si} = p_i \Delta T \tag{3.4}$$

where p_i are the components of the pyroelectric tensor.

There are two types of contributions to ΔP_{Si} when the temperature changes: One is due to the thermal expansion of the crystal, which results in its deformation. This contribution is referred as secondary pyroelectric effect. The true or primary pyroelectric effect occurs even when the crystal is prevented from deforming, and is the result of a genuine change in the charge distribution on the change of temperature. The true contribution is usually much smaller than the secondary contribution.

3.3.3. The Curie temperature

Most ferroelectric materials undergo a structural phase transition from a high-temperature nonferroelectric (or paraelectric) phase into a low-temperature ferroelectric phase, of lower crystal symmetry. A ferroelectric phase change represents a special class of structural phase transition denoted by the appearance of spontaneous polarization.

It is generally believed that the ferroelectric structure of a crystal is created by a small distortion of the paraelectric structure such that the lattice symmetry in the ferroelectric phase is always lower than that in the paraelectric phase.[14]

The phase transition temperature is usually called the Curie point (T_C). In most cases, the dielectric constant above this temperature obeys the Curie-Weiss law:

$$\varepsilon = \varepsilon_0 + \frac{C}{(T - T_0)} \quad (T > T_0) \tag{3.5}$$

Where C is the Curie-Weiss constant, and T_0 is the Curie-Weiss temperature which equals the Curie temperature T_C only for second-order phase transition, while in the case of a first order phase transition $T_0 < T_C$. In a first-order ferroelectric-paraelectric phase transition, P_s has a substantial value at temperatures very close to T_C, and undergoes a paraelectric phase in discontinuous transition, whereas in a second-order phase transition, the decrease in P_s as T approaches T_C is more gradual.

3.3.4. Piezoelectricity

The direct piezoelectric effect is equivalent to the appearance of charges when the material is subject to stress. It is described by a linear relationship between the stress X_{ik} applied to a piezoelectric material and the change in polarization

$$\frac{\partial P_i}{\partial X_{jk}} = d_{ijk}^{direct} \tag{3.6}$$

where d_{ijk} is the third-rank tensor of piezoelectric coefficients, measured in [C/N], not to be confused with the nonlinear susceptibility d-tensor of section 2.2.1.

Because strain and stress are symmetrical tensors, the tensor of the piezoelectric coefficients is symmetrical with respect to the corresponding indices, $d_{ijk} = d_{ikj}$ The number of independent piezoelectric coefficients is thus reduced from 27 to 18. The number of independent elements of d_{ijk} may be further reduced by the symmetry of the material. It is worth mentioning that the piezoelectric coefficient d can be either positive or negative.

Also the reverse effect is always present: piezoelectric materials change their dimensions (they contract or expand) when subject to an electric field. The converse piezoelectric effect is described by a linear relationship between the strain x_{ij} developed in a piezoelectric material and the applied electric field E_k:

$$\frac{\partial x_{jk}}{\partial E_i} = d_{jki}^{converse} \tag{3.7}$$

The unit of the converse piezoelectric coefficient is [m/V].

Note that $d_{kij}^{converse} = (d_{ijk}^{direct})^t$ where t denotes the transposed "matrix". The piezoelectric coefficients for the direct and converse piezoelectric effects are thermodynamically identical, i.e. $d^{converse} = d^{direct}$.

Also, when an electric field is applied to a material, it produces a strain proportional to the square of the field. This effect is called the electrostrictive effect, and it is not related to the sign of the applied field. In fact, electrostriction is a result of the polarization induced by the applied field and the electrostricitive strain is directly proportional to the square root of the polarization. Electrostriciton occurs in all materials whether or not they have polarity. The electrostriction can be expressed as[4]

$$x_{ij} = M_{ijkl} E_k E_l \tag{3.8}$$

where M_{ijkl} is the elctrostriction fourth-rank tensor.

3.4 Ferroelectric domains and domain walls

In the absence of an external force, the direction of the spontaneous polarization in an ideal ferroelectric crystal can arise with equal probability along several crystallographic directions of the prototype (paraelectric) phase. The regions of the crystal with uniformly oriented spontaneous polarization are called ferroelectric domains. Domain walls that separate different orientations of the spontaneous polarization vector are called ferroelectric domain walls and those which separate different orientations of the spontaneous strain are called ferroelastic domain walls. A domain wall is a narrow region in which the crystalline structure is disturbed. The angle between polarization vectors in neighboring domains characterizes the domain wall, giving rise to the concepts of 180° walls, 90° walls, etc. From now on, we will only refer to domains with 180° walls.

Because of the structural changes, the energy per unit cell within the domain wall is higher than in the neighboring domains, and it is characterized by a planar wall energy density σ_W. To minimize the electrostatic energy between adjacent domains, the walls should be uncharged.[13] The electrical charge on a domain wall is determined by $\nabla \mathbf{P_s}$. If the mechanical compatibility requirement does not conflict with that of charge neutrality, a charge-neutral wall would have an orientation defined by the unit vector $\boldsymbol{n}$ normal to it such that

$$(\mathbf{P_s} - \mathbf{P_s}') \cdot \mathbf{n} = \mathbf{0} \tag{3.9}$$

Where $\boldsymbol{P_s}$ and $\boldsymbol{P_s}'$ are the spontaneous polarizations in the domains separated by the wall. Thus, a wall would be a charged wall if the component of polarization normal to it is discontinuous across it.

If bound charge of the wall is not satisfying this equation the value of σ_w increases but since it may be to some degree compensated by free carriers, the electric neutrality requirement is not a very serious restriction of the wall orientation. Indeed, walls have often been observed with orientations strongly defying electrical neutrality. However, for domain pairs with antiparallel P_s the prevailing orientation of walls is parallel to the ferroelectric axis.

3.4.1. The depolarization field

An externally applied field $\mathbf{E}$ creates charges on the surface of the crystal. The field produced in the interior of the crystal by these surface charges is called depolarizing field $\mathbf{E}_d$ because it acts in opposition to the applied field as well as to the spontaneous polarization. The surface charge density obeys the Poisson equation, which can be expressed as[13]:

$$\nabla \mathbf{E} = \frac{1}{\varepsilon \varepsilon_0} (\rho - \nabla \mathbf{P_s}) \tag{3.10}$$

Inside the bulk of the ferroelectric P_s has no spatial variation, therefore $\nabla \mathbf{P_S} = 0$, and equation (3.10) reduces to

$$\nabla \mathbf{E} = \frac{\rho}{\varepsilon\varepsilon_0} \qquad (3.11)$$

However, at the vicinity of the crystal surfaces, where P_s decreases to zero, or in the neighborhood of defects, where P_s may have a strong spatial variation, the term $\nabla \mathbf{P_S}$ becomes a major contributor to the depolarizing field. This field can be compensated by the flow of free charge within the crystal:

$$\rho = \int_0^t \sigma \cdot \mathbf{E} \, dt \qquad (3.12)$$

where σ is the electric conductivity of the crystal. On the other hand, free charges in the surrounding medium can compensate for the depolarization field at the crystal surface. Accumulation of surface charge by conduction satisfies the requirement that the electric field vanished both outside and inside the crystal bulk.

The energy associated with the depolarizing field is[13]

$$W_E = \frac{1}{2}\int_V \mathbf{D} \cdot \mathbf{E} \, d\mathbf{r} \qquad (3.13)$$

where D is the electrical displacement and can be expressed as

$$D_i = \varepsilon_0 E_i + P_i = \varepsilon_0 E_i + \varepsilon_0 \chi_{ij} E_j + P_{Si} = \varepsilon_{ij} E_j + P_{Si}$$

where χ_{ij} is the tensor of the susceptibilities, ε_{ij} is the linear dielectric tensor and P and P_s are the total and spontaneous polarization, respectively.*

3.5. Thermodynamic description

Using a thermodynamic approach, it is possible to describe the important features of ferroelectric materials without taking into account the microscopic mechanisms of ferroelectricity. In this way, from the basic thermodynamic relations it follows that the stable phase under a given set of independent variables is the one which minimizes the corresponding free energy. [13]

Assume that the behavior of a ferroelectric is fully described by the six fields, temperature T, entropy S, stress **X**, strain **x**, electric field **E**, and polarization **P**. The fist law of thermodynamics states that the change in internal energy U (per unit volume) when an infinitesimal quantity of heat dQ is received is given by

---

* Keep in mind that if the field is strong, the relation $P_{Ei} = \varepsilon_0 \chi_{ij} E_j$ is not enough to describe the induced polarization and it needs to be substituted by equation (2.1)

Ferroelectricity

$$dU = dQ + dW \qquad (3.14)$$

where dW is total work done on the same ferroelectric body during the quasi-static transformation. The total work done when the ferroelectric is subjected to an infinitesimal change of strain and polarization in the presence of uniform stress and electric field is

$$dW = X_i dx_i + E_i dP_i \qquad (3.15)$$

According to the second law of thermodynamics

$$dQ = TdS \qquad (3.16)$$

Then the internal energy can be express as

$$dU = TdS + X_i dx_i + E_i dP_i \qquad (3.17)$$

where it has been assumed uniform strain and polarization increments over the unit volume.

The three independent variables can be chosen in eight different ways from among the conjugate pairs (T,S), (X_i, x_i) and (E_i, P_i). Thus, there are eight thermodynamic potentials and each of them can be used to generate the equations of state, no additional information being contained in one representation rather than another.[13] From the eight potentials, the Gibbs free energy will be used later on in the chapter:

$$G = U - TS - X_i x_i + P_i E_i \qquad (3.18)$$

and its differential form describing infinitesimal changes is

$$dG = -SdT - x_i dX_i + P_i dE_i \qquad (3.19)$$

Then, for example, the dielelctric permittivity can be obtained as

$$\varepsilon_{ij} = -\frac{\partial^2 G}{\partial E_i \partial E_j}\Big|_{S,X,T} \qquad (3.20)$$

and the piezoelectric tensor as

$$d_{kij} = -\frac{\partial^2 G}{\partial X_{ij} \partial E_k}\Big|_{T} \qquad (3.21)$$

Electrostriction is an example of a third derivative of the Gibbs free energy. The electrostricion tensor can be deduced from

$$M_{ijkl} = \frac{\partial^3 G}{\partial E_k \partial E_l \partial X_{ij}}\Big|_{T} \qquad (3.22)$$

Ferroelectrics can exist in several domain states distinguished by the direction of spontaneous polarization and these states are equivalent in energy. This degeneracy can be removed when an appropriately oriented electric field is applied to a sample of such a material. In general, the relative stability of any of the allowed orientation states is governed by the Gibbs free energy G and its derivatives, equation (3.18) and equation (3.19), respectively.

The entropy term is neglected if the experiments are performed under isothermal conditions. For simplicity, no higher order effects (e.g. electrostriction, and second order nonlinear effects) are included.

Strain x_{ij} is measured relative to the prototype (paraelectric phase) structure and can be written as spontaneous strain $x_{(s)ij}$ plus an induced strain which may arise from applied mechanical stress (elasticity) or from applied electric fields (piezoelectricity).

$$x_{ij} = x_{(s)ij} + s_{ijkl} X_{kl} + d_{kij} E_k \qquad (3.23)$$

Electric polarization can be expanded in a manner similar to strain, with contributions from a spontaneous polarization P_s and several induced effects.

$$P_i = P_{(S)i} + \varepsilon_0 \chi_{ij} E_j + d_{ijk} X_{jk} \qquad (3.24)$$

Substituting the expression for x_{ij} and P_i into the differential form for free energy, combining terms, and integrating gives the thermodynamic potential G, which applies to all orientation states. Let ^1G represent the free energy for the first orientation state and ^2G that for the second; with the tensor terms referred to a common axial system. Then, the driving potential for a state shift is the $\Delta G = {}^2G - {}^1G$. In the absence of external fields and forces, the energy of all orientation states is equal, so that $\Delta G = 0$. Under external forces the difference in free energy for the two orientation states is

$$\Delta G = \Delta x_{(s)ij} X_{ij} + \Delta P_{(S)i} E_i + \frac{1}{2}\Delta s_{ijkl} X_{ij} X_{kl} + \frac{1}{2}\Delta \varepsilon_{ij} E_i E_j + \Delta d_{ijk} E_i X_{jk} \qquad (3.25)$$

where $\Delta x_{(s)ij} = {}^2x_{(s)ij} - {}^1x_{(s)ij}$ is the difference in a certain component of spontaneous strain for orientation states 1 and 2. $\Delta P_{(s)i}$ is the difference in the i*th* component of spontaneous polarization for the two domains. The difference in elastic compliance coefficients is represented by Δs_{ijkl}. The remaining terms in (3.25) arise from differences in electric susceptibility, and from differences in piezoelectric coefficients.

3.6. Polarization reversal and hysteresis loop

An important characteristic of ferroelectrics is the hysteresis loop, i.e a P-E curve. P is a double-value function of the applied electric field. A typical hysteresis loop is shown in fig 3.1. At very low fields and at very high fields a ferroelectric crystal behaves like an ordinary dielectric (usually with high dielectric constant), but at the so-called coercive field E_c polarization reversal occurs giving a large dielectric non-linearity. The area within the loop is a measure of the energy required to twice reverse the polarization. At zero field, the polarization within a single domain (saturated value of the polarization) has two values corresponding to the opposite orientations of the spontaneous polarization. Poling of a ferroelectric is a process in which a unipolar electric field is applied to switch one of the two thermodynamically stable (saturated) states (represented by $+P_s$ and $-P_s$) in to other. The energy required for polarization reversal is given by equation (3.25).[13]
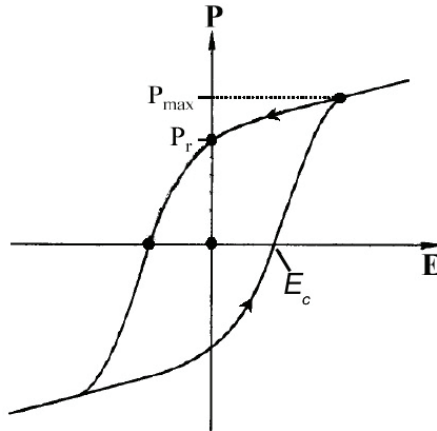
Fig. 3.1. Typical ferroelectric hysteresis loop.

The coercive field is usually defined as the field at which half the polarization has reversed. However, it depends not only on temperature, but also on the measuring frequency, the type of electrodes used to contact the crystal and on the waveform of the applied voltage, which makes it difficult to measure.

In general, the processes involved in ferroelectric domain switching by an external applied electric field are nucleation (i.e. the formation of nuclei, small domains with antiparallel polarization) and growth of these new antiparallel domains, growth of existing domains, and domain merging. The domains can either grow along the polar direction or by sideways motion.

According to Hayashi's model[16,4], and assuming the polarization and local field with in the nucleus to be uniform, the total energy change upon nucleation of new domains is

$$\Delta W = \sigma_W A + W_E - \mathbf{D} \cdot \mathbf{E} \, V \tag{3.26}$$

where σ_W and W_E are the wall energy and the depolarization energy of a dagger-type nucleus of area A, and $\mathbf{D} \cdot \mathbf{E}$ represent the electrostatic energy of the volume V.

The rate of domain nucleation is proportional to $\exp(-\Delta W/kT)$. From energy considerations, the probability of nucleation of domains by thermal fluctuations in the bulk of a crystal is very small compared to that of the surfaces or in inhomogeneities sites or at existing domain walls.

For low fields, Hayashi's analysis[16] gives an exponential field dependence for the nucleation rate, $1/\tau$:

$$1/\tau \sim e^{-(\delta/E)} \tag{3.27}$$

Where δ is fairly independent of E.

The wall velocity can depend on nucleation rate or on the growth velocity of the nucleus.

Unless the applied field is very large, nucleation of new domains is expected to be only one lattice-spacing thick. They spread along with different velocities in different directions. This growth of the domain wall parallel to its own plane can be quite fast because of the ledges and kinks available for the easy growth of regions with the new polarization orientation. Real sideways movement of an existing domain wall is not a very probable mechanism, since the energy required for a ferroelectric domain wall to move by one lattice spacing is not very different from the wall energy itself. Also, the energy gained by the process of domain wall movement by one lattice spacing is not very large.[4] The more likely mechanism is that sideways motion occurs by nucleation of two dimensional reversed step-like domains on existing 180° walls. However, in real materials the process is somewhat more complicated than this. For example multiple nuclei can grow on already growing steps of earlier nucleation. This is illustrated in Fig. 3.2.
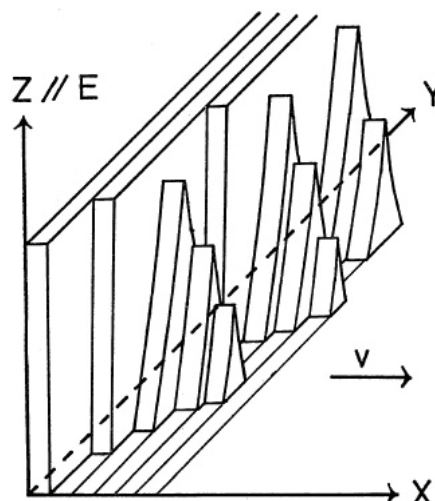

Fig. 3.2. Schematic drawing showing growth of nuclei on the steps formed by earlier nucleations.[16]

In the high field regime, the apparent wall velocity depends not only on the rate of nucleation, but also on the growth velocity of the already formed nuclei. Hayashi's analysis[4,16] showed that the exponential field dependence is replaced by a power law dependence. This is due to the change of relative importance of nucleation and sideways growth of nuclei on the wall.

3.6.1. Free carriers and defects

Free carriers play an important role in ferroelectrics. Ultimately, they compensate for the depolarization fields by conduction, which leads to single domain formation. In most cases they also contribute to stabilize the domain patterns.
Defects in any crystalline lattice generally cause deformation of the surrounding volume and modification of the local fields. Assume that in an acentric site a defect has a dipole

moment $\Delta\mu$. If the defect concentration N is sufficiently dilute that the interaction between them can be neglected, the macroscopic polarization change is

$$\Delta P = N\Delta\mu \tag{3.28}$$

During poling, the ΔP due to the defects may or may not reverse. If it does reverse, then the coercive field will depend on both the field required to switch the defects and the sign and magnitude of ΔP. In general, the presence of defects tends to increase the coercive field. If all the dipoles have the same sense the hysteresis loops will appeared biased. If the dipoles are completely random then the loop will appeared with an increased coercive field.

Defects may induce the existence of frozen-in nuclei (small regions in which the preferred direction of $\mathbf{P}_s$ is never changed and which serve as kernels at the reorientation process), and defects that prefer a particular orientation of $\mathbf{P}_s$ can lead to backswitching.

References Chapter 3

[1] D. Brewster Edinbg, J. Sci, 1, 208 (1824).

[2] J. M. Gaugain, C. R. Acad. Sci. Paris, 42, 1264 (1856).

[3] S. B. Lang, "Pyroelectricity:from ancient curiosity to modern imaging tool", Phys. Today, August pp31 (2005).

[4] V. K. Wadhawan "*Introduction to Ferroic materials*", Gordon and Breach Science Pulbishers, The Netherlands (2000).

[5] J & P Curie, C. R. Acad. Sci. Paris, 91, 294 (1890).

[6] J. Valsek, Phys. Rev.,15, 537 (1920).

[7] G. Busch & P. Scherrer, Naturwissenschaft, 23, 737 (1938).

[8] E. Wainer & S. Solomon, Titanium alloys Manufacturing Co. Reports 8 and 9 (1942).

[9] B. T. Matthias, Phys. Rev.,75, 1771 (1949).

[10] B. T. Matthias & J. P. Remeika, Phys. Rev.,76, 1886 (1949).

[11] G. Shirane, S. Hoshino, K. Suzuki, Phys. Rev.,80, 1105 (1950).

[12] J. F. Nye "*Physical properties of crystals*", Clarendon Press, Osxford, (1964).

[13] M. E. Lines and Glass, "*Principles and application of ferroelectrics and related materials*", Oxford university press, (1977).

[14] Yuhuan Xu, "*Ferroelectric Materials and Their Applications*". North-Holland, Amsterdam, (1991).

[15] J.D. Bierlein and C. B. Arweiler, Appl. Phys. Lett. 49, 917(1986).

[16] M. Hayashi, J. Phys. Soc. Japan 33, 616 (1972).

Chapter 4

Properties of KTiOPO$_4$

4.1. Introduction

Synthesis of KTP crystals was first published in 1890 by L. Ouvard[1], but it wasn't until 1976 that KTP was introduced as a nonlinear optical material.[2] Since then, KTP crystals have been widely used for frequency-doubling of 1064 nm Nd:YAG lasers using Type II phase matching[3]. Bierlein *et al*.[4] first reported fabrication of waveguides in KTP using ion exchange in molten nitrates of Rb, Cs, and Tl. In 1990, Van der Poel *et al*[5] achieved highly efficient QPM SHG by domain inversion resulting from the ion-exchange process. During the 90's, several groups reported bulk periodic poling in both hydrothermal and flux-grown KTP by various techniques like room temperature electric-field poling[6], electron beam direct writing[7], low temperature poling[8], or chemical patterning[9]. Compared with LiNbO$_3$, KTP has a lower nonlinearity but greater resistance to optical damage and photorefraction. Moreover, its coercive field is one order of magnitude lower than that of congruent LiNbO$_3$, and its anisotropic structure limits the domain broadening.

4.2. The crystallographic structure

KTP is orthorhombic and belongs to the acentric point group mm2, and space group Pna2$_1$[10]. The lattice constants[11] are a = 12.819 Å, b = 6.399 Å, c = 10.584 Å., where the c-axis is the direction of the spontaneous polarization. Following the conventional labeling in the literature[12], the crystallographic axes a, b, and c correspond to x, y, and z axes of the dielectric tensor.

Each primitive cell contains four asymmetric units with two formula units of KTiOPO$_4$. The crystal network consists of TiO$_6$ octahedra chains corner-linked by PO$_4$ tetrahedra bridges. The slightly distorted TiO$_6$ octahedra forms helical chains along the [001] direction with alternating long and short Ti-O bonds. The three-dimensional

framework formed by the PO_4 tetrahedra and the Ti octahedral results in channels along the [001] direction where the K ions are located. The K ions are weakly bonded to both the octahedral and the tetrahedral groups, and can occupy two non-equivalent sites: either eight-fold coordinated (K1) or nine-fold coordinated (K2). Due to the arrangement of alternating Ti-O bond-lengths along the chain direction, a net c-directed polarization is induced.
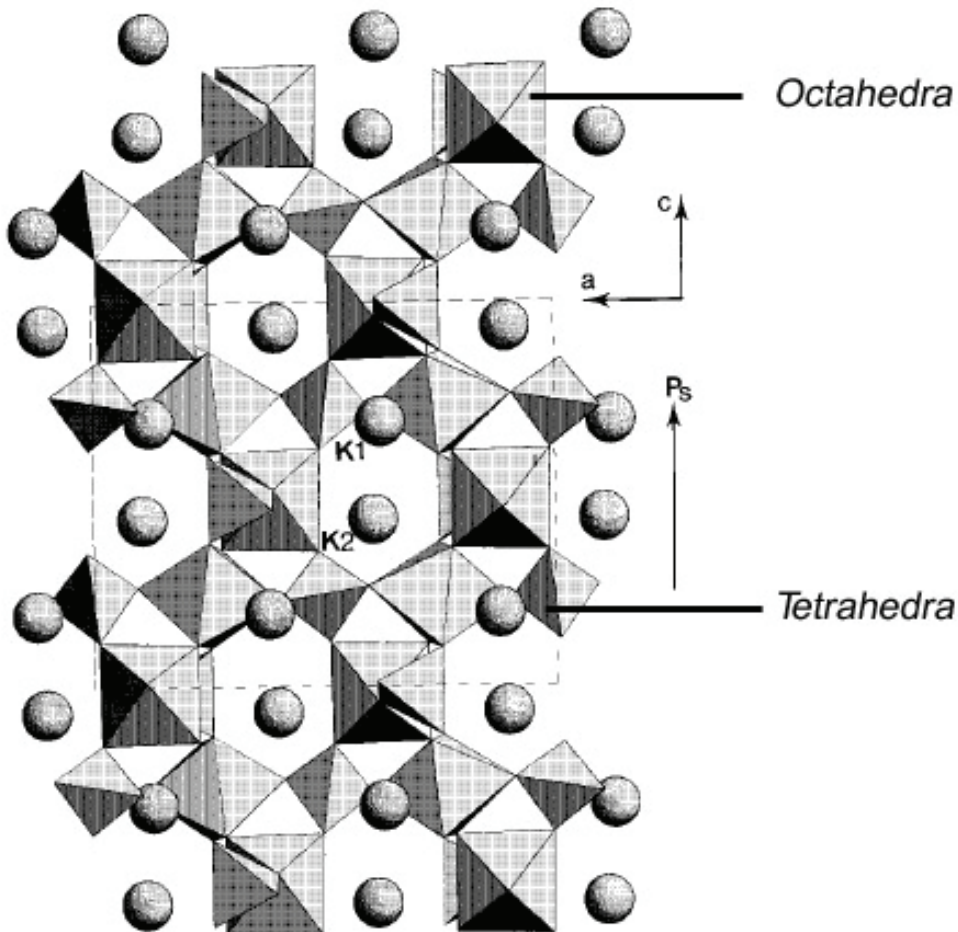

Fig 4.1 Crystallographic structure of KTP.[13]

It has not been yet clarified which bonds in the KTP crystals are the main responsible for the optical nonlinearity. Zumsteg *et al*[14] concluded that the short Ti–O bonds in the helical chain that are the major contributors and that the other Ti–O bonds as well as the PO_4 and K– O groups will contribute to a lesser extent. On the other hand, Xue and Zhang[15] presented the PO_4 tetrahedra and the K–O groups as the origin of the nonlinearity. The results in *paper A* support the idea that the nonlinearity comes mainly from Ti-O bonds.

KTP undergoes a ferroelectric phase transition[16] at 934 °C, above which the structure becomes centrosymmetric. During the transformation from the paraelectric to the ferroelectric phase, the alkali metal ions are significantly displaced along the polarization vector and fall into the two independent sites, namely K1 and K2.

It has been proposed by Stolzenberger *et al.*[17] that the domain inversion takes place by shifting the alkali ions in the $-c$ direction, i.e., the nine-coordinated cations become eight-coordinated and vice versa. At the same time, the TiO$_6$/PO$_4$ framework is forced to adjust: the short Ti-O bonds become long and the long ones, short, while the PO$_4$ tetrahedra and the TiO$_6$ undergo only a slight rotation with respect to each other.

For the other KTP isomorphs the formula unit is written MTiOXO$_4$, where M is K, Rb, or Cs, and X can be either P or As. The structures of the different isomorphs are very much like the KTP one.

4.3. Growth techniques

For KTP and its isomorphs, there are two major growth techniques, hydrothermal and flux.[18]

The hydrothermal process consists of sealing nutrient and seed crystals in a gold tube, and inserting the tube into an autoclave where crystal growth takes place. Dissolution of aqueous solvents at high temperature and high pressure is carried out in the hot nutrient zone. The material is transported via convection currents into the cooler growth zone where crystallization takes place. The hydrothermal process is performed at ~350-600 °C and high pressure (1-2 kbar) for about 3 weeks.

The flux growth technique is a high-temperature (700-1000 °C) solution growth process in which KTP crystallizes when the molten flux is cooled. The flux is a solvent of the components of the crystal. The operation of flux growth is performed at atmospheric pressure in an accurately temperature controlled furnace (better than ±0.05 °C) to avoid crystal defects due to growth striations and flux inclusions. For KTP growth, crystal growth starts in the supersaturated melt and continues while the temperature constantly decreases. Small crystals are made by spontaneous nucleation in the flux, while large crystals are grown from a seed inserted into the flux. For seeded growth, there are two slightly different methods, submerged seeded solution growth (SSSG) and top seeded solution growth (TSSG). The crystal site should be at the coldest spot in the flux to avoid secondary nucleation. Rotation of the crystal or the crucible prevents secondary nucleation by convection. Also, periodic reversal of the rotation direction avoids asymmetrical flow rates and flux inhomogeneity. The main differences between flux and hydrothermal growth are the pressure and the fact that the flux solidifies before reaching room temperature.

If the growth is carried out below the T$_C$ of the material, the resulting crystal will be single domain and if grown above T$_C$, will result in a multidomain formation.[19]

4.4. The Dielectric properties

The dielectric properties of KTP are dominated by the highly anisotropic K-ionic mobility in the quasi-one dimensional channels along the c direction through a hopping mechanism via vacancies. The thermally activated K-ion can hop to the neighboring site by passing through a "bottleneck" formed by the oxygen atoms.[20] The intrinsic barrier height of the ionic hoping is determined by the size of the "bottlenecks", which are widest in the polar axis[21], resulting in an ionic conductivity along the c-axis at least four orders of magnitude larger than along the a-b plane.

(●, ■) flux grown crystals; (○) high temperature hydrother- mally grown crystals; (□) low temperature hydrothermally grown crystals. The measurements were made at room temper- ature.
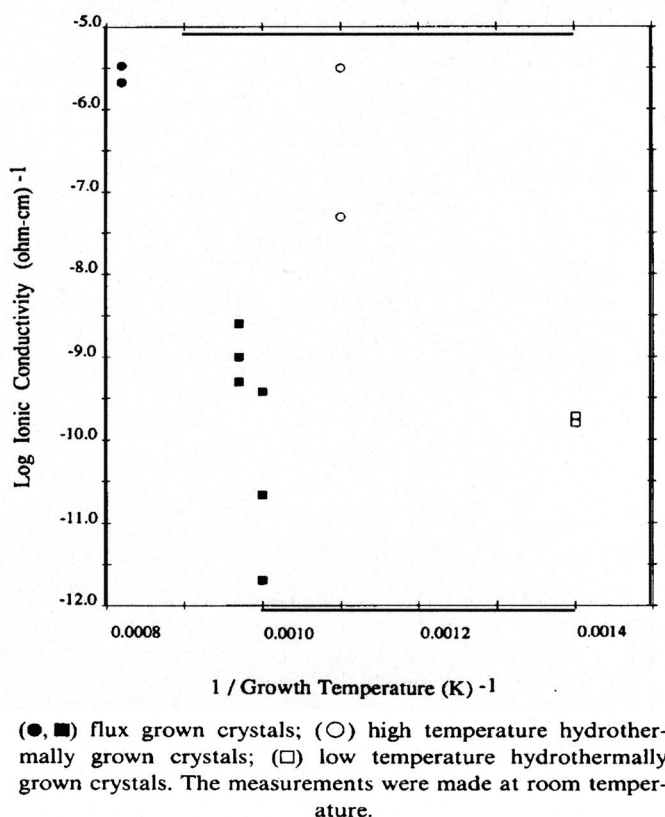
Fig 4.2. Bulk ionic conductivity plotted as a function of the reciprocal midpoint growth temperature for KTP crystals grown by the flux and hydrothermal techniques. [22]

The ionic conductivity of KTP is found to vary by four to five orders of magnitude, depending on the crystal growth technique and conditions of growth[22]. Impurity analysis of KTP crystals grown by several techniques revealed no correlation to the ionic conductivity of the material, and the variation in ionic conductivity is attributed to nonstoichiometric defects on the K and O sites. It has been shown that the concentration of nonstoichiometric defects in KTP is a strong function of the range of temperatures used for the growth.[22] At elevated crystal growth temperatures oxygen

tends to escape from the KTP crystal and leaves the total charge unbalanced. In order to compensate for the charges that the oxygen left behind, some positively charged species have to be expelled from the crystal, leaving behind potassium vacancies together with oxygen vacancies.

4.5. The optical properties

Since KTP belongs to the crystal class mm2, only five coefficients of the electro-optic tensor are non-zero. Its values, measured at λ=633 nm are[12]

$$
\begin{bmatrix} 0 & 0 & r_{13} \\ 0 & 0 & r_{23} \\ 0 & 0 & r_{33} \\ 0 & r_{42} & 0 \\ r_{51} & 0 & 0 \\ 0 & 0 & 0 \end{bmatrix} = \begin{bmatrix} 0 & 0 & 9.5 \\ 0 & 0 & 15.7 \\ 0 & 0 & 36.6 \\ 0 & 9.3 & 0 \\ 5.3 & 0 & 0 \\ 0 & 0 & 0 \end{bmatrix} \text{[pm/V]}
$$

(4.1)

The nonlinear susceptibility tensor takes the form

$$
\begin{bmatrix} 0 & 0 & 0 & 0 & d_{15} & 0 \\ 0 & 0 & 0 & d_{24} & 0 & 0 \\ d_{31} & d_{32} & d_{33} & 0 & 0 & 0 \end{bmatrix}
$$

(4.2)

The nonlinear susceptibility coefficients for different wavelengths are collected in table 4.1.

	d_{31}	d_{32}	d_{33}	d_{24}	d_{15}
@ 1064nm [pm/V][23]	2.4	4.4	16.9	7.6	6.1
@ 532 nm [pm/V][24]	1.4	2.65	10.7	2.65	1.4

Table 4.1.Nonlinear susceptibility coelfficients for KTP.

Accurate prediction of suitable QPM periods for a given wavelength requires knowledge of the exact refractive index. For light polarized in z-direction and propagating along the *x*-axis, the relevant refractive index can be express in the form of Sellmeier equation as:

$$
n_z{}^2(\lambda) = A + \frac{B}{1 - \frac{C}{\lambda^2}} + \frac{D}{1 - \frac{E}{\lambda^2}} - F\lambda^2
$$

(4.3)

For KTP, several dispersion data in the form of Sellmeier equation can be found in the literature. Fan *et al.*[25] have reported very precise dispersion relations for KTP for wavelengths below 1 μm:

$$
n_z{}^2(\lambda) = 2.25411 + \frac{1.06543}{1 - \frac{0.05486}{\lambda^2}} - 0.02140\lambda^2
$$

(4.4)

where the wavelength λ should be in μm.

For wavelengths above 1 μm, the data published by Fradkin-Kashi et al.[26] gives best results.

The index of refraction is also temperature dependent due to the thermo-optic effect. The temperature derivative can be approximated by a Laurent series. Wiechmann et al.[27] give the following equation for KTP:

$$\frac{\partial n_z}{\partial T} = \frac{12.415}{\lambda^3} - \frac{4.735}{\lambda^2} + \frac{8.711}{\lambda} + 0.953 \quad \left(\frac{10^{-6}}{°C}\right) \tag{4.5}$$

The transmission of KTP and its isomorphs has been measured by Hansson et al.[28] For KTP, the ultraviolet cut-off wavelength is 0.365 μm, and in the infrared part around 4.3 μm. The absorption in the high transmission window is less than 0.6%/cm. However, it presents an enhanced absorption close to 2.8 μm which is related to OH⁻ groups trapped in the crystal during growth.
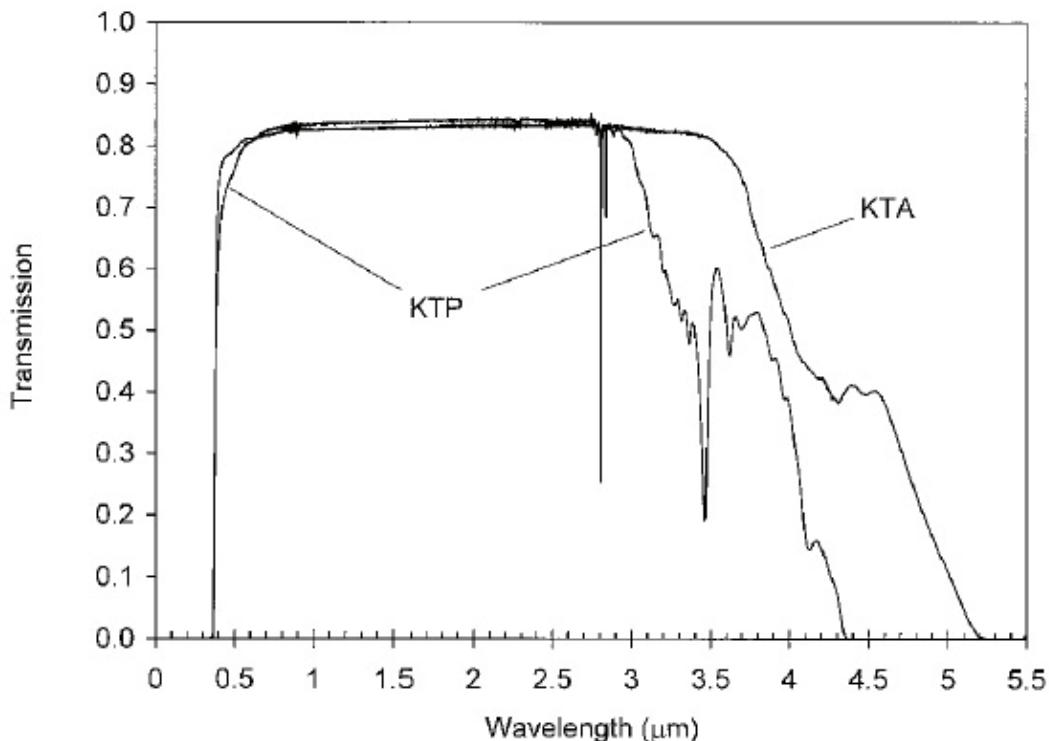
Fig 4.3. Transmission window for KTP and KTA. No compensation for the Fressnel losses were made.[28]

An important issue when choosing a crystal for nonlinear optical applications is its resistance to optical induced damage. Photorefractive damage occurs when optically excited free carriers in the crystal get trapped outside the optical beam and set-up an internal field which distorts the beam via the electro-optic effect. KTP presents several orders of magnitude higher resistance to photorefraction than $LiNbO_3$, which has to be operated above 100 °C, whereas KTP can be used at room temperature. A reason for that is the high ionic conductivity of KTP, which might contribute to quickly redistribute the free carriers.

Properties of KTiOPO$_4$

Also, compared to LiNbO$_3$, KTP presents higher threshold to material breakdown, which is caused by induced strain from high peak intensities via local temperature increase in the material. However, high intensities of visible radiation in the blue-green spectral region induce absorbing color-centers in the crystal partially associated with formation of Ti^{4+}, so-called gray tracks.[29]

References Chapter 4

[1] L. Ouvrad, M. Troost, Compt. Rend. 121, 117 (1890).

[2] F. C. Zumsteg, J.D. Bierlein and T.E. Gier, J. Appl. Phys. 47, 4980 (1976).

[3] Y. S.Liu, D. Dentz, and R. Belt, Opt. Lett.9, 76 (1984).

[4] J. D. Bierlein, A. Ferreti, J. H. Brinxter, and W. Y. Hsu, Appl. Phys. Lett. 50 1216 (1987).

[5] C. J. van der Poel, J.D. Bierlein, J.B. Brown and S. Colak, Appl. Phys. Lett. 57, 2074 (1990)

[6] H. Karlsson, F. Laurell, Appl. Phys. Lett. 71, 3474 (1997).

[7] M.C. Grupta, W. P. Risk, A. C. G. Nutt, Appl. Phy. Lett. 63, 1167 (1993).

[8] G. Rosenman, A. Skliar, M. Oron and M. Katz J. Phys. D:Appl. Phys., 30, 277 (1997).

[9] W. P. Risk, asn S. D. Lau, Appl. Phy. Lett. 69, 3999 (1996).

[10] I. Tordjman, R. Masse, and J. C. Guitel, Z. Kristallogr. 139, 103 (1974).

[11] P.A. Thomas, and A. M. Glazer, J. Appl. Cryst. 24, 968 (1991).

[12] J. D. Bierlein and H. Vanherzeele, J. Opt. Soc. Am. B. 6, 622 (1989).

[13] Z. W. Hu, P. A. Thomas, and P. Q. Huang Phys. Rev. B. 56, 8559 (1997).

[14] F.C. Zumsteg, J.D. Bierlein, T.E. Gier, J. Appl. Phys. 47, 4980, (1976).

[15] D. Xue, S. Zhang, Appl. Phys. Lett.70, 943, (1997).

[16] V.K. Tanovskii and V. I. Voronkova, Phys. Status Solidi A 93, 665 (1980).

[17] R. Stolzenberger and M. Scripsick, Proc. SPIE 3610, 23 (1999).

[18] J. Nordborg, *"Non-linear optical titanyl arsenates, crystal growth and properties"* ISBN 91-7197-882-8, Ph. D-thesis, Chalmers University of Technology (2000).

[19] K. Hutton, R. C.C. Ward, K.W. Godfrey, Mater. Res. Soc. Symp. Proc. 329, 23, (1994)

[20] S. Furusawa, H. Sugiyama, F. Itoh, A. Miyamoto and T. Sasaki, J. Phys. Soc. Japan 62, 183 (1993).

[21] C.V. Kannan, S. Ganesamoorthy, C. Subramanian, and P. Ramasamy, International J. Modern Phys. B. 17, 373 (2003).

[22] P.A. Morris, J. Crys. Growth 106, 76 (1990).

[23] L. K. Cheng, L. T. Cheng, J. Galperin, P. A. Morris Hotsenpiller, and J. D. Bierlein, *J. Crystal Growth*, 137, 107 (1994).

[24] B. Boulanger, J. P. Fève, G. Marnier, B. Ménaert, X. Cabriol, P. Villeval and C. Bonnin, J. Opt. Soc. Am. B 11, 750 (1994).

[25] T. Y. Fan, C. E. Huang, B. Q. Hu, R. C. Eckardt, Y. X. Fan, R. L. Byer, and R. S. Feigelson, Appl. Opt. 26, 2390 (1987).

[26] K. Fradkin-Kashi, A. Arie, A. Skliar, and G. Rosenman, Appl. Phys. Lett., 74, 914 (1999).

[27] W. Wiechmann, S. Kubota, T. Fukui, and H. Masuda, Opt. Lett., 18, 1208 (1993).

[28] G. Hansson, H. Karlsson, S. Wang, and F. Laurell, Appl. Opt. 39, 5058 (2000).

[29] B. Boulanger, I. Rousseau, J. P. Fève, M. Maglione, B. Ménaert, and G. Marnier, IEEE J. Quantum Electron., 35, 281 (1999).

Chapter 4

Chapter 5

Domain characterization

5.1. Introduction

Several techniques exist to inspect domain structures in KTP, for instance, electrostatic toning, which utilizes the pyroelectric effect[1], electro-chemical etching[1], second harmonic imaging[2], X-ray based techniques[3], scanning electron microscopy[Paper C], etc. For visualization of the periodic poling *in-situ,* an electro-optic imaging method by launching a He-Ne laser through the *b*-face of a crystal was recently developed.[4] In this chapter, the techniques employed during this work to inspect the domain structure in KTP used in this work are described.

5.2. Chemical etching

The easiest and quickest way to evaluate the domain structure is by chemical etching. Chemical etchants have been found for many ferroelectrics that etch the positive and negative ends at a different rate revealing, thus, the domain structure.[5]

Laurell et al. found that molten salts containing hydroxide attack the negative face (c^-), while the positive face is left essentially untouched. Etching involves both elements of electrostatic interactions of the etching ions with the bound charge of domains and the response of the etching agent to the defect structure of the sample. Cations in the etchant diffuse toward the surface of negatively charged domain outcrops (i.e., c^+ end). The ions deposited on them give rise to a shielding layer hindering further dissolution. The anions are attracted by positively charged surface of domain end (i.e., c^-). The reaction taking place between absorbed and surface ions results in the formation of a chemisorption complex. The further stages of the etching process are determined by the solubility of compounds and by chemical bonding between crystal ions and the complex and by bonding of the complex with the solution.[6]

The etchant used for KTP has been a mixture of KOH and KNO$_3$ (2:1 mole ratio) in water at 80 °C for a time typically between 5-15 min. This solution not only permits to visualize domain structure, it also allows visualization the defect structure. Fig 5.1. shows a the domain structure on the c- face of a KTP crystal. Growth striae can be seen in the *c* regions.
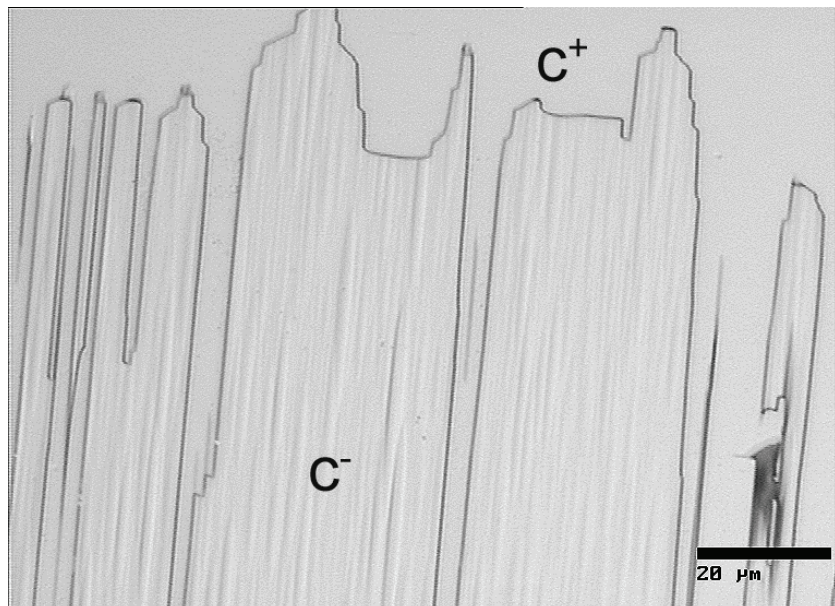
Fig 5.1. Domain structure on a KTP crystal. Growth striae can be seen in the c regions.

Etching reveals the domain configuration only at the polar faces of the crystal, since the *b*- and *a*- faces remain uncharged in KTP. This can be overcome by polishing the crystal at an angle to the *c*-face, for example at 45°.[7] However, as we will show later, atomic force microscopy becomes more useful for investigating the domain structure on the *b*-face of the crystal. A drawback of etching is that the method is destructive.

5.3. Atomic force microscopy
5.3.1. The basic principles

The operation principle of an atomic force microscope (AFM) is based on the detection of the bending of a flexible cantilever when the sharp tip at its end is brought in contact with, or near, the surface to be imaged. Forces between the tip and the sample surface cause the cantilever to bend, or deflect, according, in a first approximation, to the Hook's law. The deflection, Δz, of the cantilever is proportional to the force, F, acting on the tip, F=-kΔz, where k is the spring constant of the cantilever. The deflection of the cantilever is usually monitored by collecting a laser beam reflected by the end of the cantilever into a position sensitive photodetector (PSPD) As the cantilever bends, the position of the laser beam on the PSPD shifts. As the sample is scanned under the tip, a feed-back loop keeps the deflection of the cantilever or the tip-surface force constant, and a three-

dimensional map of the surface topography can be obtained. The measured cantilever deflections allow a computer to generate a three-dimensional map of the surface topography. Fig. 5.2 shows the essential elements of an AFM. Several forces typically contribute to the deflection of an AFM cantilever. The dependence of the force upon the distance between the tip and the sample is shown in Fig. 5.3. In general, long range interactions are dominated by attractive forces, while the short range forces are dominated by repulsive interactions. When the AFM is operated with a tip-sample separation of a few nanometers, the long range attractive forces –predominantly Van der Waals forces- dominate. These attractive forces diminish, with increasing tip-sample separation, at much slower rate than the repulsive forces. When the separation between the tip and the sample is reduced to less than a nanometer, the repulsive forces dominate, and it is said that the AFM is operated in contact mode. These forces are localized mainly to the very apex of the tip (in the ideal case to the single outermost atom) and the long range forces are integrated over the entire tip. Another useful mode is the so-called tapping™ mode[8]. In this case, the cantilever with the tip is oscillated at its resonance frequency and the height is adjusted so that the tip touches the sample surface only for a short period of time. If the tip encounters an elevation, the oscillation amplitude will decrease and the feedback control rises up the cantilever until the oscillation amplitude reaches the initial value.
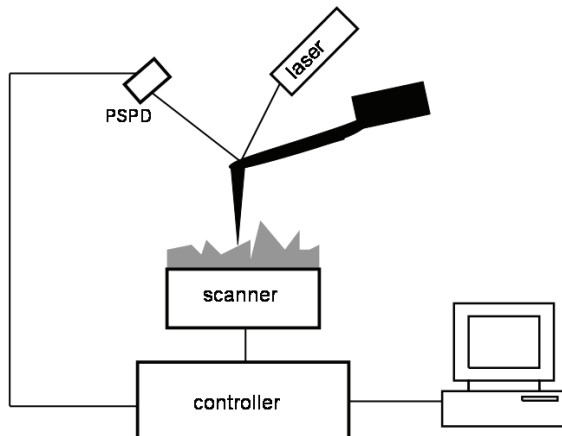
Fig. 5.2. The essential elements of an AFM
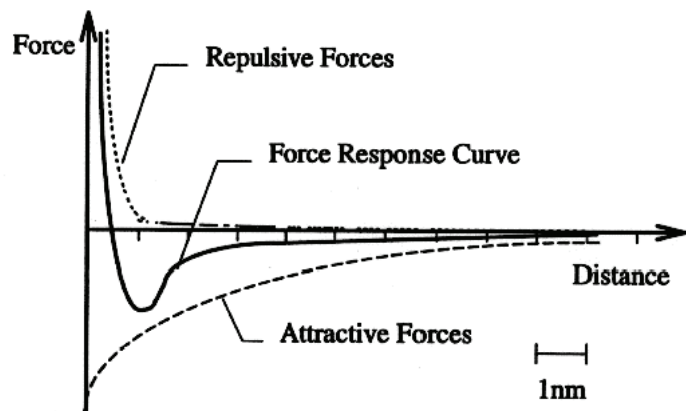
Fig. 5.3 The dependence of the force upon the distance between the tip and the sample[9].

5.3.2. Domain imaging by AFM

Obviously, AFM can be used to study the surface relief obtained by etching the sample, gaining in resolution compared to optical microscopy. An example can be seen in Fig. 5.4.
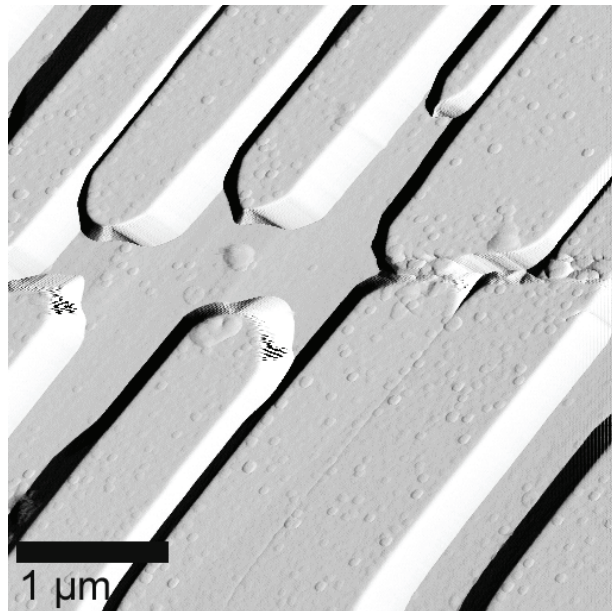
Fig. 5.4. AFM image of the etched domain structure in a KTP sample.

AFM-based techniques to visualize ferroelectric domains make use of basic properties of ferroelectrics such as their elastic or piezoelectric behavior and/or presence of surface charges associated with the spontaneous polarization. For example, electrostatic force microscopy (EFM) has been used to study periodically poled $LiNbO_3$ structures[10]. Measurements are taken in two passes across each scan-line. First, topographical data is taken in tapping mode on one pass. The tip is then raised to the final scan height and a second trace and retrace performed while maintaining a constant separation between the tip and local surface topography. Then a constant voltage is applied between the tip and the sample and the cantilever bending is then related mostly to electrostatic forces. The resolution obtained by the EFM method is around 50 nm.

Voltage-modulated AFM, or also called piezoresponse-AFM, has proven to be the most suitable AFM-based method to study ferroelectric domain structures achieving 1 nm resolution. In this imaging technique an a.c. voltage is applied between an Au-coated tip and the sample. Due to the electromechanical coupling –via the converse piezoelectric effect- the surface locally deforms –oscillates- when in contact with the tip. The deformation will be out of phase for domains with opposite orientations. When the tip is scanned in contact mode, its deflection signal contains the induced oscillations of the sample surface transmitted to the tip-cantilever. These electrical oscillations can be extracted from the global deflection signal using a lock-in amplifier. The lock-in detection rules out any other harmonic components of the deflection signal and the

piezoelectric oscillations are in this way separated from the topography. The technique allows investigation in the polar faces crystal as well as in the non-polar ones.

Fig. 5.5 depicts the voltage-modulated AFM set-up.
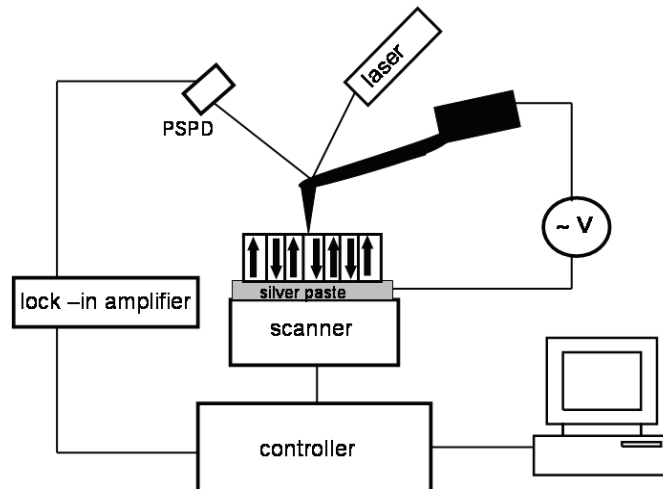
Fig. 5.5 The voltage-modulated AFM set-up.

Detection on the polar faces

The electric field generated in the sample causes the domains with opposite polarization to oscillate out of phase. The surface movements underneath the tip are given by:

$$\Delta z(t) \propto d_{33}\, \text{sgn}(P_z)\cos(\omega t) \tag{5.1}$$

Therefore, opposite orientations of polarization along the *c*-axis cause the sample surface to vibrate out of phase under a small AC voltage. Fig 5.6 illustrates the imaging mechanism of the voltage modulated AFM on the polar faces.
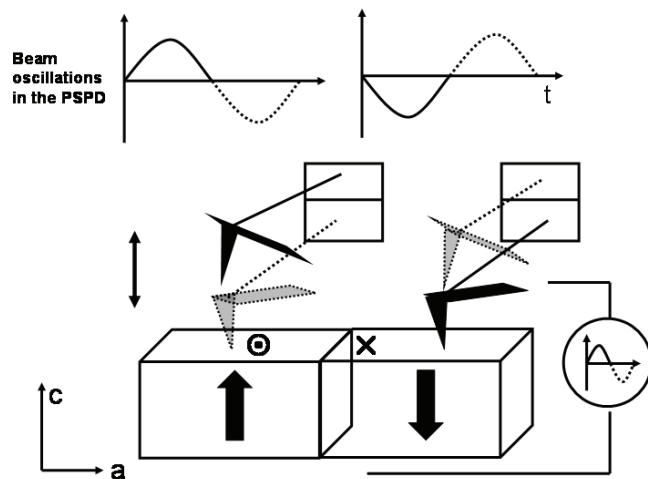
Fig. 5.6. The imaging mechanism of the voltage modulated AFM on the polar faces.

The response of the sample measured at the first harmonic, i.e., at the frequency ω, is related to the inverse piezoelectric effect. The phase shift of the response at ω characterises the sign of the polarization vector, while the amplitude is related to the magnitude of the polarization vector. The response at the second harmonic is related to the electrostrictive response of the sample.[11-14]

Figure 5.7 shows AFM images of the *c*-side of a PPKTP crystal (that was metallized during poling). The essentially featureless topology of the crystal surface is shown in (a).

In figure 5.7(b) the phase at the first harmonic (ω) of the vertical deflection is shown. The phase shift between the domains of alternating contrast in this image is 180°, it can thus be concluded that the domains have opposite directions of polarization. The amplitude of the vertical deflection at the first harmonic (ω) was also investigated. It was found that the amplitude gave similar contrast as the phase, although, in general at a somewhat weaker signal level. Ideally, the amplitude at the frequency ω should be uniform all over the surface, since the polarization should have the same magnitude in both directions. However, a shift in amplitude associated with the phase shift could be expected since the relation between amplitude and frequency is usually not linear for a complex system such as an AFM tip in contact with an oscillating surface. Nevertheless, a difference in amplitude between the domains could indicate that there is a difference in the magnitude of the effects of polarization in the domains polarized in the two opposite directions.
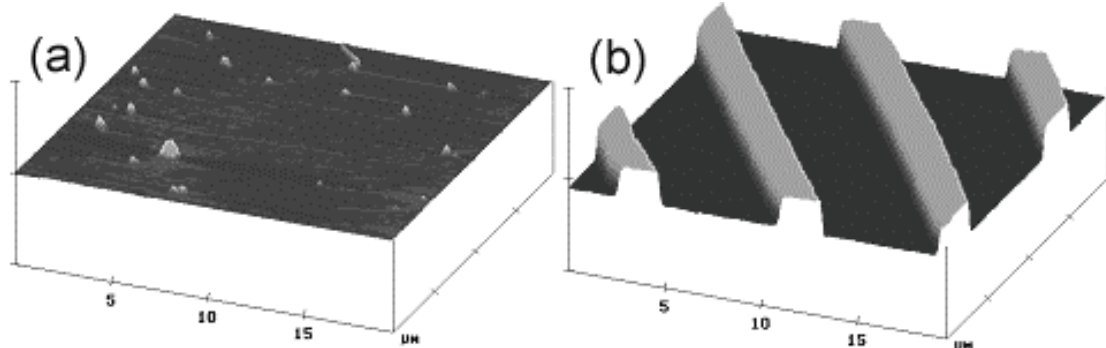
Fig 5.7. Inverse piezoelectric response AFM images: (a) topographic image showing a featureless surface. (b) phase of the vertical deflection at the first harmonic showing domains with opposite directions of polarization. All micrographs are over an area of 20×20 μm^2.

In this same configuration, Contrast at the domain walls was given by the lateral deflection of the tip, as shown in Fig. 5.8(a). This contrast can be understood by considering the strain of the crystal lattice in the area constituting the domain wall; as the neighboring domain walls are oscillating in opposite directions the domain wall is trying to follow the motion of both domains, much like a rubber band tied between two moving parts. When the AFM-tip is scanned over the area of the domain wall, it will thus

be pushed sideways, as shown in fig. 5.8(b). At the first harmonic, the contrast caused by the amplitude was weaker than the phase shift contrast. The brightness-darkness contrast depends in both cases on the scanning direction, i.e., on the relative angle between cantilever and domain walls. The largest contrast was obtained when the relative angle between the cantilever and the domains was 45°. At 90° the contrast nearly disappeared, and at 0°, some domain walls became invisible because lateral deviation of the cantilever at those angles was not detectable.
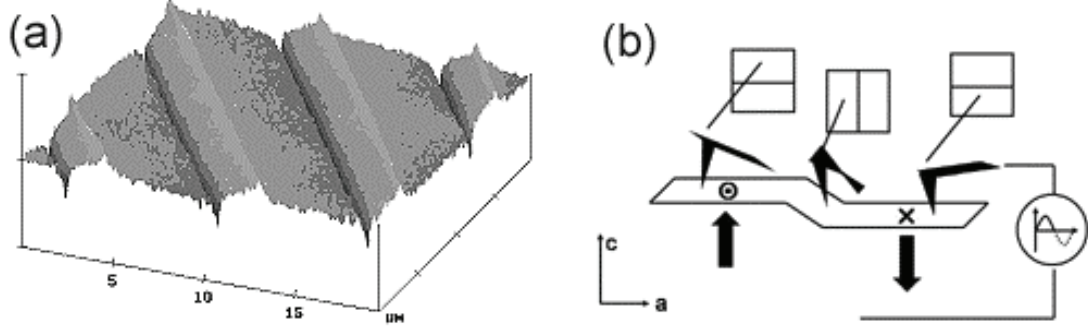
Fig 5.8 (a) Phase of the lateral deflection at the first harmonic showing the domains wall;. (b) the mechanism of lateral deflection on the polar faces. As the neighboring domains oscillate in opposite directions the AFM tip is pushed sideways in the area of the domain wall, where the surface is bent by the motion of the domains

Detection on the non-polar faces

If the polarization vector is perpendicular to the electric field, there is no piezoelectric deformation along the field direction, but a shear strain appears in the KTP, brought about by the only non-zero piezoelectric coefficient d_{24}, leading to displacements of the sample surface parallel to itself, along the polarization direction. The in-plane displacements of the surface are transferred *via* friction to the AFM tip as lateral movements, as can be seen in Fig 5.9. The amount of lateral deflection can be expressed as:

$$\Delta L \propto -d_{24} \, \text{sgn}(P_z)V_0 \cos(\omega t) \qquad (5.2)$$
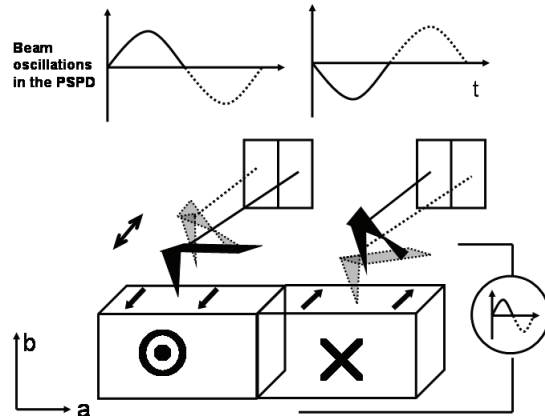
Fig 5.9 The imaging mechanism of the voltage modulated AFM on the non- polar faces.

This in-plane movement is phase-shifted for domains with opposite polarization. So, with the field applied along the *b* direction, no oscillations of the crystal surfaces induced by the diagonal tensile strain components are expected, since $d_{23}=0$ and $d_{22}=0$ for KTP. This was corroborated experimentally by the fact that no domain contrast was observed for the phase of the vertical deflection of the cantilever. The same principle was recently used by Eng *et al*[15] to map the three dimensional polarization distribution in $BaTiO_3$.

Fig. 5.10(a) shows the featureless topology of the *b*-face of the PPKTP sample on the edge with the c^+-patterned side. The top blurred area is the edge, where the tip lost contact. The corresponding phase map of the first harmonic of the AFM tip lateral deflection signal can be seen in Fig. 5.10(b). For the applied voltage frequency range of 60 – 90 kHz, the lighter contrast corresponds to the polarization-switched regions, whereas the darker represents the original polarization orientation. Below 60 kHz the contrast could invert.
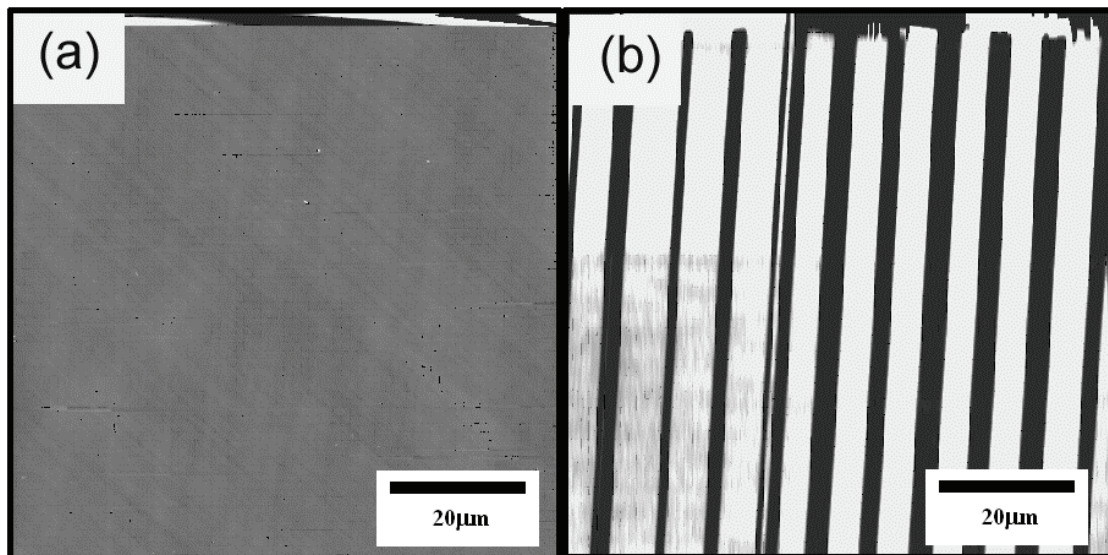
Fig 5.10 AFM images: (a) topographic image of the b-face showing a featureless surface; (b) The corresponding phase of the lateral deflection showing the domains over the same 100 ×100 μm area.

Domain wall width measurements

Voltage modulated AFM has also been used to study the domain wall width of KTP on both polar and non-polar faces. Fig 5.11 shows scans over an area of 600×600 nm^2 across a domain wall on the polar face of a PPKTP crystal. In Fig 5.11(a) is shown the phase response of the vertical deflection at the first harmonic (ω). Fig. 5.11(b) shows a line profile across the domain wall shown in fig. 5.11(a). The domain wall width, defined here as the width from 25% to 75% of the full transition, is found to be around 40 nm for this sample. The width of the full transition is approximately 200 nm. Figure 5.11(c) shows the phase response of the lateral deflection at the first harmonic (ω), of the same domain wall as in fig. 5.11(a). In fig. 5.11(d) a line profile across the domain wall shown in fig 5.11(c) is shown, the domain wall width, given here as the full width at half maximum (FWHM) is found to be ~66 nm. The domain wall widths of KTP samples were found to range between 20 and 80 nm, depending on the details of fabrication of the sample. Most typically the domain wall width was ~40 nm.
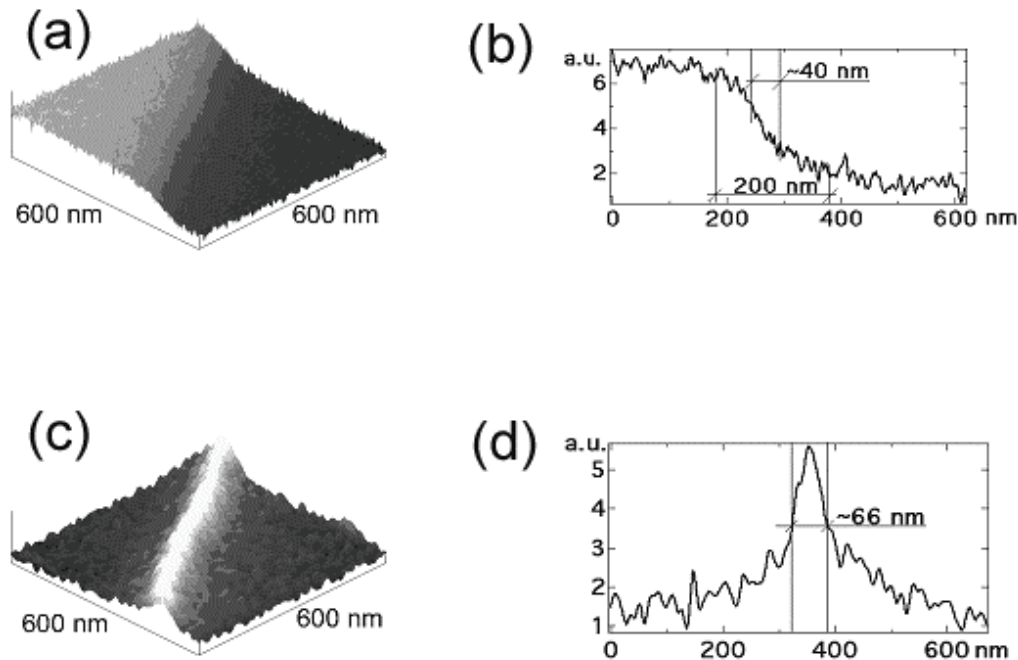
Fig. 5.11. 600×600 nm² scans across a domain wall in the KTP crystal. (a) The phase response of the vertical deflection at the first harmonic (ω); (b) a line profile across the domain wall show the domain wall width to be ~40 nm; (c) the phase response of the lateral deflection at the first harmonic (ω) of the same domain wall as in (a). (d) A line profile across the domain wall show the domain wall width (FWHM) to be ~66 nm.

Fig. 5.12 shows a detail of the end of a domain tip imaged at the *b*-face. Domain tips in KTP have the shape of a dagger always pointing opposite to the original direction of polarization. The domain wall width of the tip has been measured (as 25% to 75% of the transition) at its end and on the sides far from the tip-end. At the sides, the width is ~64 nm, whereas the front wall (perpendicular to the polarization direction) is around ~180 nm.
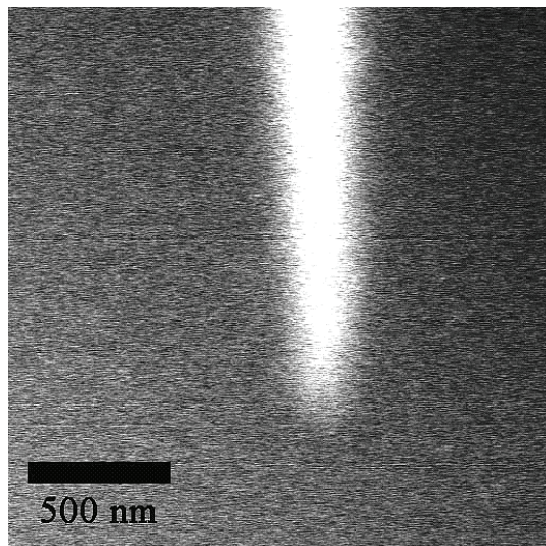
Fig. 5.12 A detail of the end of a tip on the b-face in KTP. At the sides, the domain wall width is ~64 nm, whereas the front wall (perpendicular to the polarization direction) is around ~180 nm.

Do these widths make sense? Theoretical calculations on 180° domain walls suggest that they may be just a few unit cells[16]. Pernot-Rejmánková et al[17] concluded that for KTP it might be a single P atom which acts as the linking atom for connecting inverted domains across the wall.

On the other hand, unexpectedly wide regions of strain which are strongly correlated with the presence of nonstochiometry in the crystal were found in domain walls in $LiNbO_3$ and $LiTaO_3$.[18, 19] In situ X-ray synchrotron experiments of individual domain walls strains under the external fields in $LiNbO_3$ showed that extended domain wall strains develop over 10-50 μm around the wall at fields an order of magnitude below the coercive field[20].Thus, some questions arise: Can the applied voltage on the tip broaden, at least apparently, the domain wall? Can the domain wall be broadened due to nonstoichiometry and/or to stresses induced when the domain is being switched? The large difference between the front wall and the side wall in KTP domain tips was explained by the presence of charges at the front wall and of large strains in the front wall that are needed to sustain the tail-to-tail configuration. [PAPER V]

We have not been able to answer these questions yet. Thus, the observed widths should be treated, for the time being, as upper limits.

5.4. Digital holography

Digital holography (DH) was recently successfully used[21] for *in-situ* full-field visualization of the domain reversal process in congruent LiNbO$_3$ by employing electro-optically induced phase-difference in ferroelectric domains with opposite polarity.

In this work a similar interferometric technique based on DH has been used to study the growth and kinetics of 180° domains in flux-grown KTP under an external electric field. The KTP sample, held between two Plexiglas chambers with quartz windows, was inserted in one arm of a Mach-Zehnder type interferometer with a frequency doubled Nd:YAG (532 nm) laser beam traversing the sample along its *c*-axis direction. The plane object wave passing through the sample, interferes with the reference wave at the surface of a CMOS camera with (512×512) pixels, 12 μm sized and 900 frames/s acquisition rate (see Fig 5.13). [22-24].
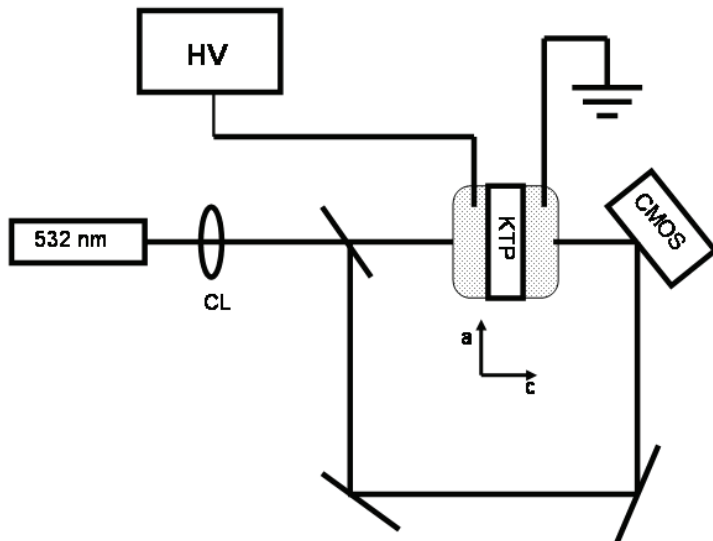
Fig 5.13 The Mach-Zehnder type interferometer with a frequency doubled Nd:YAG laser beam traversing the sample along the KTP c-axis direction. The plane object wave passing through the sample, interferes with the reference wave at the surface of a CMOS.

With an external electric field E_3 applied along the c-axis of KTP, a laser beam with the wavelength λ traversing the sample along the same axis and polarized parallel to the *a*-axis experiences a phase change of

$$\Delta\phi = \pi L n_1^3 r_{13} E_3 / \lambda \qquad\qquad (5.3)$$

where L is the crystal length along the *c*-axis and r_{13} is the appropriate element of the electro-optic tensor. In a multidomain sample containing 180° domains the phase difference experienced by the laser beam in areas with opposite direction of spontaneous

polarization will be equal to $2\Delta\phi$. During electric field poling, an incident plane wave experiences a phase shift, mainly due to the linear electro-optic effect. A reference interferogram of the sample at its initial virgin state is acquired without external voltage. With respect to this, the two-dimensional (2D) phase shift distribution experienced by the object field during poling is calculated. The DH reconstruction[22] is performed for both the reference hologram and the nth hologram recorded during the domain switching, to obtain the corresponding object field phase distributions $\phi_0(x,y)$ and $\phi_n(x,y)$. The 2D map of the induced phase shift $\phi_n(x,y) - \phi_0(x,y)$ is calculated for each hologram and the corresponding images are collected into a frame sequence, which gives information about the spatial and temporal evolution of domain reversal.

The results obtained by DH will be presented in next chapter.

References Chapter 5

[1] F. Laurell, M.G. Roelofs, W. Bindloss, H. Hsiung, A. Suna, J.D. Bierlein, J. Appl. Phys. 71, 4664 (1992).

[2] S. I. Bozhevolnyi, J. M. Hvam, K. Pedersen, F. Laurell, H. Karlsson, T.Skettrup, M. Belmonte, Appl. Phys. Lett. **73**, 1814 (1998).

[3] Z. W. Hu, P. A. Thomas, W. P. Risk, Phys. Rev. B 14, 14259 (1999).

[4] J. Hellström, R. Clemens, V. Pasiskevicius, H. Karlsson, and F. Laurell, J.Appl. Phys. 90, 1489 (2001).

[5] M. E. Lines and Glass, "*Principles and application of ferroelectrics and related materials*", Oxford university press, (1977).

[6] N. R. Ivanov, et al. Crystallography reports, 39,593 (1994).

[7] P. Urenski, M. Molotskii, and G. Rosenman, Appl. Phys. Lett. 79, 2964 (2001).

[8] Trademark from Digital Instruments, Veeco.

[9] Burleigh instruments, Inc., "Personal atomic force microscope operating manual", Fishers, NY, USA (1994).

[10]. H. Bluhm *et al.,* Appl. Phys. Lett. 71, 146 (1997).

[11] A. Gruverman, O. Auciello, H. Tokumoto, Appl. Phys. Lett. 69, 3191 (1996).

[12] K. Franke, J. Besold, W. Haessler, C. Seegebarth, Surf. Sci. Lett. 302, L283 (1994).

[13] M. Tyunina et al., Appl. Phys. Lett. 74, 3191 (1999).

[14] E. L. Colla et al., Appl. Phys. Lett. 72, 2763 (1998).

[15] L. M. Eng, H-J. Güntherodt, G.A. Schneider, U. Köpke, and J. Muñoz Saldaña, Appl.Phys.Lett. 74, 223 (1999).

[16] V. K. Wadhawan "Introduction to Ferroic materials", Gordon and Breach Science Pulbishers, The Netherlands, (2000).

[17] Pernot-Rejmánková, P.A. Thomas, Pl. Cloetens, T. Lyford, J. Baruchel, J. Phys.: Condens Matter 15, 1613 (2003).

[18] S. Kim, B. Steiner, and V. Gopalan, Appl. Phys. Lett. 77, 2051 (2000).

[19] S. Kim, V. Gopalan, A. Gruverman, Appl. Phs. Lett. 80, 2740 (2002).

[20] T. Jach, S. Kim, V. Gopalan, S. Durbin, and D. Bright, Phys. Rev. B 69, 064113, (2004).

[21] Grilli, P. Ferraro, M. Paturzo, D. Alfieri, and P. De Natale Opt. Expr. 12, 1832 (2004).

[22] U.Schanrs and W. Jüptner, Meas. Sci. Tech. 13, R85 (2002).

[23] S. Grilli, P. Ferraro, S. De Nicola, A. Finizio, G. Pierattini and R. Meucci, Opt. Expr. 9, 294 (2001).

[24] M. de Angelis, S. De Incola, A. Finizio, G. Pierattini, P. Ferraro, S. Grilli, and M. Paturzo, Appl. Phys. Lett. 85, 2785 (2004).

Chapter 6

Polarization switching characteristics of bulk KTiOPO$_4$

6.1. Introduction

Understanding the mechanisms of domain inversion in KTP is crucial in order to be able to control the periodic poling and to achieve a reasonable yield. Therefore, characterization of the polarization reversal parameters such as coercive field, switching time, domain morphology, and domain growth velocity is of utmost importance. For KTP and its isomorphs these parameters have not been studied in detail. The available data[1, 2] refers mainly to low temperature properties, where KTP have gone from the superionic to the dielectric state[3].

A systematic study of the poling properties at room temperature and in air to achieve knowledge of the different factors governing the switching characteristics becomes essential. In order to throw some light on all this matter, three different kinds of studies have been carried out for KTP with plain (non periodic) electrodes:

- Electrical studies, devoted to characterization of macroscopic properties as coercive field and switching time.
- Etching studies, to study the domain morphology adopted in all the poling steps.
- Dynamic studies, to visualize *in situ* the domains evolution as the switching process takes place.

Some of these properties have been also studied for RbTiOPO$_4$ [PAPER III], finding that this material behaves essentially in the same way as KTP.

6.2. Studies of KTP under the electric field
6.2. 1.The poling circuit

The electric circuit shown in Fig. 6.1 was used for all the electrical studies, and periodic poling experiments. A high voltage amplifier (Trek 20/20C) amplifies a waveform generated by an arbitrary signal generator (Agilent 33120A). A serial resistance R_1, limits the current passing through the sample during poling. The voltage over the sample is determined through U_1 which is the voltage over R_3, which forms a voltage divider parallel to the sample. The resistance R_2, is chosen to give appropriate voltages for the oscilloscope. The current through the sample is determined from U_2 which is the voltage over the small resistance R_4 in series with the sample. The R_1, R_2, R_3, and R_4 are set as 15 kΩ, 100 MΩ, 100 kΩ, 10 kΩ,respectively.
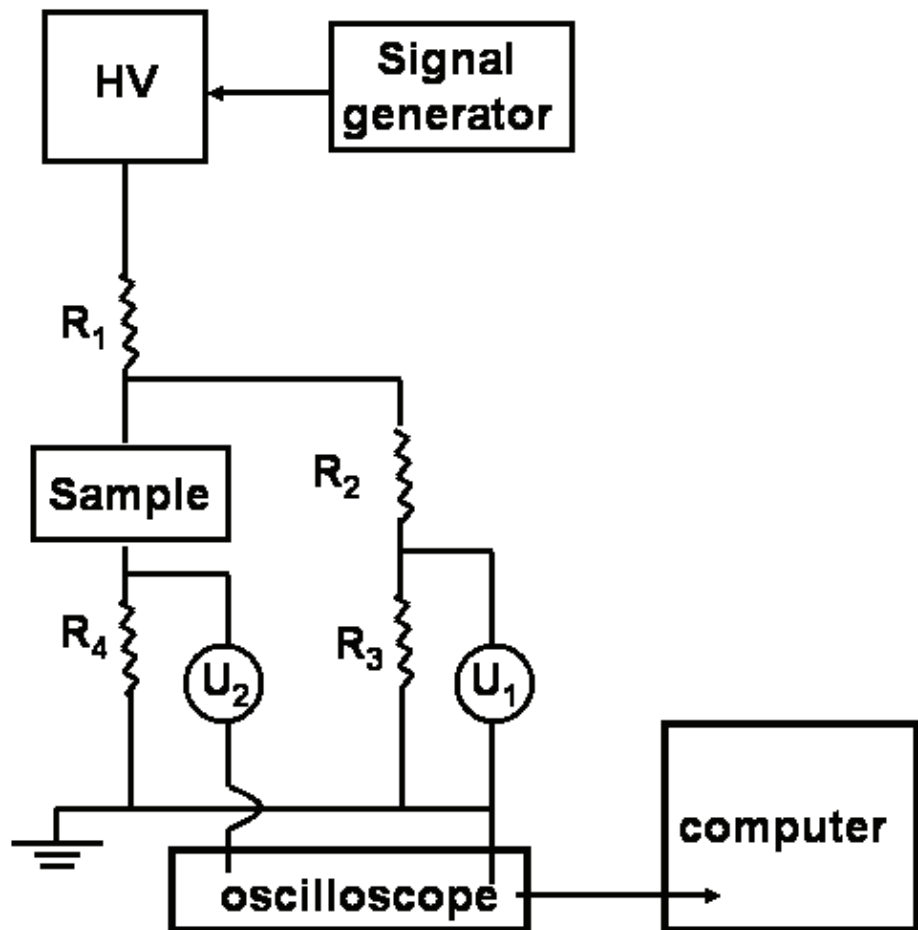
Fig. 6.1 The electrical circuit used for all the poling experiments

6.2. 2. The ionic conductivity

In flux-grown KTP, the ionic conductivity along the c-axis can vary by as much as an order of magnitude over a single wafer.[4] Therefore, we first map the conductivity distribution on each wafer. 5 ms long positive square electrical pulses of 1.5 kV in magnitude are applied to the c^--face of the wafer using an In-covered probe of 1 mm in diameter, while the c^+-face is uniformly contacted using a nearly-saturated solution of KCl. The probe electrode is scanned over the wafer surface, measuring the ionic current through the resistor R_4.

A typical measured ionic-current map of a KTP wafer, which illustrates the conductivity distribution can be seen in Fig. 6.2. The measured current of 100 μA yields an absolute value of the conductivity at 1 mm^2 of about 8.5 X 10^{-7} S/cm. It shows a parabolic variation along the b-axis, increasing by a factor of 2 from the edges to the center, whereas it remains almost constant along the a-axis. The variation in conductivity over the KTP wafer is most probably due to a temperature gradient during crystal growth that results in a spatially varying stoichiometry[5]. We define two different types of KTP samples: sample LC-KTP, coming from the edges of wafers whose conductivities are relatively low; and samples HC-KTP, from the central regions of the wafers, with high conductivity.
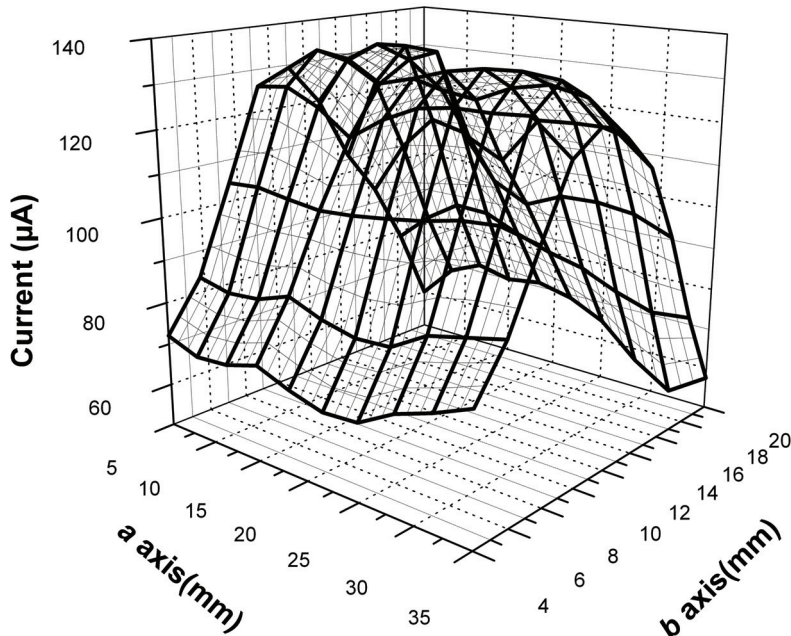
Fig. 6.2. Conductivity map of KTP showing the ionic current variation over the wafer.

6.2. 3. The coercive field

In order to achieve polarization reversal in area, A, a charge $Q = 2P_s A = \int i \cdot dt$ needs to be deposited over this area. This will cause a poling current i to flow through the external electrical circuit. In low-conductivity ferroelectrics such as LiNbO₃ the domain inversion can be controlled by monitoring the current flowing in the poling circuit and the integration of the current determines the deposited charge over a specific area. For high conductive ferroelectrics, like those from the KTP family, the applied field leads to a strong ionic current passing through the sample, which screens the poling current and makes of current monitoring an inaccurate technique for following the poling. However, it is still possible to determine the coercive field by observing a substantial increase or peaking in the current when the applied voltage is linearly ramped. In this work, in order to determinate the coercive field of the different samples, triangular electrical pulses were used to reverse the spontaneous polarization. Contacts with the samples were made with a nearly saturated solution of KCl. One of the benefits of using triangular-shaped pulses is that the voltage increase rate is time constant. Assuming that the charge transport in KTP is determined by a single species of ions, the resulting current-voltage characteristic will include the space-charge-limited current which can be approximated by the Mott-Gurney quadratic law and the polarization switching current. Then the total measured current density can be expressed as[6,7]

$$J = \frac{9}{8}\varepsilon\varepsilon_0\mu\frac{U^2}{L^3} + 2P_s\frac{1}{A}\frac{\partial A_i}{\partial t} \qquad (6.1)$$

where ε is the permittivity of the material, ε_0 is the permittivity of the vacuum, μ is the ionic mobility, L the thickness of the crystal and A_i is the area of the inverted domains. During the linear voltage ramp, the measured current will show a quadratic rise over the whole pulse due to the ionic current, while the polarization switching current will rise sharply at the voltage corresponding to the coercive field. The poling current should self-terminate when the whole area A under electrode is reversed. A clear poling current peak can be observed by choosing the voltage ramp rate such that

$$\frac{\partial U}{\partial t} < \frac{8P_s L^3}{9\varepsilon\varepsilon_0\mu A}\frac{\partial^2 A_i}{\partial t^2} \qquad (6.2)$$

Relatively slow rates make the RC response negligible. Since the maximum electric field of the triangular pulses was set higher than the expected coercive field, the poling current peak can be clearly identified. We have chosen to define the coercive field as the field where the switching peak reaches its maximum value.

Figures 6.3 show an example of the current flow during the forward and reverse poling pulse for (a) LC-KTP and (b) HC-KTP. In both cases, the ionic current caused by the mobile K^+ ions dominates the samples current response. Nevertheless, a clear switching peak can be distinguished.
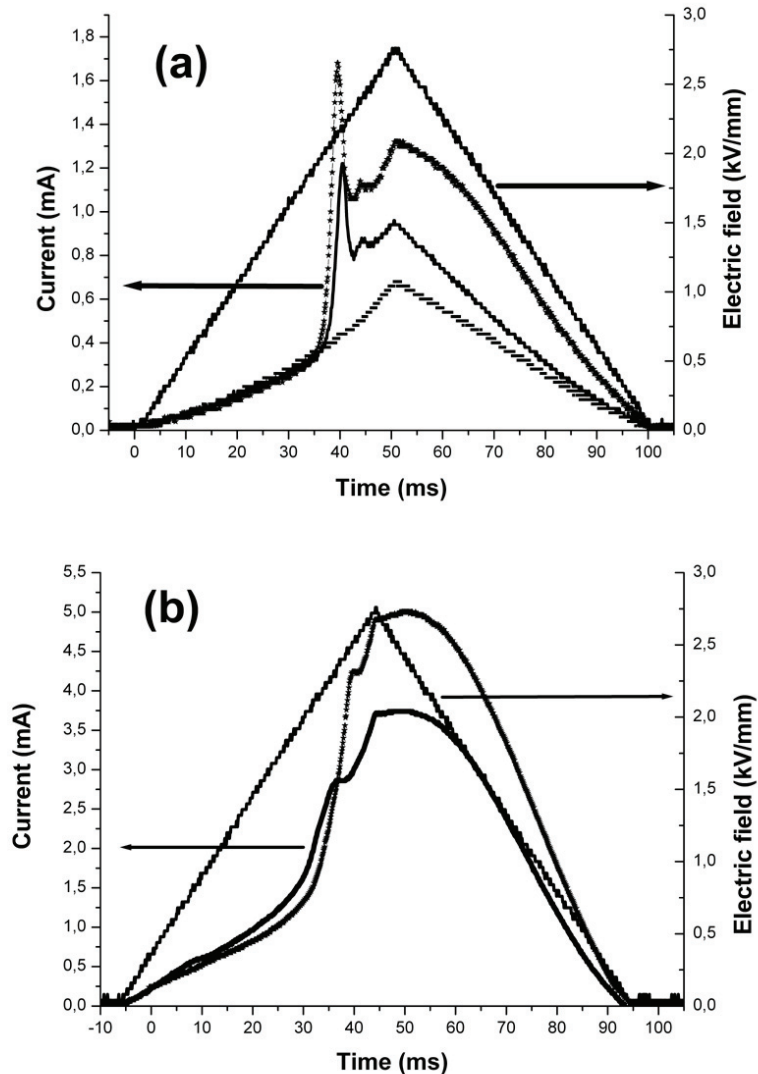
Fig. 6.3.Applied triangular electrical pulse and corresponding current flow for (a) LC-KTP, and (b) HC-KTP. The dotted line in Fig (a) is taken after the first forward poling. Since domain switching was finished the first forward pulse, there is no switching peak in the dotted line.

The coercive field obtained by this method gives information about the deviation from stoichiometry, and, to some extent, about the content of the defects. The deviation from stoichiometry is also responsible for the existence of an internal field E_i which is defined as $E_i = (E_{cf}\text{-}E_{cr})/2$ where E_{cf} and E_{cr} are the coercive field for polarization reversal from original state to reversed state and for that of reversed state to original state, respectively. It is found that the coercive field of LC-KTP for forward poling E_{cf} is lower than that of HC-KTP. This difference in E_{cf} can be attributed to a difference in K-stoichiometry between the two samples, were the HC-KTP has a lower K^+ content. For KTP, it can be assumed that the internal field E_i is formed by non-stoichiometric point

defects, namely vacancies of alkali ions and oxygen, as well as impurities, including OH$^-$ groups[8]. The sign of the internal field depends on the nature of the point defects and on how mobile they are.

Our own observations show that KTP samples with periodic electrodes are likely to switch at lower electric field if they have been previously poled back and forth. Figures 6.4 show variations of the coercive field in forward and reverse directions for (a) sample LC-KTP, and (b) sample HC-KTP. For LC-KTP, the coercive field of forward E_{cf} is slightly larger than that of reverse E_{cr} for the first poling cycle. For LC-KTP, the internal field vanishes and both coercive fields, E_{cf} and E_{cr}, reach a stable value. On the other hand, for HC-KTP, the internal field remains fairly constant, and the coercive fields just decrease slightly.
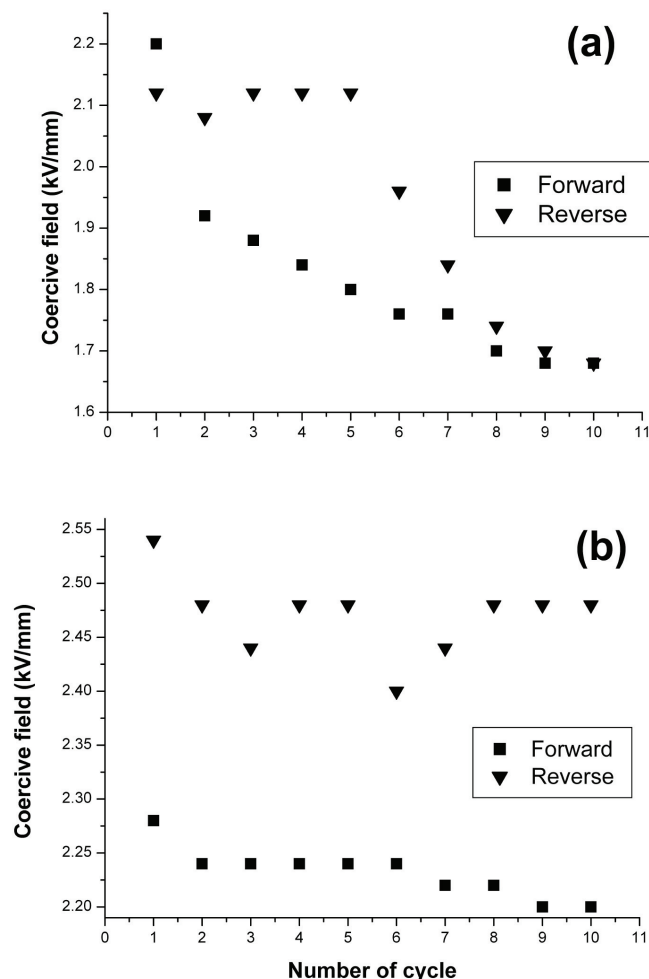
Fig. 6.4 Variation of the coercive field value in forward and reverse poling with the number of polarization cycles for (a) LC-KTP, and (b) HC-KTP.

During electric field poling, the vacancies and K^+ may redistribute, and, at the same time, due to the high mobility of the alkali ions, this can lead to a K^+ concentration gradient. Also, the external field may inject mobile ions from the liquid solution as well as dilute the crystal on K^+. The space charges created can be trapped in the crystal and modify the internal field and the steady state of K^+-distribution inside the crystal. These modifications can be readjusted with subsequent poling. Probably a lower conductivity which is due to a lower defect concentration allows for easier redistribution of K^+ ions and vacancies thus reducing the internal field. In HC samples, on the other hand, the screening is strong enough to prevent major defect redistribution by the external field.

6.2.4. Switching time

The polarization switching time gives information about how fast the domain inversion is, and hence it can be a significant factor for optimizing the fabrication of QPM devices using electric field poling. The switching time is field and pulse-shape dependent. In order to study the switching time, we used the method developed by Merz [9] where a constant field of certain magnitude is "turned on" and the duration of the switching current is measured. We distinguish a low-filed regime and a high-field regime, corresponding to the applied fields below and above the coercive field, respectively.

The switching time is commonly defined as the time necessary for the switching current to drop to 5% of its maximum value [10], but since the switching peak also contains ionic current and it is difficult to discriminate when the contribution of the switching current ends, we choose to define the switching time as the time from the beginning of the pulse to the moment when the half width of the total peak is reached.

Fig. 6.5 compares the switching time of a LC-KTP sample that has previously been poled back and forth more than 10 times with the switching time obtained with different independent virgin LC-KTP samples.

The trends are the same in both graphs, although for virgin samples the switching time is longer due to initially higher coercive field. Also, the presence of internal field is translated in a difference in switching time for forward and reverse polings, whereas for the sample that was previously cycled, the forward and reverse switching times are practically the same.

The inverse of switching time $1/t_s$ follows an exponential dependence on E in the low field regime, $1/t_s \propto \exp(\alpha \cdot E)$, and a linear dependence on E, $1/t_s \propto \beta \cdot E$, in the high field regime.
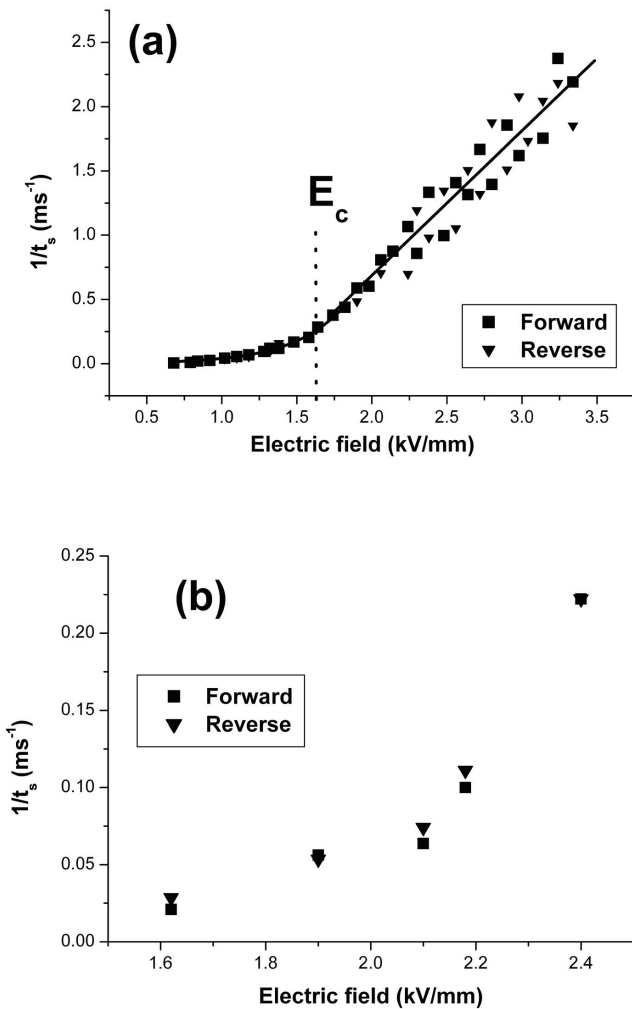
Fig. 6.5 The switching time for forward and reverse poling as function of the applied field. (a): for a 10 times cycled LC-KTP, (b): for independent virgin LC-KTP samples.

6.3. Selective domain-etching of KTP

In order to study the domain morphology in the different poling steps (section 3.6), electric field pulses of different magnitudes and lengths shorter than the switching time were applied to several virgin LC-KTP samples. Then those samples were subsequently etched to reveal the domain structure.

6.3. 1. Nucleation

Figures 6.6 (a) and (b) show typical nucleation morphologies which are taken on c-faces after application of a 10 ms long square pulse of 2.0 kV/mm (low field regime) and a 5 ms long pulse at 2.2 kV/mm (high field regime), respectively. In Fig. 6.6(a) (low

field regime), the domains are typically elongated in shape with the long axis parallel to the b-axis direction and their dimensions range between 0.4 μm to 5.0 μm. In the high-field regime (see Fig. 6.6(b)), a very dense laminar domain grating on the c^--side was formed. It is worth noting that no nucleation sites could be seen on the c^+-face in either case. Hence, the c^--face seems to be more favorable for domain nucleation. The laminar domains, parallel to the b-axis, appear aligned to the crystal growth striae in Fig. 6.6(b). The growth striae may contain higher density of defects or regions under stress, thus making nucleation more likely. These laminar domains should be formed by coalescence in the b-axis direction of nearby nucleation sites. Since the domain nucleus can only be seen on the c^--face, we tentatively conclude that the nucleus of a KTP domain is characterized by a laminar cone, with its tip pointing to the c^+ crystal surface. As this tip rapidly propagates to towards the opposite crystal face, the size of its base increases at slower rate.
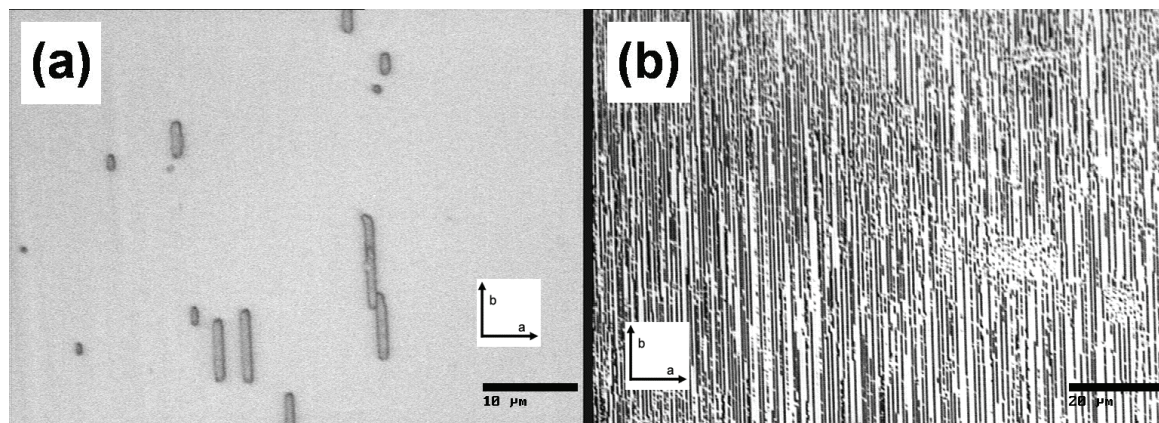
Fig. 6.6. Typical nucleation morphologies. (a) The c⁻-face after applying 2.0 kV/mm (low field regime) with 10 ms long duration pulse and etching. (b) The c⁻-face after applying 2.2 kV/mm (high field regime) with 5 ms long duration pulse and etching. The laminar domain, parallel to the b-axis, seems to be aligned to some kind of growth striae.

6.3.2. Forward propagation

The morphology of freely formed, isolated ferroelectric domains in KTP is laminar, and they remain elongated in the b-direction and quite constricted in the a-axis. Fig 6.7 shows the same domain structure after a 15 ms pulse of 1,85 kV/mm on (a) c^+-face and (b) c^--face. For clarification, an asterisk marks the same domain in both images. The domains have propagated along the whole crystal thickness. They still appear aligned along the b-axis. Note that not all the domains have the same sizes on both c-faces. They differ in width and length. This indicates the existence of charged domain walls, that can be stabilizes by the redistributing the highly mobile K-ions and defects. It is probably this easy redistribution of ions and vacancies that permits the almost instantly stabilization of the domain structure after removing the electric field.
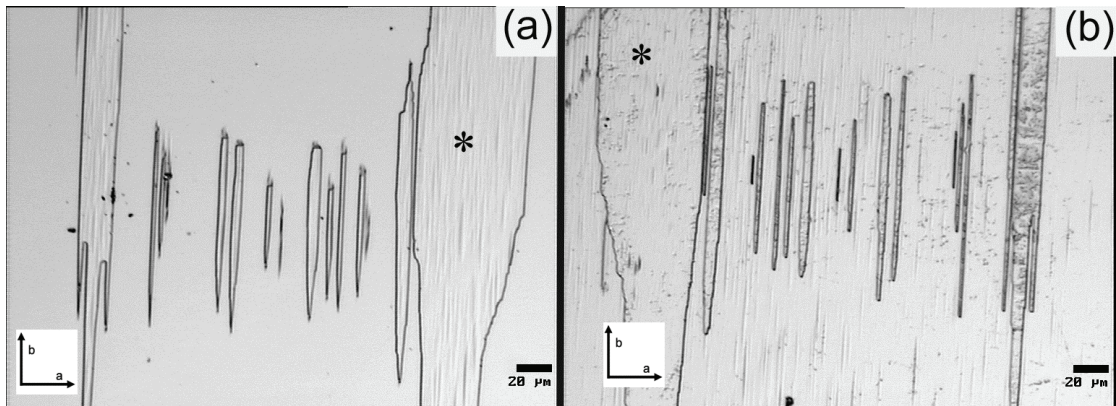
Fig. 6.7 The same domain structure after a 15 ms pulse of 1.85 kV/mm on (a) c⁺-face and (b) c⁻-face. For clarification, an asterisk marks the same domain in both images. The domains have propagated along the whole crystal thickness. Note that not all the domains have the same sizes on both c-faces. They differ in width and length.

6.3.3. Lateral domain growth

Fig 6.8 (a) shows sideways growth (in *a-b* plane) of the domains in KTP. The sample was first subjected to an electrical field of 2.3kV/mm during 1.5 ms, and then etched. Domains A_1 and A_2 were then observed. Afterwards, a second identical electrical pulse was applied, and the sample was etched again. The domains A_1 and A_2 had grown preferentially in the *b*-direction and expanded to B_1 and B_2, respectively. It can clearly be seen that the domain growth has been considerably faster in *b*-direction than along the *a*-axis. This can be explained by the anisotropy of the KTP crystal lattice that makes domain-walls parallel to the (100) plane most favorable, since these planes do not cut through the helical chains. It is also worth noting that all the domains in the image grew with different velocities.
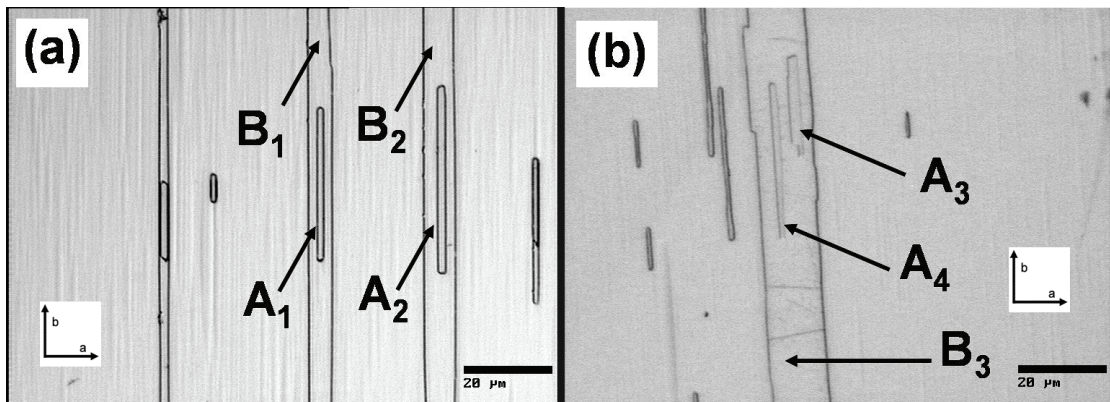
Fig. 6.8(a) Typical morphologies of sideways growth. The domains A_1 and A_2 were etched after applying a first electrical field pulse of 2.3 kV/mm during 1.5 ms. The domains B_1 and B_2 appeared after a second identical electrical pulse. (b) Typical morphologies of domain merging. The domains A_3 and A_4 were etched after application of a first electrical field pulse of 2.0 kV/mm and 10 ms duration. B_3 was obtained after a second electrical pulse of 2.0 kV/mm and 5 ms duration.

6.3. 4. Domain merging

Fig 6.8(b) shows an example of domain merging. This sample was subjected to a field of 2.0 kV/mm for 10 ms, and then etched. Domain A_3 and A_4 were then formed. An additional pulse of 2.0 kV and 5ms was then applied, and the sample was etched again. The domains A_3 and A_4 had merged after the second pulse and had become domain B_3. The domains rapidly merge together forming a larger domain when the domain walls of two adjacent domains touched.

6.3. 5. Estimation of the domain velocities

The domain wall velocities as a function of field strength were estimated using the Miller and Savage method.[11] In this method, an electrical pulse of a given length and magnitude is applied to a sample, which is subsequently etched; and the velocity is defined as the average length of the formed domains divided by the length of the pulse.
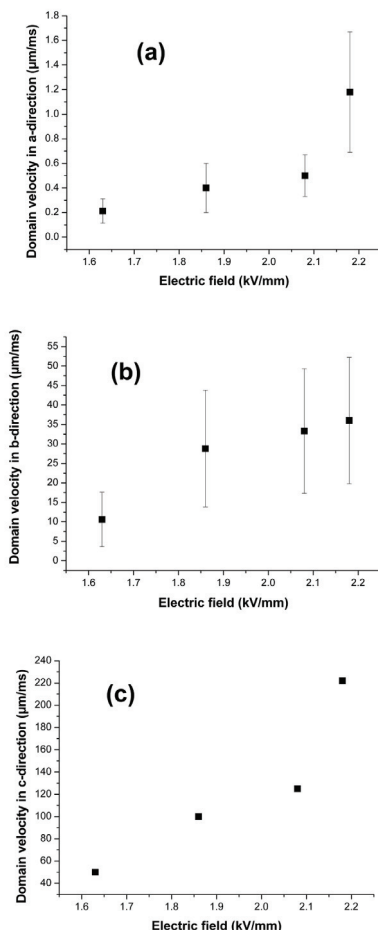
Fig. 6.9 The domain wall velocity in (a) a-direction, (b) b-direction, and (c) c-direction.

Figure 6.9 shows the measured domain wall velocities along each crystallographic axis. For the three directions, and in the range of fields studied, the domain velocity increased with the applied field. The velocity along the *b*-axis is ~30 times larger than in the *a*-direction. The velocity along the polar axis is, at least, two orders of magnitude larger than in the *a-b* plane. Note that the velocity in the *c*-direction is underestimated since it was calculated dividing the sample thickness by the length of the pulse.

6.4. Domain growth dynamics

The holographic method described in section 5.4 was used for *in-situ* dynamic polarization-switching studies. Three different electric field pulse shapes were used to study the domain kinetics: a square pulse 100 ms long (pulse A); a train of square 20 ms-long pulses with 50% duty-cycle (pulse B) and; a triangular 100 ms-long pulse (pulse C). For all of the measurements, we will refer to the effective time duration during which the sample is subjected to the external field.

Fig 6.10 shows sequences of selected frames of the reconstructed 2D phase shift distribution for (a) first forward poling for pulse-type A, and (b) first forward poling of pulse-type B. The spontaneous polarization axis is normal to the image plane. For pulses A and B there is an "incubation time" of 20-40 ms. The "incubation time" is the delay between the start of the voltage pulse and the observation of significant growth of domains. The existence of incubation time has been reported in LiNbO₃[12] and MgO:LiNbO₃[13]. It is probably associated with the existence of capacitive surface charge layers which neutralize a spontaneous polarization-related electric field in virgin KTP crystals. This surface charge layer is largely modified or eliminated during first domain reversal cycle, thus the "incubation time" is expected to be reduced or eliminated altogether in subsequent domain reversal cycles. The domain nucleation starts at the electrode edges, where the electric field is slightly larger due to fringing fields. Since KTP wafers present a parabolic variation of ionic conductivity in the *b*-direction, it is not surprising that nucleation starts always on the lower conductive edge of the sample.

For pulse-type A, the domains in frame 205 ms keep a constant speed (15 μm/ms in *b*-direction and 2μm/ms in *a*-direction) for ~20-30 ms; then is suddenly reduced one order of magnitude until the pulse is finished. The initial speed is recovered when a new pulse is applied. This is happening for the next pulses, until another domain overcomes them. This kind of "jerky" movement was also observed in LiNbO₃.[14] It is likely that lattice defects or impurities near the domains form space-charge regions that pin the propagating domain wall. Also, there is interaction of internal stress with crystal defects. It was shown that as-poled unannealed periodically poled KTP contained more stress than virgin crystals.[15] When the field is turned off and on, this stress at least partially relaxes leading also to space charge redistribution leading to unpinning the wall. Also in good agreement with experimental observation, the domain wall pinning should happen

on the time-scale of the dielectric relaxation time-constant, which was between 20 ms and 30 ms in our KTP wafers.
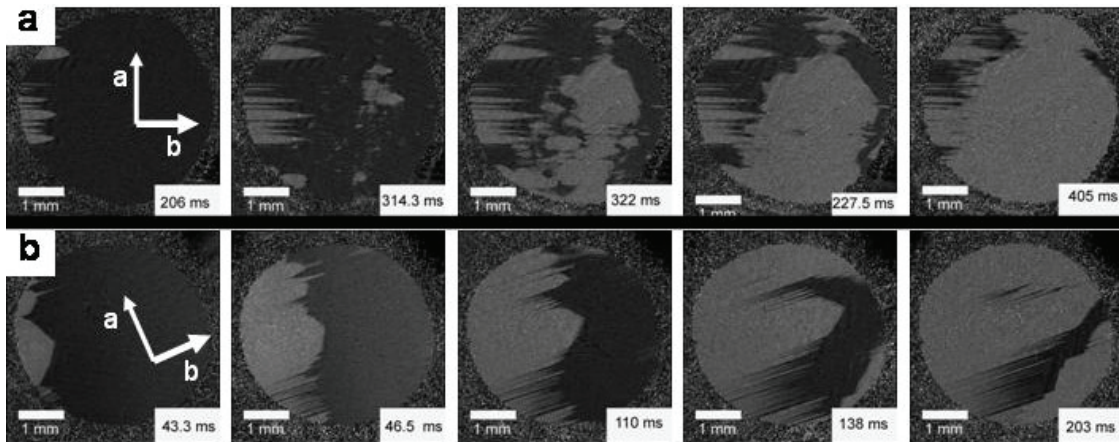

Fig. 6.10 Sequences of selected frames of the reconstructed two dimensional map of the phase shift distribution for (a) first forward poling for pulse-type A, and (b) first forward poling of pulse-type B. The crystallographic axis and the scale have been added to the images.

In the case of poling with pulses B, the domains are less elongated along the *b*-axis and they merge together quicker to form a single wall. It also seems that this train of pulses, switching the voltage on and off on a time scale shorter than the dielectric relaxation time, increases the density of nucleation sites. This observation might be attributed to time-dependent electric field redistribution in the bulk of the sample in the presence of a capacitive surface-charge layer. During the initial part of the voltage pulse the electric field in the bulk will be maximum and then relax with the dielectric relaxation time to a stationary value. If this stationary field is smaller than the coercive field then the nucleation of new ferroelectric domains will not occur. This makes the domains wider and more uniform. In the case of pulse-type A, several new domains appear in the middle of the sample from ~310 ms, which merge together quickly and dominate the switching process. Note that for pulse-type B, the domains keep a more steady speed and the "jerky" domain wall motion was not clearly observed, indicating that domain wall pinning is largely prevented by poling with pulses shorter than the dielectric relaxation time. Table 6.1 compares the incubation times and total poling time for subsequent poling cycles for A and B poling pulses. It is worth noting that the first reverse poling and the second forward and reverse present time scales that are one order of magnitude smaller than first forward poling. Note also that there is a small difference between the second forward and reverse poling cycles. This difference reflects the existence of an internal field, as discussed in section 6.2.3.

	A F1	A R1	A F2	A R2	B F1	B R1	B F2	B R2
Incubation time (ms)	25	3	7	3	34	5	6	5
Total poling time (ms)	350	11	26	10	215	10	15	10

Table 6.1. Comparison of the incubation times and total poling time for subsequent polings for A and B. F1,R1, F2, R2 refer to first forward poling, first reverse poling, second forward poling, and second reverse poling, respectively.

Fig 6.11 shows sequences of (a) first reverse poling for pulse-type A, and (b) first reverse poling for B. Note that in both cases nucleation starts from the same edge as the first forward poling, but the domains merge together in 1-2 ms to form a new domain front that moves quickly to the other side. This rather high speed can be explained by taking into account that the sideways motion occurs by preferential nucleation of new domains at the existing walls[17]. In KTP, these walls present a zigzag structure increasing their overall length. It was shown for LiTaO₃ that the activation energy for nucleation at the ledge of a serrate wall is lower than that for nucleation at flat walls. [18] Note that no domain wall pinning was observed in any of these polings.
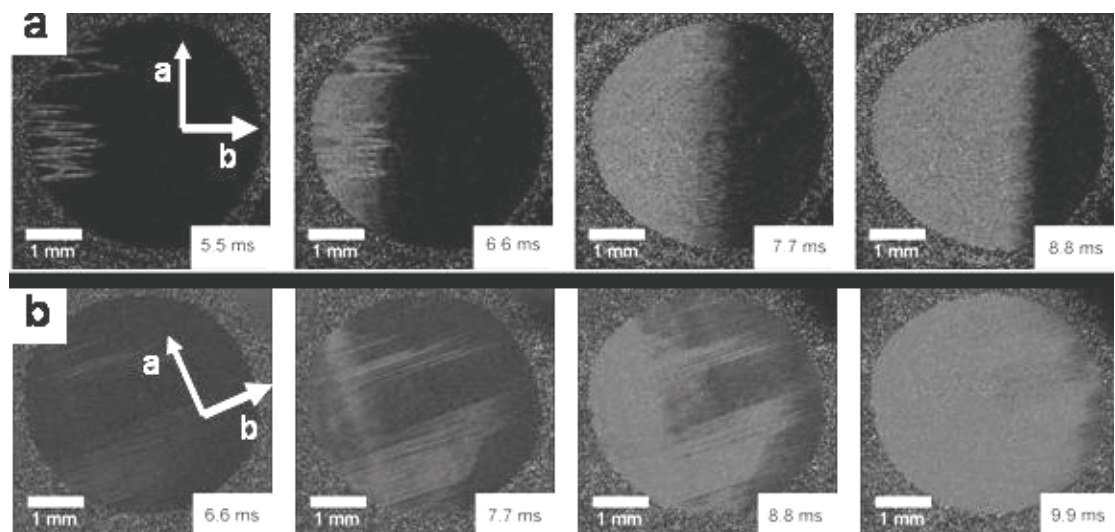
Fig. 6.11. Sequences of selected frames of the reconstructed two dimensional map of the phase shift distribution for (a) first reverse poling for pulse-type A, and (b) first reverse poling of pulse-type B. The crystallographic axis and the scale have been added to the images.

Fig. 6.12 shows selected frames of (a) first forward poling (b) first reverse poling for pulse type C. The triangular pulse has a rate of 68.8 V/ms up to 3.4 kV/mm. No incubation time is needed for triangular pulses. Nucleation starts at very low fields (1.3-1.4 kV/mm), and it only takes 8 ms to complete the switching. The nucleation is more uniform on the whole poling area, creating more fronts that quickly merge together. The difference between first forward and subsequent poling is minimal: the time scales are the same and they only differ on which edge the biggest domain emerges. Ramping the voltage decreases the potential drop in the capacitive surface and space-charge regions thus rendering higher and more uniform electric field distribution in the bulk of the crystal. In turn, this leads to more homogeneous nucleation and growth of ferroelectric domains. This observation is also consistent with the above-reported differences in the domain kinetics when poling with A- and B-type pulses.
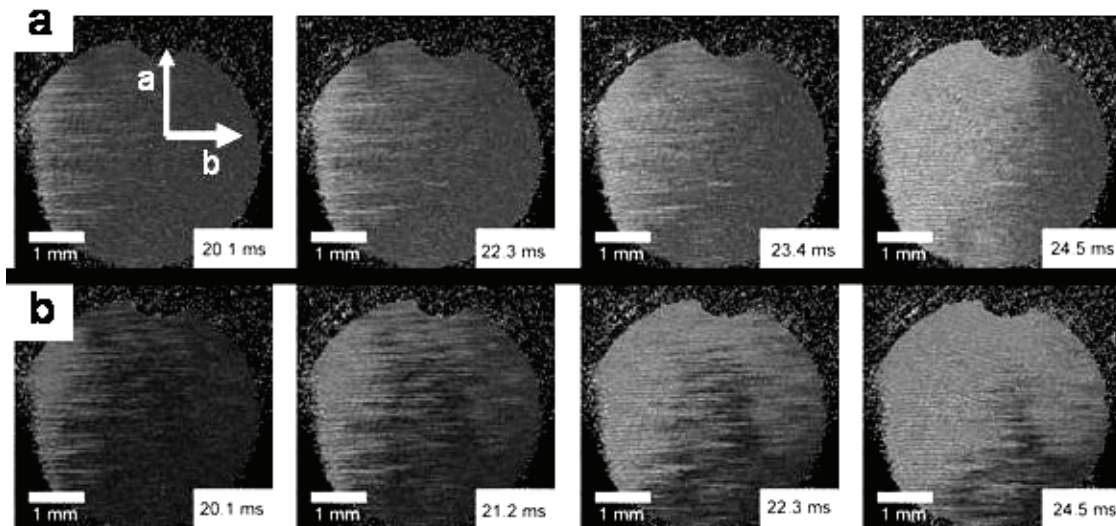
Fig 6.12. Selected frames of (a) first forward poling (b) first reverse poling for pulse type C. The crystallographic axis and the scale have been added to the images.

6.5. Comparison between electrical, etching and dynamic studies

All three types of studies give important information about the switching characteristics in bulk KTP that complement each other. The domain morphology obtained by etching and dynamic studies was the same, which means that essential no changes of what are induced by etching the sample. The speed of independent domains measured by the Miller and Savage[11] technique gives the same result as for the dynamic studies.

The switching time given by the electrical measurements when the samples were subjected to triangular electric field pulses was essentially the same as when the sample was observed by the holographic method (Keep in mind that in the later case the poling

area is larger than in the electrical studies). However, maybe an apparent contradiction appears with the observation of "incubation time". It is apparent because (a) the switching time presented in fig 6.5(a) corresponds to samples that have been previously poled back and forth more than 10 times, whereas the data matches well when one compares it with the second forward and reverse poling events in case of pulse type A. (b) Incubation time is probably accompanied by formation of nuclei/domains of dimensions smaller than 17 μm (pixel size in the holographic investigations). Thus these domains can only be observed by etching experiments.

References Chapter 6

[1] P. Urenski, M.Lesnykh, Y. Rosenwaks, G. Rosenman, and M. Molotskii, J. Appl. Phys. 90, 1950 (2001).

[2] P. Urenski, M. Molotskii, and G. Rosenman,. Appl. Phys.Lett. 79, 2964 (2001).

[3] G Rosenman, A Skliar, M Oron and M Katz, J. Phys. D: Appl. Phys. 30, 277 (1997).

[4] H. Karlsson, F. Laurell, Appl. Phys. Lett. 71, 3474 (1997).

[5] T.F. McGee, G.M. Blom and G. Kostecky, J. Crystal Growth 109, 361 (1991).

[6] D. Natali, M. Sampietro, J. Appl. Phys. 92, 5310 (2002).

[7] H. C. F. Martens, W. F. Pasveer, H. B. Brom, J. N. Huiberts, P. W. M. Blom, Phys. Rev. B 63, 125328-1 (2001).

[8] . P. A. Morris, A. Ferretti, J. D. Bierlein, and G. M. Loiacono, J. Crys. Growth 109, 367 (1991).

[9] W. J. Merz, J. Appl. Phys. 27, 938 (1956).

[10] E. Fatuzzo and W. J. Merz, Ferroelectricity, North-Holland Publishing, Amsterdam (1967).

[11] . R. Miller and A. Savage, Phys. Rev. 112, 755 (1958).

[12] L. –H. Peng, Y. –C. Fang, and Y. –C. Lin, Appl. Phys Lett. 74, 2070 (1999).

[13] K. Nakamura, J. Kurz, K. Parameswaran, M. M. Fejer, J. Appl. Phys. 91, 4528 (2002).

[14] V. Gopalan, Q. X. Jia and T. E. Mitchell, Appl. Phys. Lett. 75, 2482 (1999).

[15] S. Wang, V. Pasiskevicius, and F. Laurell, J. Appl. Phys. 96, 2023 (2004).

[16] S. Wang, V. Pasiskevicius, and F. Laurell, J. Appl. Phys. 96, 2023 (2004).

[17] R. C. Miller and G. Weinreich, Phys. Rev. 117, 1460 (1960).

[18] V. Gopalan, and T. E. Mitchell, J. Appl. Phys. 85, 2304 (1999).

Chapter 7

Periodic Poling of KTiOPO$_4$

7.1. Introduction

Several methods exist for manufacturing QPM devices involving chemistry,[1, 2] direct electron-beam writing[3], and modulation of the sign of the nonlinearity during ferroelectric crystal growth[4, 5]. However, the method of fabricating QPM structures by electric field poling using periodic electrodes on one of the polar faces of the crystal has been the breakthrough that has raised QPM ferroelectrics to their current importance. An efficient QPM grating should contain several thousands of few micrometers wide domains with a depth of 1 mm. The efficiency of these devices depends on the uniformity of the domain structure over the sample thickness and along the propagation direction of optical beam. The most harmful error on the conversion efficiency is an accumulating error in the periodicity[6], for instance, constant or randomly varying period error. This can be solved by properly choosing the patterning period form the Sellmeirs equation (section 4.4). The most common defects that arise from the device fabrication are missing domains (or merged domains) and duty-cycle errors. Although they not accumulate a phase error during propagation through the crystal, they do have an effect on the conversion efficiency. For example, missing or merged domains reduce the effective interaction length and the sinc^2-curve (equation 2.13) is distorted. A constant duty-cycle error reduces also the overall conversion efficiency, but does not distort the sinc^2-curve.

7.2. Periodic poling procedure

Fig. 7.1 shows a scheme of all the process steps involved in the fabrication of PPKTP. The process starts with mapping the conductivity of the as-purchased wafers, as explained in section 6.2.2. Due to the conductivity variations, the wafers are cut into smaller pieces, with more uniform conductivity that can then be treated separately. The

cuts are parallel to the crystallographic axis, and give a typical sample size of 10 mm in *a* and 5 mm in *b*. Finally, the end faces are polished to an optical finish for light propagation along the *a*-axis.

conductivity mapping

cutting & polishing
solvent cleaning

resist spinning (2 μm)
and baking (110°C, 90s)

resist exposure &
development

Al-deposition

Electric field poling
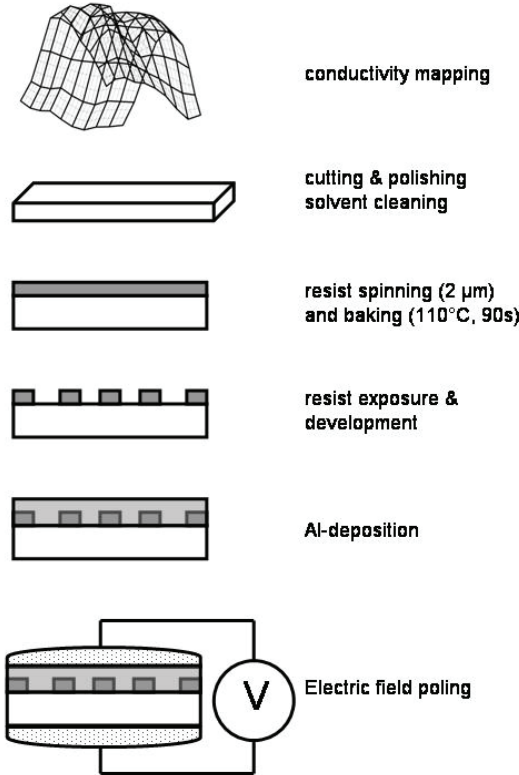
Fig. 7.1 Schematic of the steps involved in PPKTP fabrication process.

The samples are cleaned and 2 μm of positive resist S1818 is spun on one of the polar faces. The photoresist is soft-baked and then exposed through a mask using a g-line Hg lamp. Afterwards, an Al film (50-100 nm) is evaporated on top of the photoresist pattern. The sample is mounted in a plexiglas holder and connected to the circuit (Fig 6.1) by contact with a nearly saturated KCl solution. Afterwards, the sample is poled by applying electrical pulses.

It is of utmost importance to control and monitor all the steps involved in the periodic poling process in order to achieve highly efficient QPM devices.

7.3. Techniques for monitoring the poling process

During electric field poling, it is necessary to know when to stop applying pulses. If too few pulses are used, the domains are not completely reversed under the electrodes, while the application of too many pulses results in overpoling, i.e. poling of the areas between the electrodes. KTP is known for spatial inhomogeneities in the crystal structure (i.e., spatial deviation in stoichiometry) which can cause over-poling in some areas and under-

poling in others while still other areas can be well poled. In addition, crystals from different boules may have different dielectric properties, making a recipe for poling process difficult. To obtain as good poling as possible, it is necessary to monitor the poling process.

In the case of LiNbO$_3$, the charge transferred to the sample during poling provides a convenient means of controlling the poling process. Then, the point to "stop" the electric field is when the charge transferred is Q=2P$_s$A, being A the total area of the electrode. In KTP, however, ionic conductivity and variations in poling properties between samples prevent charge transfer from being used as the sole indication of successful periodic poling in such a way that the number of pulses must be determined for each sample.

Karlsson et al[7] developed a monitoring method base on the transverse electro-optic effect (Fig. 7.2). A He-Ne laser beam is linearly polarized 45° to the z and y axis of the crystal and is launch along the x-axis of the crystal during poling. When the crystal is subjected to an electric field, the y and z components of the laser polarization will be phase-shifted due to the electro-optic effect. This phase-shift can be detected by measuring the intensity change when the beam goes through a second polarizer orthogonal to the initial one. The phase-shift will be time-dependent only when the field is non constant (rise and fall of the pulse) or when the field is constant and polarization switching occurs (In this is the case, the sign of the electro-optic tensor elements will change).
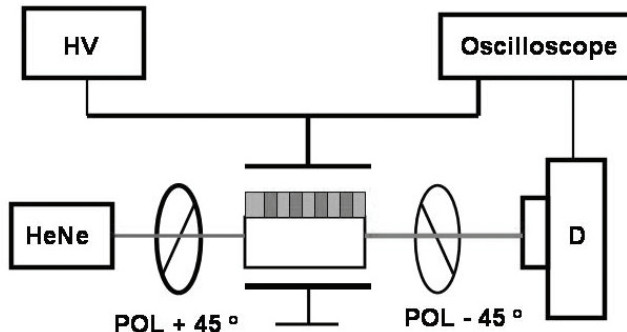
Fig 7.2 Set-up to monitor the poling with the electro-optic effect.

Another practical method to obtain good poling is to monitor in-situ the second harmonic generation signal. Wang *et al.*[8] proved the usefulness of this method for monitoring the poling of KTP isomorphs. The method uses a tunable continuous-wave (CW) Ti-Sapphire that is loosely focused in the sample. The pump can be scanned over the whole crystal aperture and information about the uniformity and quality of the poling can be obtained. Poling of KTP crystals with periods between 2-12μm, can be monitored with 1st order SHG directly, whereas high order SHG will be used for grating period larger than 12μm. This method is illustrated in Fig 7.3. In this work it has been used together with the electro-optic monitoring technique.
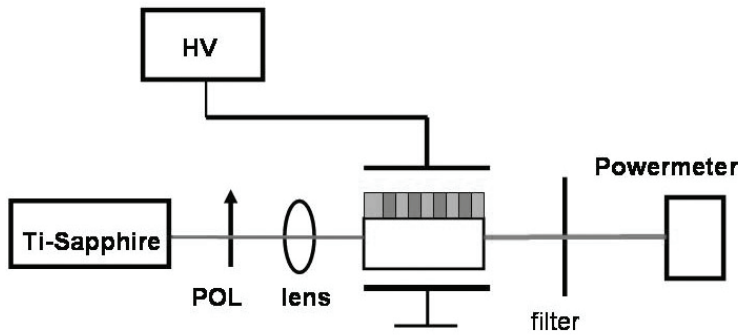
Fig. 7.3. The On-line SHG set-up

7.4. The electrode structure
7.4.1. Fringing fields

The electrode structure is important for controlling the electric field and supplying the injection charge for domain reversal. The insulator that is part of the patterned surface electrode helps shape the field and blocks the flow of charge to the region between the grating lines. There is significant fringing of the field around the electrode lines due to geometrical effects, which accumulate a large amount of charge at the edges of the electrodes, where the polar component of the electric field can be many times larger than the average field in the crystal. The depth of the fringing fields is strongly related to the electrode period. For congruent LiNbO$_3$, as a comparison, the depth of the fringing fields, *d*, in *c*-direction is proportional to the period[9]

$$d \approx \frac{\Lambda}{10} \qquad\qquad (7.1)$$

Fig 7.4 shows an example of the vector field plot for LiNbO$_3$ patterned with $\Lambda = 6$ μm. It can be assumed that the fringing fields in KTP behave in the same way as in LiNbO$_3$, at least before any domain formation takes place. Note that the electric field modulation evens out after a distance Λ below the crystal surface.
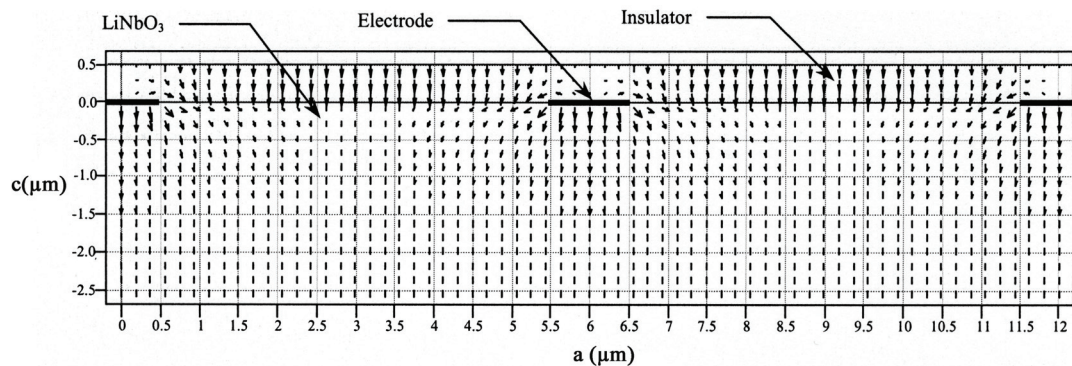
Fig. 7.4 Vector field plot showing the fringing field for a LiNbO₃ sample patterned with $\Lambda = 6\,\mu m$.[9]

Also, at the edges of the electrodes, the fringing electric field has a strong *a*-component, which might inject enough charge into the insulated region to initiate domain formation.[9,10] In general the domain spreading beyond the electrodes is determined by the conductivity component along the *a*-axis, as well as the electric field strength, the former parameter is to a large degree determined by the crystal quality and surface conditions, while the latter depends on the applied voltage and also on periodicity of the electrodes[9].

An example of the effect of the fringing fields and domain broadening can be seen in Fig 7.5. The sample was patterned with $\Lambda = 10.6\,\mu m$, with a duty cycle of 30% for the electrode and 70% for the insulator. It was poled with one square electrical pulse of 2.3 kV/mm (6 ms long). It can be seen that the domains formed at the edges of the electrodes; and many areas in the middle of the electrodes were not yet reversed. Moreover, the inverted regions resulted wider than the original 30% duty-cycle of the metal electrode, indicating that charge deposition has occurred underneath the insulated area.
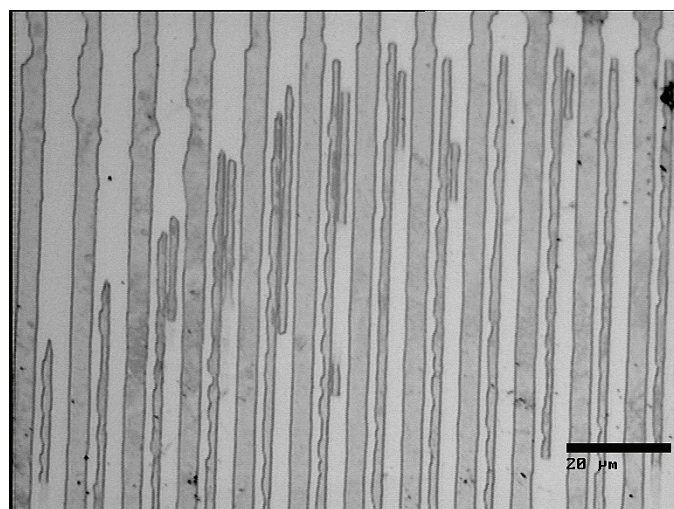
Fig. 7.5. The c-patterned face of a sample poled with one square electrical pulse of 2.3 kV/mm (6 ms long).
Domains formed at the edges of the electrodes; and many areas in the middle of the electrodes were not yet reversed.
The inverted regions resulted wider than the original 30% duty-cycle of the metal electrode.

7.4.2. Materials for the electrode structure

The photoresist used for patterning is considered insulating enough to prevent charge penetration and, if it is post baked, its dielectric strength can be enhanced. Photoresist is a convenient choice as the insulator since is the material used for patterning. However, other materials, for example oxide films, may offer better dielectric strength, resistance and durability.

For contacting the surface a liquid or a metal can be used. Homogeneous and good electrical contact is desired to have a uniform nucleation. In this work, the electrical contact was provided by a metal film on the patterned face and by liquid electrolyte on the non-pattern side. The main reason to use a metal film is nucleation enhancement. Experiments similar to those describe in section 6.3 (i.e applying pulses and etching), showed that the use of Al film enhances the domain nucleation on both polar faces. Fig 7.6 shows samples of similar conductivity poled with one square electrical pulse of 2.2 kV/mm (6 ms long) with a continuous Al film on (a) c^+ face, and (b) c^- face, and afterwards etched. It can be seen that the nucleation density for c^--face is larger than for c^+. Moreover, the sample with Al on c^+ presented some nucleation on its c^--face, whereas the sample with Al on c^- did not show any nucleation sites on c^+. Therefore, patterning on $c-$ can be more advantageous than on c^+, since the nucleation enhancement can limit the domain propagation to one single direction, at least in the first stages of the domain switching. In addition, the metal lines give much better defined edges than liquid electrode-covered photoresist.
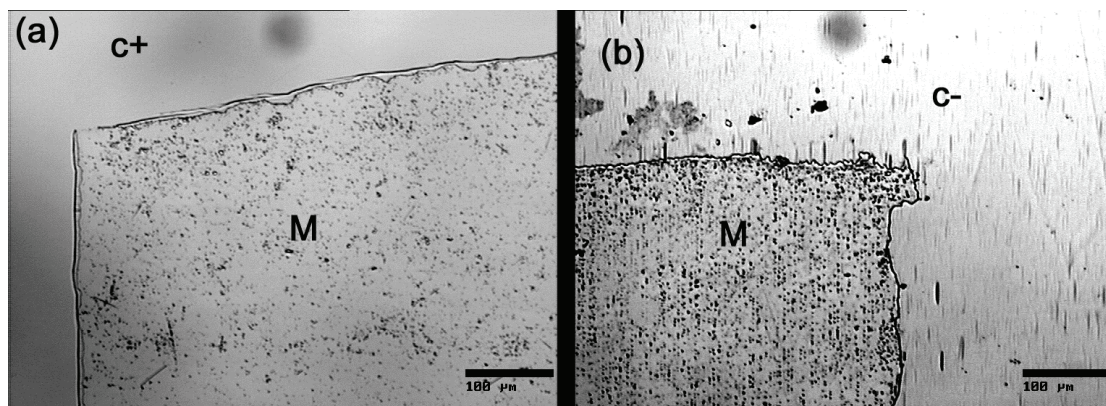
Fig 7.6 Nucleation sites in samples with a continuous Al film on (a) c^+ face, and (b) c^- face.

7.5 Electric field poling

Once the electrode structure is defined, the list of variables that one can play with is still large: poling temperature, pulse shape, pulse length, electric field magnitude number of pulses…etc. In this work, we have set all the parameters but two. We have chosen to work at room temperature because poling at low temperature increases the coercive field considerably and it has not been proven that it gives better results. The shape of the electrical pulses has been square with a rise time shorter than 100 μs and a fall time around 1 ms. The pulse duration was usually between 1-10 ms, but 6 ms has been the standard length during this work. This value, although it has not been optimized, has proven to give reasonably good results. There are several reasons to use pulses instead of a continuous field. First of all, as it has been shown in chapter 6, the poling in KTP is too quick (less than 1 s) to allow a manual stop of the voltage and, since the poling current is masked by the ionic current, no evident feedback loop can be implemented. Another reason is to prevent domain wall pinning by switching the voltage on and off. Thus, the variables that we have played with are the field strength and the number of pulses.

We believe that domain growth in KTP during periodic electric field poling follows a widely accepted process described for $LiNbO_3$.[11] Looking down upon the patterned c-face of the patterned crystal, domain nucleation begins at the two edges of each electrode where the field is strongest. The domain nuclei rapidly propagate vertically down toward the opposing crystal face, and, in a slower process, merge horizontally under each electrode. However, domain propagation along the polar axis and sideways spreading of the domain wall seem to be two competing processes due to the limited supply of external electrostatic energy. If the domain propagation along the polar axis is slowed down for instance due to presence of crystal defects, then we should expect larger domain broadening. Also we have observed that sidewise domain growth and merging occurs before the tips reach the opposite polar face. Correct domain growth seems to depend on the electric field strength and the number of pulses.

7.5.1. Poling in the low field regime

By poling in the low field regime we refer to poling with fields below or very close to the coercive field. The idea behind poling in low field regime is to obtain low domain speeds, so that the domain merging can be potentially controlled. Although this seems to work in some cases, it usually yields overpoling under the pattern and a shallow domain depth.

Fig 7.7 displays different positions on the b-face of a sample with a period of Λ=26.3 μm, poled by one pulse of 2.1 kV/mm followed by two pulses of 1.75 kV/mm. The top of the images (a), (c) and (e) of fig. 7.7 correspond to the edge of the c patterned side. The uppermost of all three images corresponds to edge with the c⁻ patterned side. The three figures below, (b), (d) and (e) show where the tips of fig (a), (c) and (e) begin to

end, respectively; and are taken at a depth in *c*-direction of 270 μm, 260 μm and 218 μm for (b), (d), and (e) respectively.
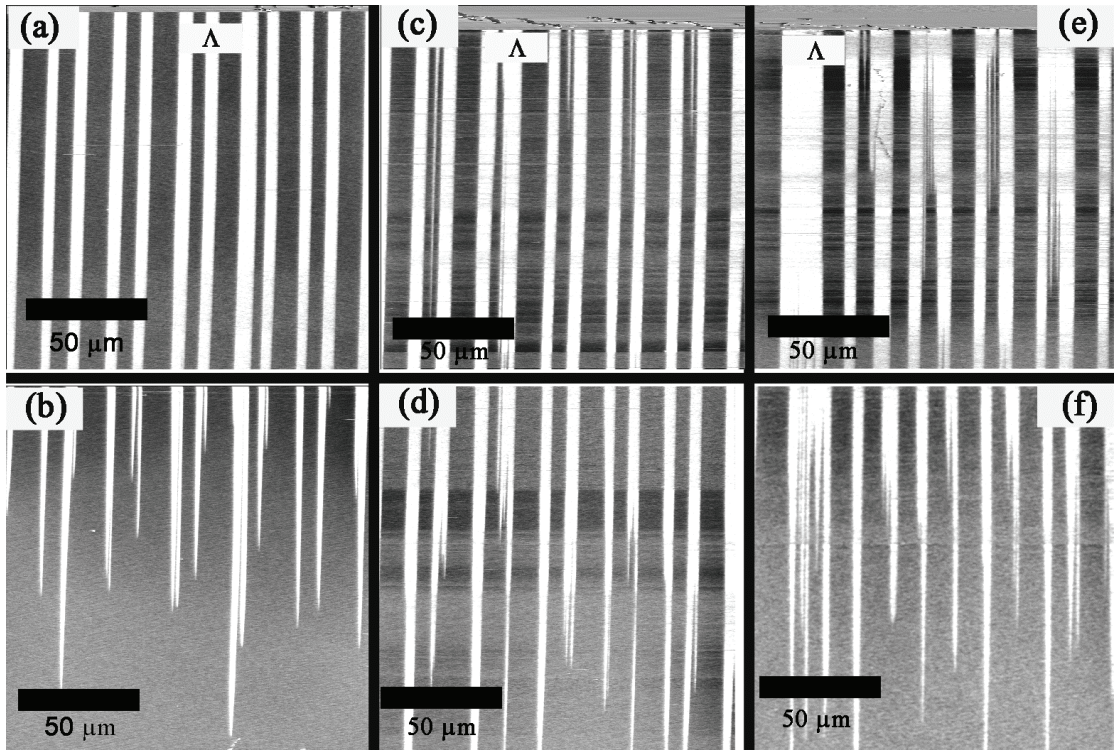

Fig 7.7 Different positions on the b-face of a sample with a period of Λ=26.3 μm. The top of the images (a), (c) and (e) correspond to the edge of the c⁻ patterned side. The uppermost of all three images corresponds to edge with the c⁻ patterned side. The three figures below, (b), (d) and (e) show where the tips of fig (a), (c) and (e) begin to end, respectively; and are taken at a depth in c-direction of 270 μm, 260 μm and 218 μm for (b), (d), and (e) respectively.

Fig 7.7(a) shows domain formation starting at the edges of the metal electrodes and fast propagation along the polar axis. Fig 7.7(c), representing another region of the same sample, shows several independent tips growing between the two electrode edges. This indicates that in this stage the domain switching is governed by nucleation of new domains. The tips growing from the middle of the electrode do not penetrate as deep as the ones growing from the edges, since the field is not as high. Fig 7.7(e) displays a third position in the same sample. Here the nucleated domains in the regions below electrodes are in the process of merging or have already merged. It is worth noting that the domain merging occurs much before the tips of the first edge-nucleated domains reach the c^+-face. The fact that the three regions present different domain evolution means that the domain inversion starts at different positions in the crystal and suggests sample inhomogeneity or, more specifically, deviation form stoichiometry.[PAPER III] After initial domain nucleation at the electrode edges, the domain rapidly propagates along the polar direction helped in part by the electric field enhancement at the tips of growing domains (see Fig 7.7(b) which shows the domain tips at the depth of 290 μm, where the domains of Fig 7.7(a) terminate). On the other hand, the domain wall speed along the *a*-crystal

axis in KTP, causing domain broadening and mergeing, is more than an order of magnitude lower. Domain propagation along the polar axis and sideways spreading of the domain wall seem to be two competing effects. Indeed, the average domain length along the c-axis for the position in Fig.7.7(a) was 290 μm, compared to 230 μm for the position of Fig.7.7(e). It is notable, that the domain broadening in Fig.7.7 has been the same for the three regions, i.e. duty cycle of poled region is 60%, while the original duty-cycle was 40%.

If a sample is subjected to too many pulses of low magnitude, lower than the coercive field, the domains merge together underneath the patterned face, but maintain a periodic structure after a certain depth. Fig 7.8 shows a sample of Λ= 10.6 μm poled with 6 pulses of 2.16 kV/mm. Fig. 7.8(a) is taken just below the periodic electrode. In this case, as the domains spread out under the electrodes, unscreened charges on the surface of the crystal lowers the average field seen by the domain under the insulated region, slowing its growth, and making the complete merging underneath the pattern face. Fig 7.8(b) shows the domain structure at a depth ~500 μm from the patterned side. Fig 7.8(c) shows the domain structure close to the unpatterned side.
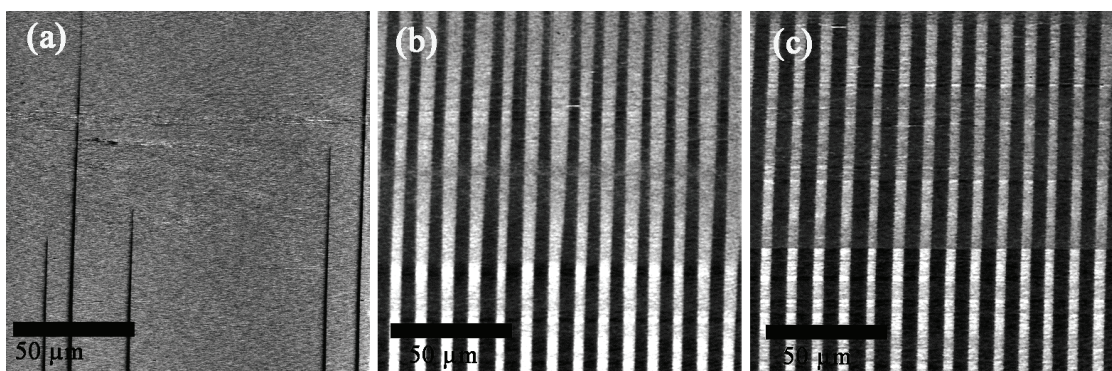
Fig 7.8. A sample of Λ= 10.6 μm poled with 6 pulses of 2.16 kV/mm. (a) is taken just below the periodic electrode; (b) shows the domain structure at a depth ~500 μm from the patterned side; and (c) shows the domain structure close to the unpatterned side.

7.5.2. Poling in the high field regime

Poling in the high field regime means poling with fields higher than the coercive field. Poling in the high field regime will be beneficial in the sense that the domains will propagate much faster to the opposite face. However, if the magnitude of the applied field is too high, the domains maintain a periodic structure close to the patterned face and the broadening and merging occurs in the bulk. Fig 7.9 shows the b-face of a sample of Λ= 26,3 μm poled with 2 pulses of 2.7 kV/mm.[*] The image is taken at the edge with the patterned side. In this case, initial nucleation and growth rate of the domains under the patterned electrodes is much higher than the characteristic Maxwell relaxation rate

---

[*] Keep in mind that light contrast corresponds to inverted regions.

for the surface charge injection along the *a*-axis, thus preventing domain spreading beyond the electrodes. Moreover, the negatively charged domain tips propagating from the electrode edges cause redistribution of the electric field thus effectively reducing the fringing field at the electrodes which slow down the lateral charge injection even further. At the same time the field at the non-patterned c^+-face is large enough to start nucleation, creating high field areas on this side. The couter-propagating domains interact and merge in the bulk of the crystal. Note, however, that the domains present ~50% duty-cycle close to the patterned face. Thus, poling in the high field regime can be beneficial for the limited amount of charge injection below the insulator.
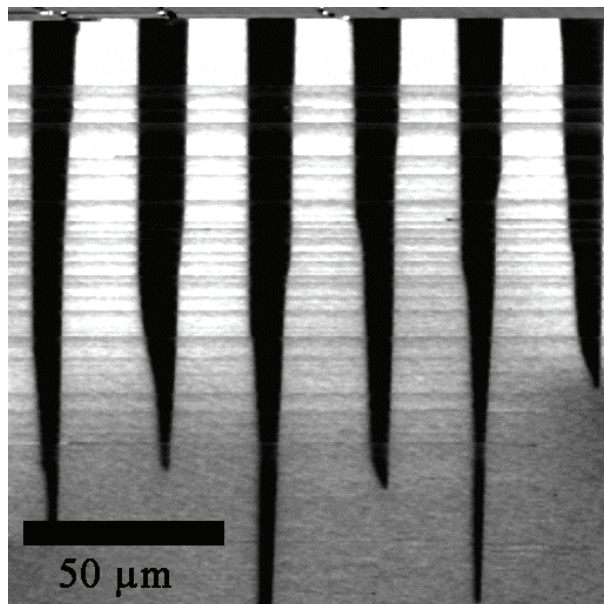
Fig. 7.9. The b-face of a sample of Λ= 26,3 μm poled with 2 pulses of 2.7 kV/mm. The image is taken at the edge with the patterned side

Nevertheless, my best results have been obtained by poling the samples with one or two single pulses in the high field regime. The pulse should give enough energy to pole the sample all the way through, but prevent excessive domain broadening and merging. The magnitude of the pulse needs to be adjusted for each particular sample, and its value can be guessed from conductive and the E_c measurements. An example of this can be seen in fig 7.10. However, also good samples have been obtained by poling in the low field regime or with combination of high and low field regimes pulses.
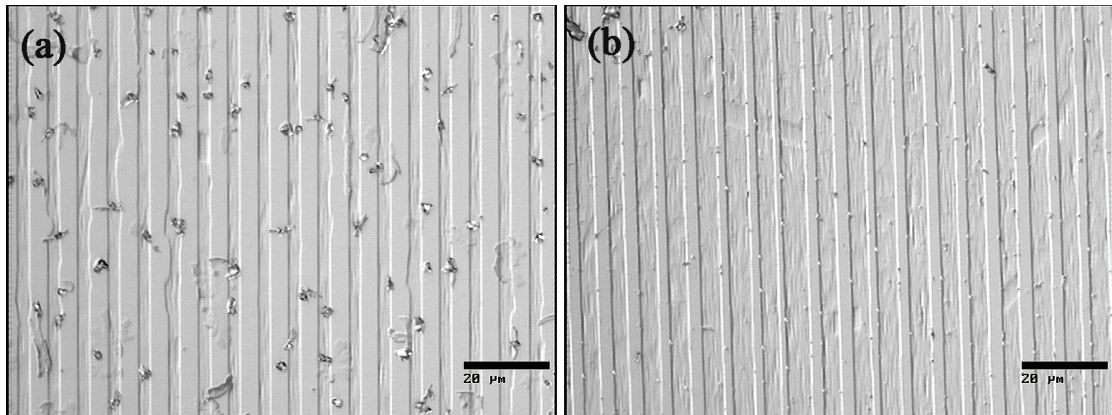
*Fig 7.10. Polar faces of a sample with a period of Λ= 10.6 μ, poled with one pulse of 2.65 kV/mm.
(a) patterned c⁻-face; (b) former c⁺-face.*

7.5.3. Combination of poling in the high and low field regimes

The idea behind this method is to give enough energy in the first pulse to propagate the tips from the edges of the electrodes deep enough and then, with pulses of lower magnitude, slowly merge them.

A sample with Λ= 10.6 μm poled with 1 pulse of 2.46 kV, followed by 6 pulses of 1.74 kV/mm presented an average domain width of ~6.5 μm, i.e., a duty-cycle of 65% (the electrode duty-cycle was 30%). The b-face of this sample is shown in Fig 7.11: (a) at the edge with the patterned side, (b) at 500 μm from the ċ-face, and (c) at the edge with the non-patterned face. In fact, the high applied field makes the *a*-axis component of the fringing field large and, hence, injecting charges in the insulated region. In this case, only a few domains tips reached the c⁺-face. Most of the tips underneath the electrodes have merged together at a depth of 500 μm.
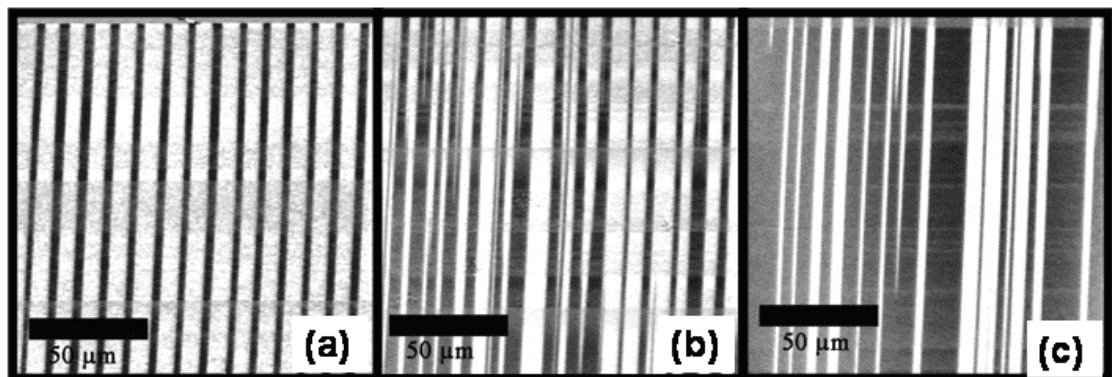
Fig.7.11. The b-face of a sample with Λ= 10.6 μm poled with 1 pulse of 2.46 kV, followed by 6 pulses of 1.74 kV/mm. (a)is taken at the edge with the patterned side; (b) at 500 μm from the c⁻-face, and (c) at the edge with the non-patterned face.

Fig. 7.12 shows the domain structure on the $\bar{c}$-face of the same sample of Fig. 7.11 with the topography of the metal pattern over imposed. The domains have larger width than the electrodes. There are several bulges along the domain wall. These bulges are growth steps, i.e. nucleation besides a preexisting domain wall. The steps have a typical size of 2×0.5 μm², being elongated along the b-axis. This indicates that the preferred growth direction is in the b-direction, in good agreement with previous observations.[Paper III, 12] The shape of these steps is not related to the metal electrodes, since we have also observed them in samples without periodic pattern poled with plain liquid electrodes. However, this bulges steps seem to appear almost exclusively on the $\bar{c}$-face (whether has been the patterned face or not). This supports the idea of preferential nucleation on the $\bar{c}$-face.
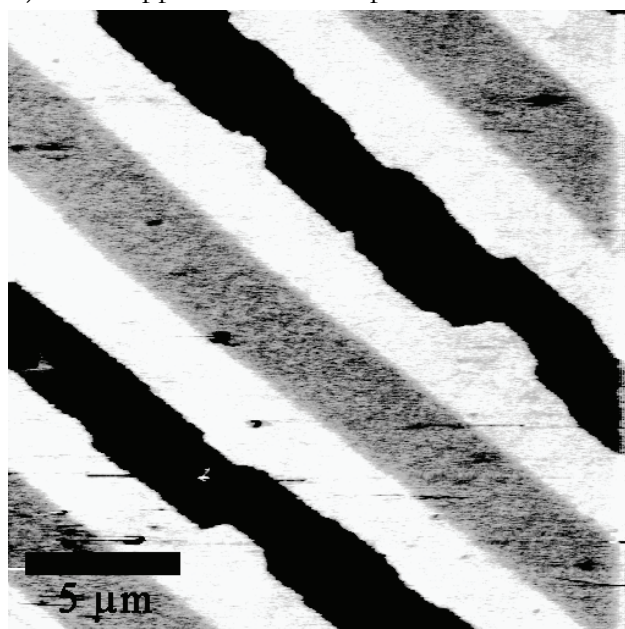
Fig. 7.12 The domain structure on the c̄-face of the same sample of Fig. 7.11 with the topography of the metal pattern (in grey) over imposed is shown. The white area, then, represents the broadening.

7.6. Inhomogeneities

There are mainly two kinds of inhomogeneities that influence the periodic poling: local (small scale) inhomogeneities and spatial (large scale) inhomogeneities.

Local inhomogeneities probably derivate from local concentration of defects, and result in areas with merged domains. An example can be seen in Fig 7.13(a). However, the more severe case derives from the parabolic variation in conductivity in the KTP wafers. These spatial inhomogeneities result in samples that are only partially well poled in the b-direction, as can be seen in Fig 7.13(b) A possible solution would be to cut the samples in smaller pieces, although that will difficult the patterning process due to photoresist thickness variations at the sides of the crystal.
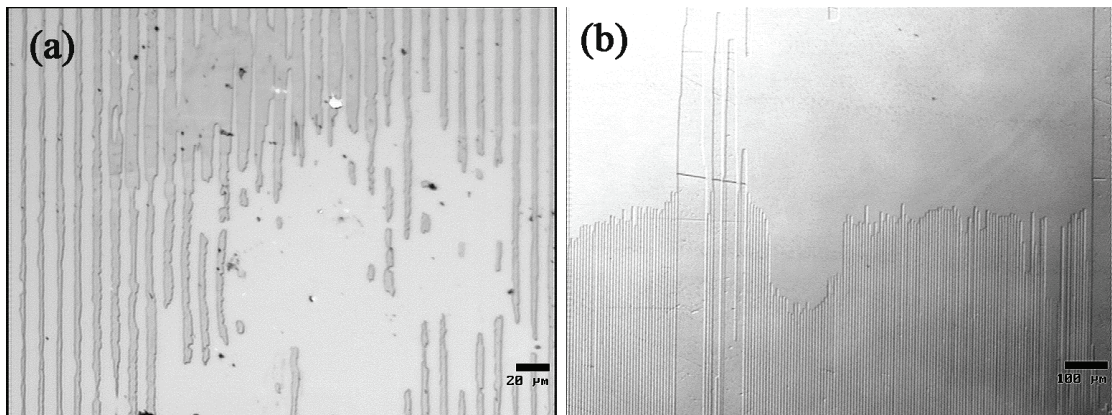
Fig 7.13 (a) local inhomogeneities showing several domains merged together; (b) spatial inhomogeneities resulting in well poled and merged areas in the b-direction.

References Chapter 7

[1] C. Baron, H. Cheng, M.C. Grupta, Appl. Phys. Lett. 68, 481 (1996).

[2] W. P. Risk, and S. D. Lau, Appl. Phy. Lett. 69, 3999 (1996).

[3] M.C. Grupta, W. P. Risk, A. C. G. Nutt, Appl. Phy. Lett. 63, 1167 (1993).

[4] J. Capmany, V. Bermúdez, E. Diéguez, Appl. Phys. Lett. 74, 1534 (1999).

[5] Y.H. Xue, N. B. Ming, J. S. Zho, D. Feng, Chin. Phys. 4, 554 (1984).

[6] M. M. Fejer, G. A. Magel, D. H. Jundt, and R. L. Byer, IEEE J. Quantum Electron. 28, 2631 (1992).

[7] H. Karlsson, F. Laurell, L.K. Cheng. Appl. Phys. Lett. 74, 1519 (1999).

[8] S. Wang, V. Pasiskevicius, and F. Laurell, "highly efficient periodically poled Rb-doped $KTiOPO_4$ using in-situ monitoring" submitted to J. Appl. Phys. (2005).

[9] G. Miller, Periodically poled Lithium Niobate: Modeling, fabrication and nonlinear-optical performance, PhD Thesis, Stanford University (1998).

[10] K. Nakamura, J. Kurz, K. Parameswaran, M. M. Fejer, J. Appl. Phys. 91, 4528 (2002).

[11] V. Shur, E. Rumyantsev, R. Batchko, G. Miller, M. Fejer, R. Byer, Ferroelectrics 221, 157 (1999).

[12] J. D. Bierlein and F. Ahmed, Appl. Phys. Lett. **51**, 1322 (1987).

Chapter 8

Sub-micrometer periodically poled KTiOPO$_4$

8.1. Introduction

When the period of a poled device approaches the value of the wavelength of the pump, new types of optical effects can be observed and new components can be made. This could for example be electrically controlled Bragg reflectors, beam steering devices and narrow band filters. When a continuous electric field is applied over such a structure the opposite domains will attain positive and negative refractive index change depending on their orientation and a multi-layer-index stack will be formed. The optical response function of such a layered refractive index structure is a narrow band filter with a bandwidth and reflectivity depending on the applied field and the length of the structure. Furthermore, if these addressable components are used in lasers they will allow several new functions. First, the wavelength of the laser can be made single frequency as a result of the narrow bandwidth response of the filter function, and secondly it can be switched between frequencies if several separate grating are produced in the same crystal. Then, as a third important option, the output coupling can be modulated to switch on and off the laser, or to choose a certain output power independent of the other laser parameters (like pumping). In beam steering applications such devices would allow a higher angular deflection to be attained than in conventional components. Other types of nonlinear devices have also been proposed, in QPM SHG, for example, if sub-micron domains can be created, $K=2\,\pi\,m\,/\Lambda$ becomes then the dominating term and the defining wavevector and allows implementation of QPM interactions involving counter- and back-propagating beams, e.g., counterpropagating optical parametric oscillators[1], and all-optical switching components which take advantage of increased efficiency in counterpropagating cascaded second-order interaction[2, 3, 4].

Structuring of the nonlinear media on sub-micrometer and nanometer scale is the key technology required for implementation of these devices.

Dense domain gratings have recently been fabricated in bulk LiTaO$_3$ and KTP. For LiTaO$_3$, grating periods of 1.75 μm and 2.65 μm have been generated[5, 6] in 150 μm- and 200 μm-thick samples, respectively. For KTP, the shortest period reported was 2.95 μm[7] for 1 mm thick samples. The latter corresponds to a domain–thickness aspect ratio smaller than 1.5:1000. Recently, Shur *et al.*[8] reported fabrication of nanoscale domain patterning in LiNbO$_3$ based on controlled back-switched poling. The depth of these structures was about 50–100 μm. Risk *et al.*[9] have reported fabrication of segmented ion-exchanged waveguides in KTP, with distributed Bragg reflectors showing a period of 0.7 μm. The Bragg grating section consisted of 0.4 μm-long domain inverted segments separated by a 0.3 μm gap. These waveguides have also been used for backward second-harmonic generation.[10] The depth of the domain inverted segments was not measured in this case, but the technique used for ion-exchange induced domain reversal is known to give a shallow domain inversion of a few μm. A 250 μm thick LiNbO$_3$ sample with a Λ=3.3 μm has been used to demonstrate 16th to 19th order QPM BSHG with ns-pulses.[11] Rosenman et al.[12] inverted 0.49-0.3 μm domains in 200 μm thick LiNbO$_3$ and RbTiOAsO$_4$ plates by high voltage AFM. However, this method is slow, and it is not useful for practical devices.

In this chapter, we present fabrication of sub-μm PPKTP. Two techniques for lithographic patterning will be described, as well as a chemical pattering technique. At the end, the optical performance of these structures will be shown.

8.2. Patterning techniques

The resolution achievable with a conventional contact photolithographic mask aligner based on the Hg g-line exposure is approximately 1 μm. Therefore, two techniques that allow patterning of nanoscale features have been explored: e-beam lithography and deep UV-laser lithography.

8.2.1. E-beam lithography

The electron beam (e-beam) lithographic system used in this work is a combination of a scanning electron microscope (SEM) manufactured by LEO microscopy Ltd. using a Gemini column and a high precision laser interferometric stage combined with special digital to analog converters for the e-beam deflection during lithography, both made by Raith Gmbh.

The first complication with e-beam lithography that arises is substrate charging. Although KTP is an ionic conductor, it is not conductive enough for e-beam radiation and the electrons from the electron-beam build up at the surface and deflect the beam.

The first attempt to solve the problem was to deposit a thin (10-20 nm) gold layer on top of the e-beam resist. However, this created tensions in the metal-resist interface, which resulted also in a distorted pattern.

Therefore, we chose to have the metal film between the KTP surface and the resist layer, and to transfer the pattern from the resist into the metal by dry-etching. The pattern, sketched in Fig. 8.1, consisted of 3 arrays, separated by 200µm, of 12 sets of structures of 800 nm periodicity, and 50% duty cycle. Each set was 400µm long and 80µm wide. The gaps between the different sets were 20 µm. Since the pattern was large and required long exposures times, the separation between the different gratings was chosen to avoid stitching errors of the e-beam writing field, which could yield a mismatch between the electrodes and the insulated regions.
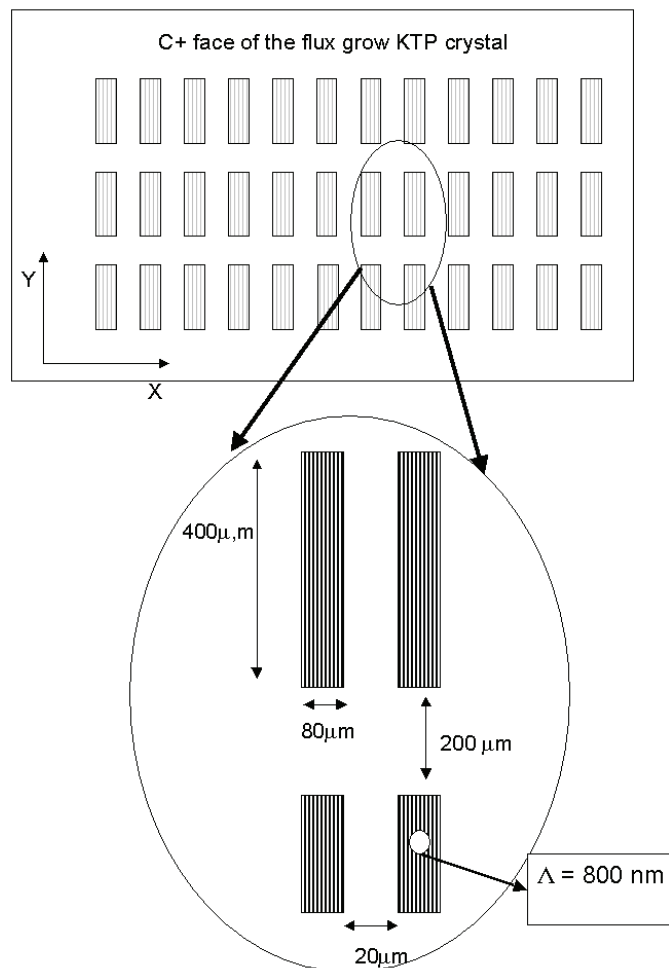
Fig. 8.1. Sketch of the pattern that was transferred into the Ti layer by e-beam lithography.

Once the pattern was transferred into the Ti layer, the e-beam resist was removed and an insulating layer of 2 µm photoresist was deposited on top of the pattern, except for an opening of 3 mm × 1mm at one edge of the metallic region, which was left to be an electrical contact. The large gaps between the sets of patterns (i.e., 20 µm and 200 µm gaps) ensured that all the metal lines had electrical contact. The lithographic steps are depicted in Fig 8.2. Since the regions that had been e-beam exposed corresponded to the

insulated regions, the pattern was deposited on the c^+ face in order to avoid any domain switching due to electron bombardment.[13]
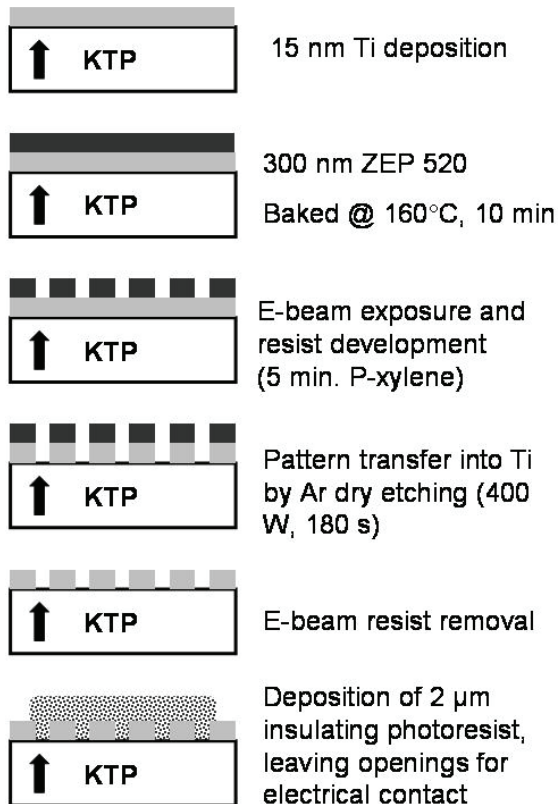
Fig. 8.2 Schematic of the steps involved in e-beam lithography.

The major disadvantage of e-beam lithography is the slow writing speed. For example, 3 hours were needed to expose the pattern of fig 8.1. Also, longer exposure times may result in a lost of control of the e-beam spot size (like, focus, astigmatism… etc), resulting in a distorted pattern.

8.2.2. Deep UV lithography

The long exposure times required by e-beam lithography limited the amount of area that could be patterned. Moreover, the large number of processing steps decreased the yield of a successful pattern. An alternative for dense gratings is deep UV-laser lithography, which allows large areas to be exposed and the process is as simple and as quick as conventional photolithography.

A deep UV-laser lithography system was build in-house. The frequency doubled argon-ion laser (244 nm) beam was launched through a microscope lens, followed by a pin-hole and a collimating lens. The collimated beam was then split by a phase mask. The two beams were recombined to form an interferometric grating. Fig 8.4 shows the interferometric set-up. The total grating area that could be exposed was 10×20 mm^2.
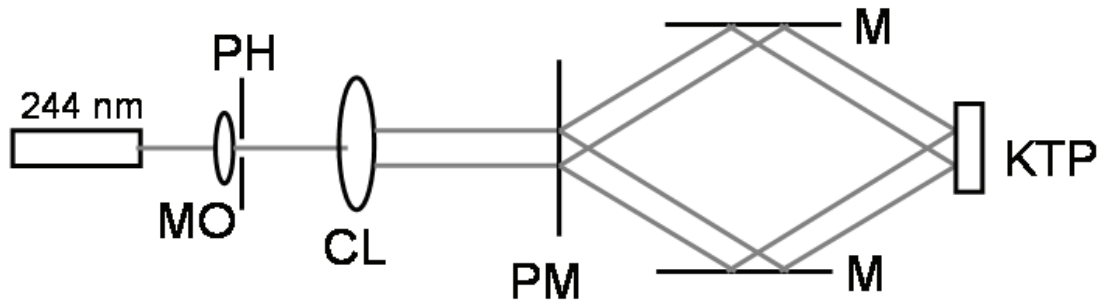
Fig. 8.4. Deep UV laser lithography setup. MO, microscope objective; PH, pin hole, CL, collimating lens; PM, phase mask; M, mirror.
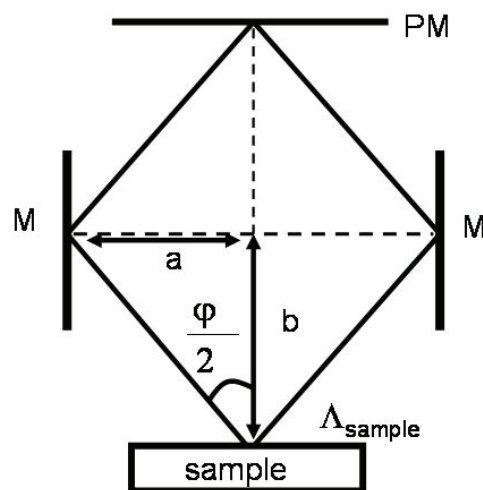
Fig. 8.5. Geometry in the deep UV laser lithography setup.PM, phase mask; M, mirror.

Fig 8.5 shows the geometry of the lithography set-up. The period of the grating could be changed by changing the distance of the sample to the mirrors plane and subsequently adjusting the mirrors angles in the following way: since $\Lambda_{sample} = \dfrac{\lambda_{laser}}{2\,sin(\frac{\varphi}{2})}$ and

$tan(\dfrac{\varphi}{2}) = \dfrac{a}{b}$, then $\Lambda_{sample} = \dfrac{\lambda_{laser}}{2\,sin(arctan\frac{a}{b})}$.

The main drawbacks in deep UV-laser lithography is that the photoresist used was not electrically insulating enough for electric field poling. Thus the deep-UV photoresist was lift-off and a new layer of 2 μm conventional photoresist was deposited on top of the metallic pattern, leaving some openings for electrical contact. Fig. 8.6 depicts the processing steps involved in deep UV-laser lithography.
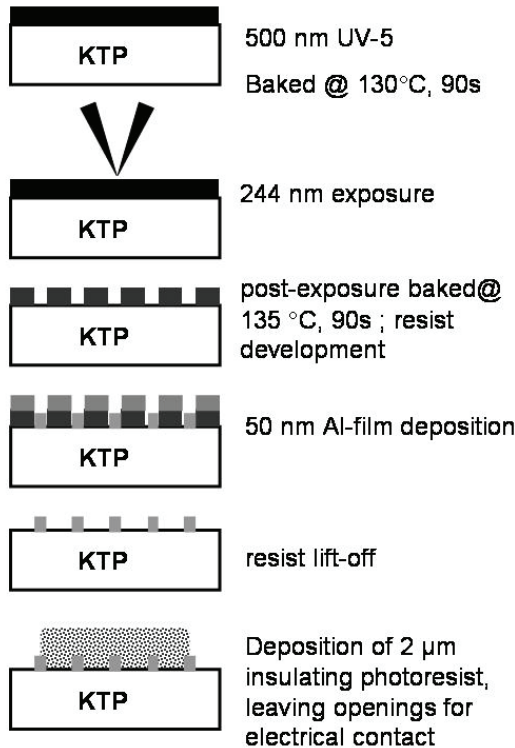
Fig. 8.6 Schematic of the steps involved in deep-UV laser lithography.

8.2.3. Duty-cycle control

The main problem with the above techniques lies in the difficulty to control the duty-cycle of the period. In the case of e-beam lithography, the control on the duty-cycle is lost during reactive ion etching, where small variations in the metal thickness derivate into variations of the final metal opening sizes. In the case of deep-UV laser lithography, the problem comes from the environmental instability of the photoresist, in other words, the sensitivity of the photoresist to the time between exposure and development. In normal work where there is 1 to 10 min this is not an issue, but for us it could pass more than an hour and then, it became a severe problem leading to loss of control in the pattern duty-cycle.

On top of that, optical microscopy has not enough resolution to inspect the quality of the lithographic gratings, and more slow techniques as SEM or AFM had to be used.

8.3. E-field poling

8.3.1 Monitoring techniques

Monitoring of sub-µm poling was found difficult. In principle, the poling can be monitored using the electro-optic technique described in section 7.3. However, due to

the large amount of domains to be inverted in a single sample, the intensity modulation can continue when the sub-micrmoeter domains merge together. Thus, this method is only reliable for indication if the poling starts.

On line QPM SHG can not be phasematched in the forward direction for such a short periods The signal of QPM BSHG is too small to be practical[PAPER VII], and the peak wavelength will depend very much on the relative angle between the beam and the sample. However, the Ti:Sapphire can be used to monitor the random QPM SHG, which depends on the square root of the number of domain walls in a random network of domains, with large number of domains.[14] The reason for random QPM is that there is a non-zero main domain length, so that the phases of certain wavelengths do compensate and, on average, SH is generated. Since SHG increases with the number of domains present in the crystal, it gives a good hint about how the poling proceeds.

8.3.2 Poling of sub-micrometer structures

Poling sub-µm structures is more difficult than poling "standard" QPM devices. One difficulty arises from controlling the effect of the electrodes fringing fields, which becomes larger with shorter periods, and the associated domain broadening. For this aspect, the number of pulses and the field strength become more critical. Moreover, the local inhomogeneities in the KTP crystals constitute a serious problem. Fig 8.7 shows an example of local inhomogeneities. Note that while some domains have the right width (400nm), others have merged together. Then, the general problem with sub-µm poling is to obtain poling uniformity.
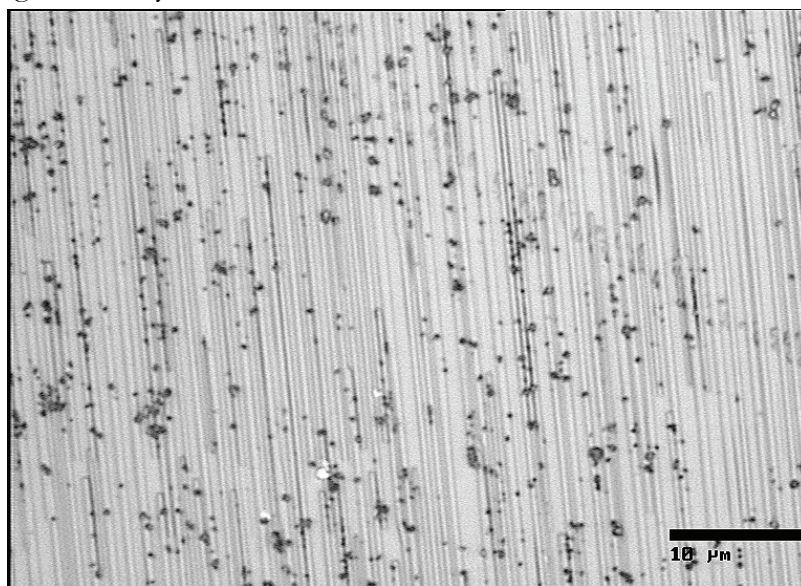
Fig 8.7 Example of local inhomogeneities. The sample was patterned with a Λ=800 nm. Note that while some domains have the right width (400nm), others have merged together.

Poling in the low field regime has given the best results, although it has not been possible to achieve homogeneous poling over the whole poled area. Variations in

stoichiometry yielded a poor poling uniformity, with samples presenting relatively well poled, underpoled and overpoled regions. However, it was still possible to obtain regions of reasonable quality. Fig 8.8 shows AFM images topography of the etched poled structure of a 0.5 mm thick sample that was poled by applying four 1 ms long electrical pulses of 1 kV. In this area, we can see that the periodically poled structure, as observed on the crystal back-side (original *c),* indicates that the poling was too short to allow the domains to fully close up under each electrode. The duty cycle was measured to be 40:60.
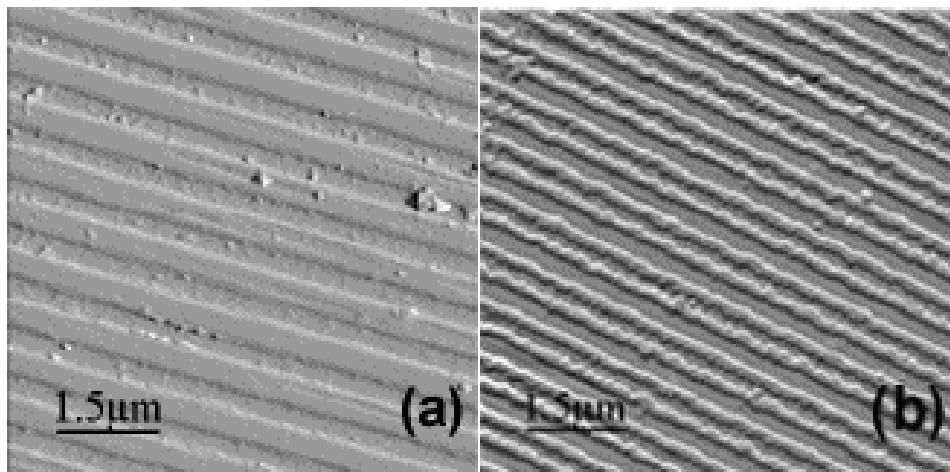
Fig. 8.8 AFM images showing the etched domain structure of a 0.5 mm sample pattern with a period of 800nm: (a) On the patterned surface; (b) On the opposite side.

Over all, we found the poling too difficult or, in other words, the yield became too low. Therefore, we decided to try to develop complementary technology to be able to get better results and an easier job. A chemical patterning method was therefore tested and found giving clearly improved results.

8.3.3 Chemical patterning

It has already been mentioned several times that flux-grown KTP has composition variations related to deviations in stoichiometry dominated by potassium and oxygen vacancies. Rosenman *et al.*[15] reported a decrease in coercive field for KTP when increasing the potassium content.

In order to obtain samples with better homogeneity, we tried to introduce extra K-ions by immersing them in a KNO_3 melt for 1 day at 380 °C. We could then observe a reduction in the coercive field that is attributed to an improved stoichiometry. Fig. 8.9 shows the measured coercive field of a non-patterned sample before and after K-enrichment. The coercive field before K-enrichment could not be measured due to an initially too high conductivity, but can be estimated to be ~2.3 kV/mm. After the K-enrichment, the same sample presents a coercive field of ~ 1kV/mm.
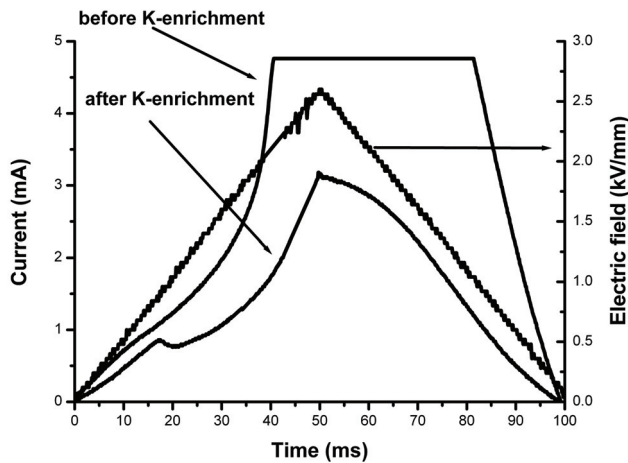
Fig 8.9 The measured coercive field of a non-patterned sample before and after K-enrichment. The coercive field before K-enrichment could not be measured due to an initially too high conductivity, but can be estimated to be ~2.3 kV/mm. After the K-enrichment, the same sample presents a coercive field of ~ 1kV/mm.

We now had two materials with drastically different poling voltage. The idea was, then, to fabricate a periodic structure of these materials, i.e. a chemical pattern. The chemical pattern was done in the following way: First, the sample was patterned with UV-laser lithography. After evaporating an Al-film of 50 nm on top of the pattern, an extra metal layer was deposited on the opposite face. The photoresist was then lift-off. The sample was immersed for about 1 day in a KNO$_3$ melt, and a grating of high and low coercive field regions was created. Since one of the polar faces was fully covered, the difference in coercive field between the enriched and non-enriched K regions in a patterned sample was estimated to be around 0.5 kV/mm. Afterwards, the metal was removed and the sample was ready for poling. Fig 8.10 depicts the chemical pattern process. The main advantage of this method is that the sample homogeneity is improved and that the fringing fields are avoided.
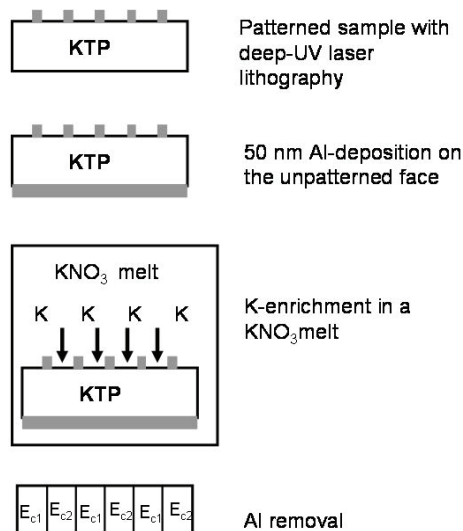
Fig. 8.10 Schematic of the steps involved in chemical patterning.

The sample was poled in the low field regime, taking advantage of the different velocities for the different stoichiometric areas. Fig. 8.11 shows a 1mm-thick sample poled by four 4.5 ms long square electrical pulses of 1.6 kV/mm. The total poled area was 7×4 mm^2. The topography of the poled structure of the patterned side can be seen in (a), and the domain structure on the backside is shown in (b). The average periodic domain size in this structure was 360 nm. As visually inspected the poling was homogenous over an area 5 x 2 mm^2. The maximum aspect-ratio achieved in our samples exceeded 0.4 to 1000. This is, to the best of our knowledge, the largest aspect ratio achieved in a bulk ferroelectric crystal.
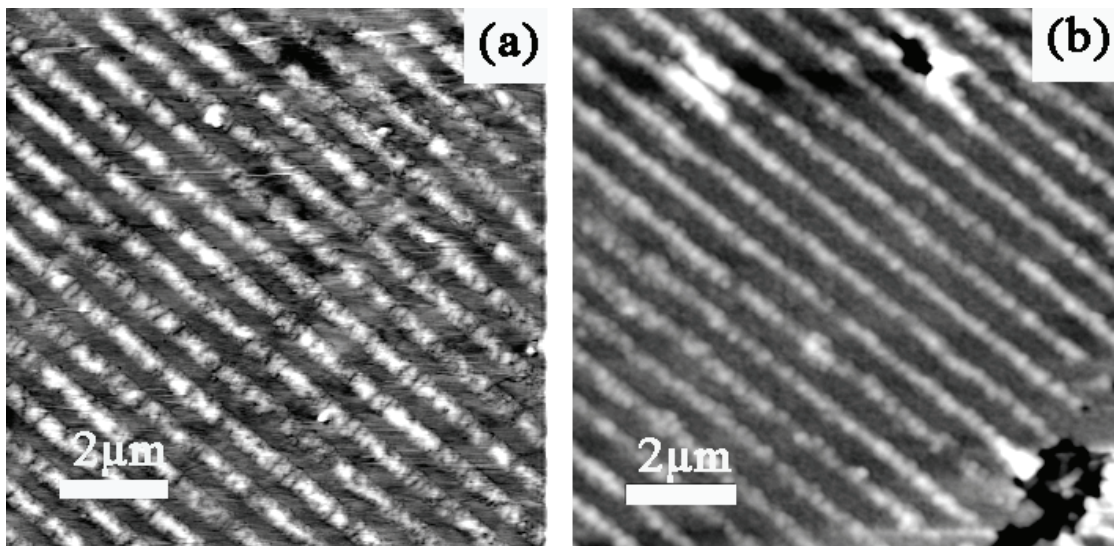
Fig 8.11. AFM images showing a 1 mm-thcik sample poled with a Λ=720 nm, (a) on the patterned surface, and (b) on the back side. The scale bar is 2 μm in both images.

8.4. Optical performance of sub-μm PPKTP

8.4.1. An electro-optical addressed Bragg reflector

Samples fabricated by e-beam lithography and electric field poling were tested as electro-optic Bragg modulators in a back-reflection configuration

The application of an external field, which is perpendicular to the direction of the electromagnetic wave propagation, produces the refractive index change via the electrooptic effect:

$$\Delta n_i = -\frac{1}{2} r_{ij} E_j n_i^3 \qquad (8.1)$$

where r_{ij} is the electro-optic coefficient of KTP, E_j is the strength of the external electric field in the direction j defined relative to the crystallographic axes of the

ferroelectric, and n_i is the refractive index for the electromagnetic wave polarized parallel to the direction i. The electro-optic coefficients have opposite signs in adjacent ferroelectric domains. Thus due to the action of the electro-optic effect the refractive index increases in one domain while it decreases by the same amount in the neighbouring ferroelectric domain. These changes give rise to a reflection at the domain walls with a reflection coefficient:

$$R = 0.25 r_{ij}^2 E_j^2 n_i^4 \qquad (8.2)$$

Due to multiple reflection at the domain walls the amplitudes of the reflected waves coherently add and produce a maximum at particular wavelengths λ_i for the electromagnetic wave which satisfy the Bragg condition $\Delta k_i = 0$, where

$$\Delta k_i = \frac{4\pi n_i}{\lambda_i} - \frac{2\pi m}{\Lambda} \qquad (8.3)$$

Here m is an integer number, called the order of the Bragg reflection. An example of the dependence of the wavelengths satisfying the Bragg condition on the order of reflectivity m is shown in Fig. 8.12 for the electro-optic Bragg modulator with a domain periodicity of 800 nm realized in KTP. Here the electromagnetic wave polarized parallel to the crystal z-axis was assumed.
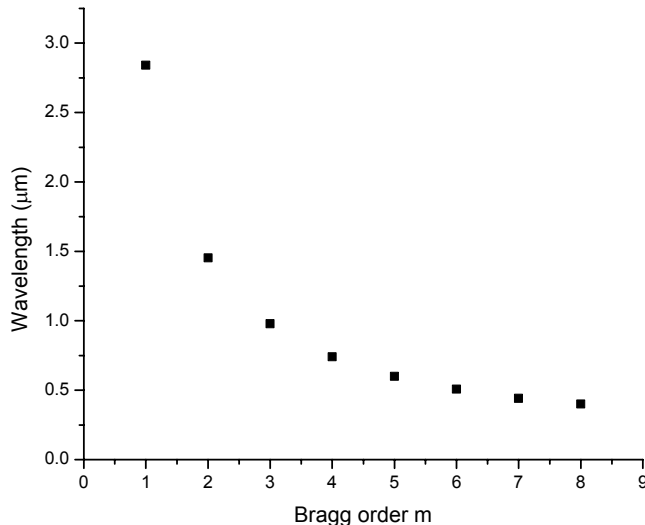
Fig 8.12. Bragg reflection wavelength as a function of the Bragg order for a sample with a period of 800 nm.

The amplitude of the reflected wave depends on the wavelength of the electromagnetic wave and the external electric field through the coupling coefficient:

$$\Omega = \frac{\pi \Delta n_i}{\lambda_i} . \qquad (8.4)$$

For an electro-optic Bragg reflector with a length L, the maximum reflectivity for an intensity of the electromagnetic wave at the wavelength satisfying the Bragg condition, can be calculated using the following formula:

$$R_{max} = \tanh^2(\Omega L) \qquad (8.5)$$

Generally, for a given device length and domain periodicity the reflection intensity is a function of wavelength and the applied electric field:

$$R(\lambda, E) = \frac{\Omega^2(\lambda, E)\sinh^2(s(\lambda, E)L)}{\Delta k^2(\lambda)\sinh^2(s(\lambda, E)L) + s^2(\lambda, E)\cosh^2(s(\lambda, E)L)}, \qquad (8.6)$$

where

$$s(\lambda, E) = \sqrt{\Omega^2(\lambda, E) - \Delta k(\lambda)}. \qquad (8.7)$$

The calculated dependence of the reflectivity on wavelength around the third-order ($m=3$) Bragg reflection for an electrooptic Bragg reflector realized in KTP with a domain period of 800 nm and a device length of 80μm and an external electric field of 2.6 kV/cm, is shown in Fig. 8.13.
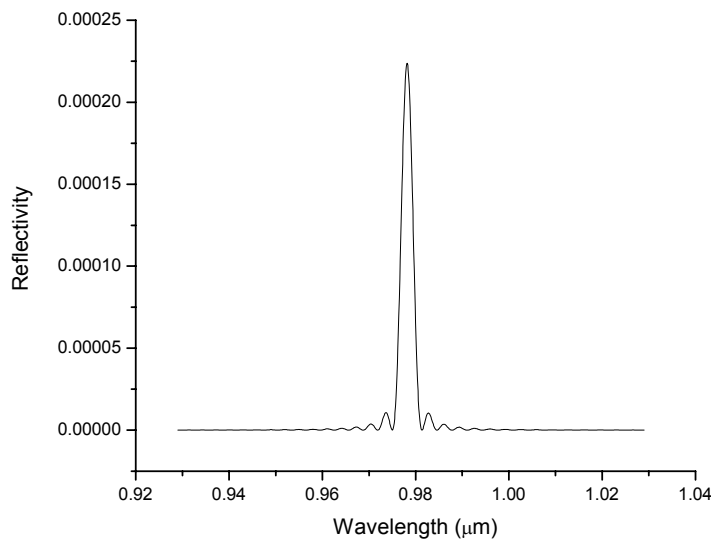
Fig. 8.13. 3rd order Bragg reflectivity vs. wavelength for a sample with a domain period of 800 nm .

The measured reflectivity dependence on external electric field in the same device at the wavelength corresponding to the third-order reflection (m=3) is shown in Fig. 8.14. Owing to the dependence of the reflection coefficient on the external voltage, this structure can be used as a spectrally selective electrooptic modulator.

As expected, the dependence is quadratic, obeying equation (8.2). The reflectivity reached 1.45 10^{-5}, which is about 17-times smaller than what is expected from theoretical calculations, and it corresponds to an effective structure length of 20 μm, compared to the actual one of 80 μm.
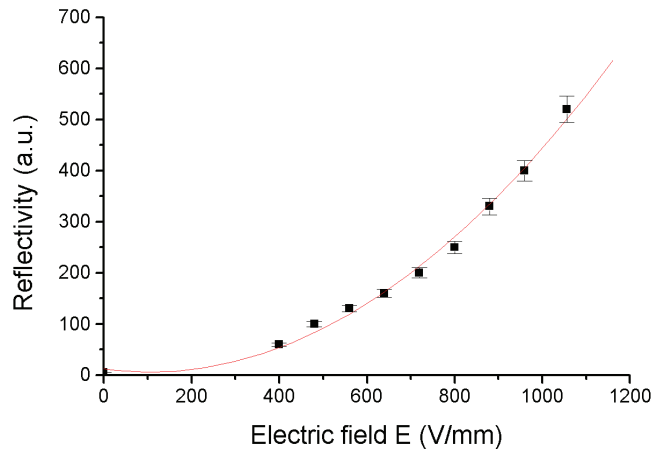
Fig 8.14. Backward reflectivity versus the peak-to-peak amplitude of the applied electric field.

Obviously, a reflectivity of the order of 10^{-5} is not very useful for practical applications. However, longer crystals, with improved poling quality, would give significantly higher reflectivity.

The same structure can also be used as a beam steering device where the modulated refractive index structure, obtained by applying the electric field, work just as a dielectric stack which reflect the beam in a certain direction. The direction is fixed, but the reflected amplitude depends on the applied electric field in the same manner as for the retroreflecting Bragg structure.

8.4.2. QPM BSHG

A 1 mm sub-μm PPKTP with $\Lambda=720$ nm fabricated by deep UV lithography and chemical patterning was used to demonstrate QPM backward SHG (BSHG).

The optical set-up used to characterize backward SHG is shown in Fig. 8.15. The fundamental beam, which was provided by a CW Ti:sapphire laser, was polarized in the z-direction by a half-wave plate. The beam was loosely focused (40 μm beam waste radius) into the PPKTP through a 1 mm diameter aperture with a f=150 mm lens. To avoid difficulties in separating backward SHG from higher order SHG generated by fundamental light reflected at the output end of the sample, and then propagating in the backward direction the sample had been polished with a small wedge at the output end. The backward SHG was collected by a confocal microscope arrangement consisting of a f=200mm collimating lens, followed by a f=40mm focussing lens, and a final pin-hole of 200μm in diameter. Two BG 39 filters were used directly before the photomultiplier in order to suppress scattered fundamental light from reaching the detector. The photomultiplier was connected to a lock-in amplifier. The power of the CW fundamental beam was kept constant at 320 mW during the spectral scans by employing a waveplate-polarizer arrangement. The laser was scanned through its tuning range, and two peaks

were observed. Using the Sellmeier equations derived by T.Y. Fan[16], the peaks were found to correspond to 6:th and 7:th order of QPM for a QPM period of 720 nm.
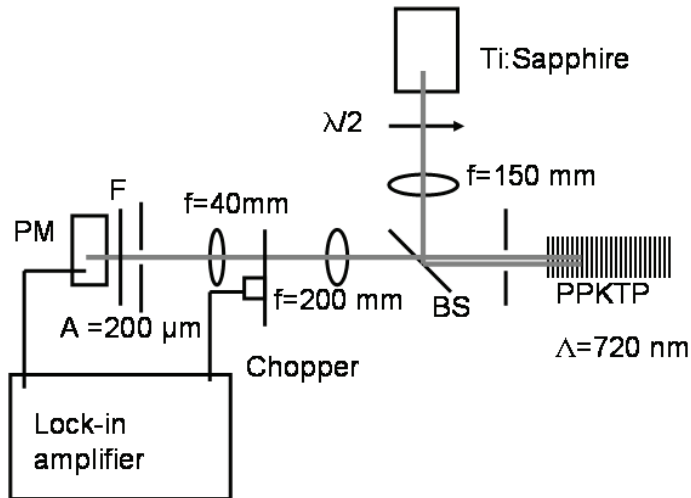
Fig. 8.15.Experimental set-up of BSHG. λ/2, half-wave plate, BS, beamsplitter; PM, photomultiplier; F, 2 BG39 filters.

Fig 8.16(a) and 8.16 (b) shows the spectrum of the 7:th and 6: th order QPM backward SHG, respectively. The spectral width of the BSHG process can be estimated from the phase-matching conditions, giving the wavelength FWHM bandwidth[8]:

$$\Delta\lambda = \frac{1.3925\ \lambda^2}{L\pi(n(\lambda) + n(\lambda/2))},\tag{8.8}$$

where λ, n and L are the fundamental wavelength, the refractive index and the length of the QPM structure, respectively. The spectral bandwidth calculated from equation (8.8) should be 0.15Å for a 5 mm-long structure. The measured bandwidth of the 7th order peak is 0.8 nm, substantially wider than the calculated one, but the measurement resolution was rather low, approximately 0.2 nm limited by the laser linewidth and the spectrum analyzer, and further diminished by the proximity of the noise floor of the detection system. Anyway this indicates that the effective length is shorter than what we observe just by observing the etched domain structure.
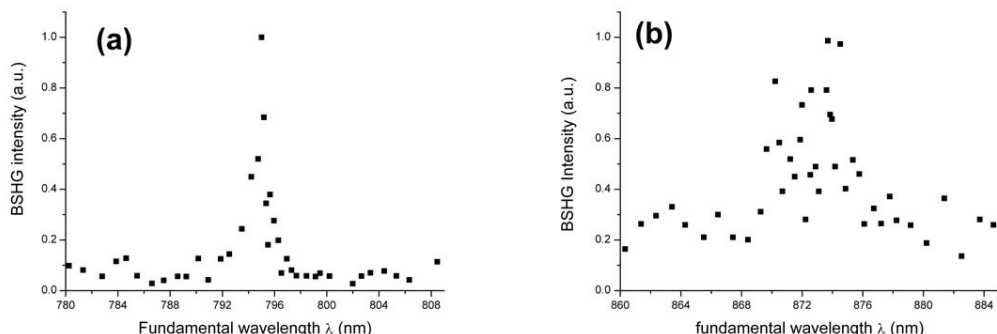
Fig. 8.16 . BSHG intensity as a function of the fundamental wavelength for (a) 7:th , and (b) 6:th order interactions.

The BSHG process efficiency can be calculated using[8,9]

$$\eta = \frac{\sqrt{2}\eta_0 d_{33}^2 I_F L^2 \Delta\lambda_{SH}}{4\sqrt{\pi}n(\lambda/2)n^2(\lambda)\left[n(\lambda) + n(\lambda/2)\right]^2 \Lambda^2 \Delta\lambda_F} ,$$

(8.9)

where η_0, d_{33}, I_F, $\Delta\lambda_{SH}$ and $\Delta\lambda_F$ are the vacuum impedance, nonlinear coefficient, fundamental intensity, second-harmonic and fundamental bandwidths, respectively. The second-harmonic power estimated from equation (8.9) in a 7th order 5 mm-long structure should be 12 nW. We estimate that our signal is slightly higher than 2 nW in good accordance with a effective length slightly shorter than 5 mm. Since for sub-micrometer periodically poled structures, the grating vector, K_m, is much larger than k_ω and $k_{2\omega}$, the BSHG linewidth and conversion efficiency are much more sensitive to the fabrication accuracy of the grating such as domain duty cycle and spatial inhomogeneity of the domains. The 6:th order, which should be absent in a perfect periodically poled crystal 50%:50% duty cycle, is also appearing, but with a much lower power, due to small variations in the domain grating.

In principle, QPM BSHG should be as efficient as forward SHG. However, it is much more sensitive to duty-cycle variations and pattern defects, which in practice, means lower efficiency. Nevertheless, it can be useful to test the quality of a sub-μm domain grattings in periodically poled samples. Moreover, QPM SHG is the first demonstration of backward parametric devices.

To the best of our knowledge, this was the first demonstration of cw-QPM BSHG in a bulk crystal.

References Chapter 8

[1] S. E. Harris, Appl. Phys. Lett. **9**, 114 (1966).

[2] G. D. Landry, and T. A. Maldonaldo, Optics Lett. **22**, 1400 (1997).

[3] G. D. Landry, and T. A. Maldonaldo, J. Lightwave Technol. 17, 316 (1999).

[4] K. Gallo, G. Assanto, K. R. Parameswaran and M. M. Fejer, Appl. Phys. Lett. **79**, 314 (2001).

[5] K. Mizuuchi, K. Yamamoto, M. Kato, Appl. Phys. Lett. **70**, 1201, (1997).

[6] J. P. Meyn, M. M. Fejer, Optics Lett. **22**,1214, (1997).

[7] S. Wang, V. Pasiskevicius, F. Laurell, H. Karlsson, Optics Lett. **23**, 1883 (1998).

[8] V.Ya. Shur, E.L. Rumyantsev, E.V. Nikolaeva, E.I. Shishkin, D.V. Fursov, R.G. Batchko, L.A. Eyres, M.M. Fejer, R.L. Byer; Appl. Phys. Lett. **76**, 143 (2000).

[9] W.P. Risk, S. D. Lau, M.A. McCord, IEEE Photonics Technology Letters, **6**,406 (1994).

[10] X. Mu, I.B. Zotova, Y.J. Ding, W.P. Risk, Optics Communications **181** 153 (2000).

[11] X. Gu, R. Y. Korotkov, Y. J. Ding, J. U. Kang, and J. B. Khurgin, J. Opt. Soc. Am. B **15**, 1561 (1998).

[12] G. Rosenman P. Urenski, A. Agronin, Y. Rosenwaks, and M. Molotskii , Appl. Phys. Lett. **82**, 103 (2003).

[13] M.C. Grupta, W. P. Risk, A. C. G. Nutt, Appl. Phy. Lett. 63, 1167 (1993).

[14] M. Baudrier-Raybant, R. Haïdar, Ph. Kupecek, Ph. Lemasson, and E. Rosencher, Nature 432, 374, (2004).

[15] G. Rosenman, P. Urenski, A. Arie, M. Roth, N. Angert, S. Skliar, M. Tseitlin, Appl.Phys. Lett. **76**, 3798 (2000).

[16] T. Y. Fan, C. E. Huang, B. Q. Hu, R. C. Eckardt, Y. X. Fan, R. L. Byer, and R. S. Feigelson, Appl. Opt. **26**, 2390 (1987).

Chapter 9

Description of the original work and author contribution

Paper I
Nanoscale imaging of domains and domain walls in periodically poled ferroelectrics using atomic force microscopy

J. Wittborn, C. Canalias, K.V. Rao, R. Clemens, H. Karlsson and F- Laurell

In this paper, ferroelectric domain structures in the polar faces of periodically poled $KTiOPO_4$ and $LiNbO_3$ crystals are visualized by applying an a.c. voltage between a gold-coated atomic force microscope tip and the bottom electrode of the ferroelectric crystal. The surface oscillations created by the inverse piezoelectric effect are detected by a lock-in technique. Contrast was observed between areas of opposite spontaneous polarization. In addition, by recording the lateral deflection of the tip, contrast at the domain walls was recorded. Domain wall widths for both materials were studied by these methods, and were found to be ~60 nm for $KTiOPO_4$ and ~150 nm for $LiNbO_3$.

Contributions by the author: The author participated in the AFM measurements, in the discussion and in the manuscript preparation.

Paper II

High-resolution domain imaging on the nonpolar y-face of periodically poled KTiOPO₄ by means of atomic force microscopy

C. Canalias, V. Pasiskevicius, A. Fragemann and F- Laurell

High-resolution images of ferroelectric domains in periodically poled KTiOPO₄ crystals on their nonpolar *b*-face were produced using the inverse piezoelectric effect and an atomic force microscopy. Domain nucleation and grown in electric field periodically poled KTiOPO₄ was studied, and effects like domain broadening and growth of needle like submicron domains were reported.

Contributions by the author: The author participated in poling the crystals, did the AFM measurements, and took part in the discussions and in preparation of the manuscript.

Paper III

Polarization switching characteristics of flux-grown KTiOPO₄ and RbTiOPO₄ at room temperature

C. Canalias, J. Hirohashi, V. Pasiskevicius, and F- Laurell

Domain reversal in KTiOPO₄ and RbTiOPO₄ at room temperature was studied. By optimizing the experimental conditions, we were able to determine the coercive field and domain switching time quantitatively by measuring the switching current dynamics. The coercive field of high-conductivity KTP samples was found to be higher than that of the low-conductive ones. KTP has an internal field formed by non-stoichiometric point defects. E_c decreases with the number of polarization-cycles as a consequence of redistribution of K^+ vacancies during electric field poling. The coercive field E_c and the internal field in RTP was found to remain constant over the number of polarization-cycles due to the lower mobility of the Rb ions which prevents easy redistribution of the space charges.

For both isomorphs, the inverse of the polarization-switching time, *1/t*, was found to follow an exponential dependence on the applied field E in low field regime, and a linear dependence on E in the high field regime.

The ferroelectric domain morphology in KTiOPO₄ was investigated by selective etching and revealed laminar structures elongated in the *b* crystallographic direction. Estimation of the domain wall velocity showed that in the polar direction it is, at least, two orders of magnitude larger than in the *a-b* plane. In turn, the velocity along the *b*-direction is ~ 30 times higher than along the *a*-axis.

Description of the original work and author contribution

Contributions by the author: The author did the measurements, took part in the discussions and in the manuscript preparation.

Paper IV
In-situ visualization of domain kinetics in flux-grown KTiOPO$_4$ by digital holography
C. Canalias, V. Pasiskevicius, F. Laurell, S. Grilli, P. Ferraro, P. De Natale

A digital holographic technique was used *in-situ* to visualize the domain kinetics in flux grown KTiOPO$_4$. Three different electric field pulse shapes were used to study the domain switching process. In the case of square pulses, the incubation time and the total poling time were found to be one order of magnitude larger for first forward poling than those of subsequent domain reversals. The use of a train of pulses prevented domain wall pinning. In the case of poling with triangular pulses, a more uniform nucleation and domain growth was achieved. This was attributed to diminished influence of capacitive space-charge regions on the electric field distribution in the bulk of the crystal.

Contributions by the author: The author participated in the measurements, discussions, and in writing of the paper.

Paper V
Nucleation and growth of periodic domains during electric field poling in flux-grown KTiOPO$_4$ observed by atomic force microscopy
C. Canalias, S. Wang, V. Pasiskevicius, and F. Laurell

The domain structure of periodically poled KTiOPO$_4$ were studied on both the polar and nonpolar faces utilizing a voltage-modulated atomic force microscope. Domain nucleation at the edges the electrodes and charge deposition underneath the insulator, which broadens the domain; were observed. This broadening proved to be severe if many electrical pulses are applied. Sidewise domain growth and merging was observed to occur before the tips reach the opposite polar face. Forward and sidewise growths were identified as to two competing processes. It was also shown that if electrical pulses of too high magnitude are used, nucleation might occur on the unpatterned polar face giving rise to bulk broadening and merging.

Contributions by the author: The author poled the samples, participated in the experiments, discussions, and in writing of the paper.

Paper VI
Submicron periodically poled flux-grown KTiOPO$_4$
C. Canalias, V. Pasiskevicius, R. Clemens, and F. Laurell

We reported for first time on a sub-micron domain grating created in a bulk ferroelectric. Electron-beam lithography and electric field poling were used to fabricate a 800 nm period grating in a 0.5-mm-thick flux-grown KTiOPO$_4$ sample. The domain structure was characterized with an atomic force microscope and was used to demonstrate electrically amplitude adjustable Bragg reflections.

Contributions by the author: The author fabricated the sample, participated in the optical measurements, and took part in the discussions and in preparation of the manuscript.

Paper VII
Backward quasi-phase-matched second-harmonic generation in submicrometer periodically poled flux-grown KTiOPO$_4$
C. Canalias, V. Pasiskevicius, M. Fokine, and F. Laurell

A 1 mm thick flux-grown KTiOPO$_4$ sample was poled with a 720 nm domain period by employing in-house built deep-UV laser lithography, in combination with chemical patterning, which creates a grating with periodic high and low K-stoichiometry, and electric field poling. An atomic force microscope was used to characterize the periodic domain structure. The sample was used to demonstrate 6:th and 7:th order continuous-wave quasi-phase matched backward second harmonic generation.

Contributions by the author: The author participated in building the lithographic set-up, and then did the chemical patterning and poled the sample. The author took part in the optical measurements, the discussions, and in the paper writing.

Chapter 10

Summary

In this thesis, several techniques to study domain structure in KTP have been shown, both in-situ and ex-situ. The results obtained have been used to characterize different aspects of the polarization switching processes in KTP, both for patterned and unpatterned samples. The combination of results has been an important factor for gaining a more comprehensive understanding of the domain-inversion process.

It has been demonstrated that use of the inverse piezoelectric effect in voltage-modulated AFM is a very effective and informative tool for studies of domain structures at both polar and non-polar crystal faces. Thus, effects as domain formation, tip propagation and domain broadening have been studied with nanometer resolution.

With electrical studies we were able to determine the coercive field and domain switching time quantitatively by measuring the switching current dynamics. The coercive field of high conductive KTP samples is higher than that of low conductive ones. KTP has an internal field formed by non-stoichiometric point defects. E_c decreases with the number of polarization-cycles as a consequence of redistribution of vacancies during the electric field poling. The inverse of switching time $1/t_s$ depends exponentially on the applied field E in low field regime, while a linear dependence on E in the high field regime is observed.

The ferroelectric domain morphology in KTP investigated by selective etching reveals laminar structures elongated in the b crystallographic direction. Estimation of the domain wall velocity shows that in the polar direction it is, at least, two orders of magnitude larger than in the a-b plane. In turn, the velocity along the b-direction is ~ 30 times higher than along the a-axis.

In-*situ* visualization of domain kinetics in KTP by a digital holographic technique has been demonstrated. When the sample is subjected to square electrical pulses, the incubation time and the total poling time are one order of magnitude larger for the first forward poling than those of subsequent domain reversals. The use of a train of pulses prevents domain wall pinning. In the case of poling with triangular pulses, a more

uniform nucleation and domain growth is achieved due to diminished influence of capacitive space-charge regions on the electric field distribution in the bulk of the crystal. For periodic poling of KTP, several factors have to be taken into account: (i) charge deposition underneath the insulator broadens the domain; this broadening can be severe if many pulses are applied; (ii) the use of metal on the c-face enhances domain nucleation and gives straighter domain walls; (iii) sidewise growing and merging of domains occurs before the tips reach the opposite polar face, (iv) forward and sidewise growing seem to be two competing processes, (v) if electrical pulses of too high magnitude are used, nucleation might occur on the unpatterned polar face giving rise to bulk broadening and merging.

It has also been demonstrated that it is possible to fabricate sub-μm PPKTP for novel optical devices. Lithographic processes based on e-beam lithography and deep UV-laser lithography have been proven useful to pattern sub-μm pitches, where the later has been the most convenient method. A poling method based on a periodical modulation of the K-stoichiometry has been developed, and has resulted in a sub-micrometer domain grating with a period of 720 nm for a 1mm thick KTP crystal. To the best of our knowledge, this is the largest domain aspect-ratio achieved in a bulk ferroelectric crystal. The sub-micrometer PPKTP samples have been used for demonstration of 6:th and 7:th QPM order backward SHG with CW laser excitation, as well as demonstration of electrically-adjustable Bragg reflectivity.

I believe all these results improve the understanding of domain reversal in KTP under electric fields and can be used to improve fabrication of periodically poled structures for QPM devices.

Acknowledgments